

Copyright  
by  
David Robert Rounce  
2016

**The Dissertation Committee for David Robert Rounce Certifies that this is the  
approved version of the following dissertation:**

**Debris-Covered Glaciers:  
Modeling ablation and flood hazards in the Nepal Himalaya**

**Committee:**

---

Daene C. McKinney, Supervisor

---

David R. Maidment

---

Ben R. Hodges

---

Ginny A. Catania

---

Zong-Liang Yang

**Debris-Covered Glaciers:  
Modeling ablation and flood hazards in the Nepal Himalaya**

**by**

**David Robert Rounce, B.S., M.S.E.**

**Dissertation**

Presented to the Faculty of the Graduate School of

The University of Texas at Austin

in Partial Fulfillment

of the Requirements

for the Degree of

**Doctor of Philosophy**

**The University of Texas at Austin**

**May, 2016**

## **Dedication**

To my mother and father for their unconditional love and support.

## **Acknowledgements**

I am grateful for the incredible support I've received over the years from all my family, friends, and colleagues. Five years ago I never imagined I'd be trekking in the Himalaya for research – Daene McKinney, I am forever indebted to you for giving me the opportunity to find my passion for the mountains and truly cherish all the time we spent together in the field. You've been a wonderful mentor. Desmond Lawler and Michael Barrett, I thank you both for encouraging and supporting me to follow my passion for international work both in research and service. Dorothy Hall, thank you for giving me the opportunity to join you at Goddard – I truly cherished being a part of such an electric atmosphere and appreciate all your guidance.

Fieldwork would not have been the same without the tremendous support from Dhananjay Regmi and all those I trekked with from the Himalayan Research Expedition (HRE). Alton and Elizabeth Byers, thank you for sharing your knowledge of the mountains and truly bringing the trail to life. Duncan Quincey, you've been a great mentor and friend from across the pond.

My research was funded by the USAID Climate Change Resilient Development (CCRD) project and the NSF Dynamics of Coupled Natural and Human Systems (CNH) program. I'd also like to acknowledge the SHARE Project thanks to contributions from the Italian National Research Council and the Italian Ministry of Foreign Affairs for providing me with data support. Without the support of these organizations, none of this work would have been possible.

Most importantly, a special thanks to my wonderful family – Anne, Mom, and Dad. Anne, you're one of the hardest working and most driven people that I know and

set an example that I strive to follow. Mom and Dad, you taught me to follow my dreams and have supported me in everything that I've ever done. Words can't express the love and gratitude I have for you guys – I'll forever continue to try and make you guys proud.

**Debris-Covered Glaciers:  
Modeling ablation and flood hazards in the Nepal Himalaya**

David Robert Rounce, Ph.D.

The University of Texas at Austin, 2016

Supervisor: Daene C. McKinney

Debris-covered are ubiquitous in the Nepal Himalaya and significantly alter the glaciers response to climate change and have large implications on the development of glacial lakes. The thickness of the debris is largely heterogeneous over the course of the glacier thereby promoting ablation in areas of thin debris and retarding ablation in areas of thick debris. The debris thickness typically increases towards the snout of the glacier, but can be difficult to measure as field measurements are time-consuming and laborious. This body of work utilizes satellite imagery in conjunction with a debris-covered glacier energy balance model to reasonably estimate the spatial variations in debris thickness for glaciers in the Everest region of Nepal. Sub-debris ablation rates may be computed using the same energy balance model, but requires detailed information regarding the properties of the debris and the surface processes. Detailed field data was collected over the 2014 melt season on Imja-Lhotse Shar Glacier to estimate many of the debris properties. This data was also used to model the sub-debris ablation rates to develop an understanding of the critical properties (i.e., thermal conductivity, albedo, and surface roughness) and processes (i.e., accounting for the latent heat flux) required to accurately model the impact of the debris.

The heterogeneous debris cover often causes higher melt rates upglacier, which diminishes the glacier's topographic gradient thereby promoting glacier stagnation and the development of glacial lakes. These glacial lakes form behind terminal moraines comprising soil and loose boulders that are susceptible to fail causing a glacial lake outburst flood (GLOF). GLOFs can have devastating impacts on infrastructure and communities located downstream; however, assessing the risks associated with these floods has traditionally required detailed field campaigns that are difficult to perform as these glacial lakes are located in remote areas at high altitudes. This body of work develops a holistic hazard assessment using solely remotely sensed data to objectively characterize the threat of a GLOF. This hazard assessment provides valuable information concerning potential GLOF triggers that may be used to direct future field campaigns and ultimately the management actions associated with these glacial lakes.

## Table of Contents

List of Tables .....	xiii
List of Figures .....	xv
<b>Chapter 1 Introduction .....</b>	<b>1</b>
1.1 Motivation .....	1
1.2 Research Questions .....	3
1.3 Hypotheses .....	3
1.4 Outline .....	4
<b>Chapter 2 Background .....</b>	<b>5</b>
2.1 Evolution of debris-covered glaciers .....	5
2.2 Debris-covered energy balance model .....	7
2.3 GLOF triggers and process chain .....	8
<b>Chapter 3 Debris thickness of glaciers in the Everest area (Nepal Himalaya) derived from satellite imagery using a nonlinear energy balance model .....</b>	<b>11</b>
3.1 Abstract .....	11
3.2 Introduction .....	12
3.3 Data .....	15
3.3.1 Meteorological data .....	15
3.3.2 Remotely sensed data.....	17
3.3.3 Field data .....	20
3.3.3.1 Study site .....	20
3.3.3.2 Debris measurements .....	20
3.4 Methods .....	22
3.4.1 Energy balance model .....	22
3.5 Field results .....	25
3.5.1 Thermal conductivity .....	25
3.5.2 Debris thickness .....	26
3.5.3 Nonlinear approximation factor, $G_{\text{ratio}}$ .....	27

3.6 Modeled results .....	30
3.6.1 Nonlinear sloped model - 5 m pixels .....	30
3.6.2 Nonlinear sloped model - 30 m pixels .....	33
3.6.3 Linear sloped model - 30 m pixels .....	35
3.6.4 Nonlinear flat model - 30 m pixels .....	35
3.6.5 Importance of DEM resolution .....	36
3.6.6 Debris thickness for glaciers in the Everest region .....	37
3.6.7 Sensitivity analysis .....	38
3.7 Conclusion .....	41
3.8 Acknowledgements .....	41

**Chapter 4 Debris-covered glacier energy balance model for Imja-Lhotse Shar Glacier in the Everest region of Nepal .....43**

4.1 Abstract .....	43
4.2 Introduction .....	44
4.3 Data .....	47
4.3.1 Field data .....	47
4.3.2 Meteorological data .....	51
4.4 Methods .....	53
4.4.1 Surface roughness .....	53
4.4.2 Debris-covered glacier energy balance model .....	58
4.5 Field results .....	61
4.5.1 Thermal conductivity (k) .....	61
4.5.2 Surface roughness ( $z_0$ ) .....	62
4.5.3 Ablation stakes .....	66
4.6 Modeled results .....	67
4.6.1 Model calibration .....	67
4.6.2 Model validation .....	71
4.6.3 Modeled ablation rates .....	72
4.6.4 Sensitivity analysis .....	76
4.6.5 Temporal resolution .....	78

4.7 Field results .....	81
4.7.1 Thermal conductivity .....	81
4.7.2 Surface roughness .....	82
4.7.3 Modeled results .....	84
4.8 Conclusions .....	85
4.9 Acknowledgements .....	87

**Chapter 5 A new remote hazard and risk assessment framework for glacial lakes in the Nepal Himalaya .....88**

5.1 Abstract .....	88
5.2 Introduction .....	89
5.3 Study area .....	92
5.4 Existing methods .....	95
5.4.1 Summary .....	95
5.4.2 Application of existing methods .....	96
5.5 New hazard and risk framework .....	100
5.5.1 Remote hazard assessment .....	102
5.5.1.1 Mass movement trajectories .....	103
5.5.1.2 Lake expansion .....	105
5.5.1.3 Hydrostatic pressure .....	107
5.5.1.4 Buried ice .....	108
5.5.1.5 GLOF modeling .....	109
5.5.1.6 Downstream impact .....	114
5.5.2 Risk classification and management actions .....	115
5.6 Results & discussion of remote hazard assessment .....	118
5.6.1 Imja Tsho .....	122
5.6.2 Lumding Tsho .....	126
5.6.3 Chamlang North Tsho .....	132
5.6.4 Chamlang South Tsho .....	133
5.6.5 Dig Tsho .....	135
5.6.6 Lower Barun Tsho .....	136

5.6.7 Thulagi Tsho .....	138
5.6.8 Tsho Rolpa .....	140
5.7 Conclusions .....	142
5.8 Acknowledgements .....	143
5.9 Supplementary material .....	144
<b>Chapter 6 Conclusions and future perspective .....</b>	<b>156</b>
6.1 Research Questions .....	156
6.1.1 How does debris cover affect the evolution of glaciers and glacial lakes in the Everest region of Nepal? .....	156
6.1.2 What underlying properties and processes are critical for modeling the ablation of debris-covered glacier? .....	157
6.1.3 Can remotely sensed data be used to objectively quantify the hazards associated with dangerous glacial lakes? .....	159
6.1.4 What role should field campaigns serve in the management of glacial lakes? .....	160
6.2 Contribution to knowledge and concluding remarks .....	162
<b>References .....</b>	<b>164</b>

## List of Tables

Table 3.1: Overview of satellite imagery used in this study .....	18
Table 3.2: Modeled results for the nonlinear sloped and flat model in the focus area with the high resolution DEM showing trends in debris thickness ( $d$ ), surface temperature ( $T_s$ ), and net radiation ( $R_n$ ) with respect to slope and aspect .....	31
Table 3.3: Sensitivity analysis for select meteorological and model parameters .....	39
Table 4.1: Details of debris thickness, topography, and monitoring equipment installed at each site. <i>Italics</i> note an estimation of debris thickness. $T_s$ denotes surface temperature .....	50
Table 4.2: Errors associated with the DEM for each site .....	63
Table 4.3: Surface roughness ( $z_0$ ) estimates and obstacle thresholds as a function of DEM resolution (m) at Sites A-D .....	65
Table 4.4: Optimized values of albedo, thermal conductivity, and surface roughness for three methods of estimating the latent heat flux during calibration period .....	68
Table 4.5: Sensitivity analysis showing percent changes relative to the total melt (m) as a function of the uncertainty associated with the calibration parameters ( $\alpha$ , $k$ , $z_0$ ) for all sites over the study period using the $LE_{Rain}$ model in conjunction with the average calibrated parameters for all sites .....	77

Table 5.1: Previous qualitative hazard assessments applied to eight glacial lakes in Nepal. Fractions are the amount of hazard parameters identified out of the total number of parameters used by each model. Details shown in Tables 5.7 - 5.9 .....	97
Table 5.2: Previous semi-quantitative and quantitative hazard assessments applied to eight glacial lakes in Nepal. Values and thresholds for classifications are specific to each study. Fractions are the amount of scenarios for each lake that are considered to be highly dangerous. Details shown in Tables 5.10 - 5.12 .....	98
Table 5.3: Most frequently used parameters associated with previous studies (adapted from Emmer and Vilímek, 2013) .....	100
Table 5.4: Summary of the hazard parameters for the studied glacial lakes .....	119
Table 5.5: Summary of hazard, downstream impact, and risk for each glacial lake .....	120
Table 5.6: Details of downstream impacts from MC-LCP GLOF models for each glacial lake .....	121
Table 5.7: Results of O'Connor et al. (200) hazard assessment .....	144
Table 5.8: Results of Costa and Schuster (1988) hazard assessment .....	144
Table 5.9: Results of Wang et al. (2008) hazard assessment .....	145
Table 5.10: Results of Bolch et al. (2011a) hazard assessment .....	145
Table 5.11: Results of Wang et al. (2011) hazard assesment .....	146
Table 5.12: Results of Emmer and Vilímek (2014) hazard assessment .....	146
Table 5.13: Details concerning the satellite imagery, dates, bands, thresholds, and area (km <sup>2</sup> ) for each glacial lake in this study .....	147

## List of Figures

Figure 2.1: Empirical relationship between debris thickness and ablation rates for various glaciers throughout the world (Fig. 1 from Nicholson and Benn, 2006) .....	5
Figure 2.2: The evolution of glacial lakes on debris-covered glaciers as a function of climate change (adapted from Benn et al., 2012) .....	6
Figure 2.3: The GLOF process chain for mass movement entering a glacial lake (Worni et al., 2014) .....	9
Figure 3.1: Panchromatic band from Landsat 7 on 04 Oct 2002 showing Imja Lake, the focus area on Imja-Lhotse Shar Glacier, and Pyramid Station amongst debris-covered glaciers in the Everest region .....	17
Figure 3.2: Surface temperature derived from Landsat7 imagery (left) and corresponding meteorological data (right) on 04 October 2002 .....	19
Figure 3.3: Debris thickness measurements on Imja-Lhotse Shar Glacier inside and outside of the melt basin .....	27
Figure 3.4: Temperature profiles at site LT3 at 10:15 with the temperature gradients used to compute $G_{ratio}$ identified .....	28
Figure 3.5: $G_{ratio}$ as a function of depth (left) and corresponding $G_{ratio}$ values at 10 cm depth for each sensor (right) .....	29
Figure 3.6: Debris thickness (m) with 30 m pixels using the (A) nonlinear sloped model, (B) linear sloped model, (C) nonlinear flat model, and (D) using the ASTER GDEM with the nonlinear sloped model.....	34

Figure 3.7: Debris thickness (m) using the ASTER GDEM and nonlinear sloped model for debris-covered glaciers in the Everest region with Ngozumpa, Khumbu, and Imja-Lhotse Shar Glaciers, left to right respectively, highlighted with GLIMS outlines .....38

Figure 4.1: Landsat 8 panchromatic image from 14 Nov 2014 of Imja-Lhotse Shar Glacier with the focus area of this study highlighted by the rectangular box several kilometers up-glacier from the terminus, and the site location within Nepal shown in the inset .....48

Figure 4.2: Sites A-D highlighting the variations in grain sizes that are found over the debris-covered portion of Imja-Lhotse Shar Glacier (cones 0.19 m diameter) .....49

Figure 4.3: Transect from Left-Right of Site B showing the identification of obstacles (Obst) and their corresponding heights ( $h_{\text{obst}}$ ) and depths ( $d_{\text{obst}}$ ) .....57

Figure 4.4: The effect of obstacle threshold (m) on both obstacle density and the estimate of surface roughness using the modified method for Sites A-D and the DEMs with a resolution of 0.01 m .....64

Figure 4.5: Various plots for Site 11 using the  $LE_{\text{Rain}}$  model showing (A) average daily temperatures at two depths (solid and dashed lines indicate measured and modeled temperatures, respectively), (B) average daily energy fluxes, (C) measured and modeled temperatures at a depth of 0.01 m over the calibration period, and (D) measured and modeled temperatures over the validation period.....70

Figure 4.6: Scatterplot of measured and modeled temperature for Site 11 at the surface for the  $LE_{\text{Rain}}$  model showing the positive temperature bias overnight .....71

Figure 4.7: Modeled ablation with respect to debris thickness for all 15 sites from 18 May to 09 November 2014 for each of the three latent heat flux models including the $LE_{\text{Rain}}$ model with average values and the three measured stakes that did not exceed 1 m .....	74
Figure 4.8: Modeled and measured surface temperature at Site 11 over the (A) calibration period and (B) validation period using 6-hour data, and (C) entire period using daily averages .....	80
Figure 5.1: The location of the eight glacial lakes assessed in this study in the Nepal Himalaya .....	93
Figure 5.2: Schematic of GLOF hazard parameters used in new method: (1) snow/ice avalanche, (2) rockfall, (3) flood from upstream lake, (4) lake expansion, (5) hydrostatic pressure, (6) ice-cored moraine, and (7) downstream impact .....	102
Figure 5.3: Inundated areas at Dingboche for a GLOF from Imja Tsho using (A) FLO2D (Somos-Valenzuela et al., 2015), (B) the MSF model using the GDEM, (C-G) the MC-LCP model with various DEMs and pixel sizes: (C) SRTM 90 m resampled 15 m, (D) GDEM 30 m resampled 15 m, (E) SRTM 90 m resampled 30 m, (F) GDEM 30 m, and (G) SRTM 90 m .....	113
Figure 5.4: Hazard classification flow chart for determining the hazard associated with a glacial lake (numbers refer to hazard parameters in Figure 5.2) .....	116

Figure 5.5: Risk and management action framework. Left table: GLOF risk is a function of the hazard and downstream impact. Right table: the recommended course of action for a given glacial lake based on the type of assessment .....117

Figure 5.6: Area of glacial lakes derived from satellite imagery using the NDWI method from 2000 to 2015 (details in Table 5.13) .....122

Figure 5.7: Hazards and downstream impact for Imja Tsho: (A) avalanche trajectories, (B) rockfall trajectories, (C) ponds on the moraine, (D) future lake expansion, and (E) the extent of the MC-LCP GLOF model (F) highlighting the impacts at Dingboche .....124

Figure 5.8: Bathymetric survey conducted on Lumding Tsho on 22-23 October 2015 .....128

Figure 5.9: Lumding Tsho and its surrounding slopes with areas of concern highlighted in red showing (A) the calving front and prone areas behind the glacier, (B) the southern side slope, and (C) the terminal moraine and its gentle outlet .....131

Figure 5.10: Hazards and downstream impact for Chamlang North Tsho: (A) avalanche trajectories, (B) rockfall trajectories, (C) lack of ponds on the moraine, (D) future lake expansion, and (E) the extent of the MC-LCP GLOF model (F) highlighting the impacts downstream .....149

Figure 5.11: Hazards and downstream impact for Chamlang South Tsho: (A) avalanche trajectories, (B) rockfall trajectories, (C) ponds on the moraine, (D) future lake expansion, and (E) the extent of the MC-LCP GLOF model (F) highlighting the impacts downstream .....150

Figure 5.12: Hazards and downstream impact for Dig Tsho: (A) avalanche trajectories, (B) rockfall trajectories, (C) lack of ponds on the moraine, (D) future lake expansion, and (E) the extent of the MC-LCP GLOF model (F) highlighting the impacts downstream .....151

Figure 5.13: Hazards and downstream impact for Lower Barun Tsho: (A) avalanche trajectories, (B) rockfall trajectories, (C) ponds on the moraine, (D) future lake expansion, and (E) the extent of the MC-LCP GLOF model (F) highlighting the impacts downstream .....152

Figure 5.14: Hazards and downstream impact for Lumding Tsho: (A) avalanche trajectories, (B) rockfall trajectories, (C) lack of ponds on the moraine, (D) future lake expansion, and (E) the extent of the MC-LCP GLOF model (F) highlighting the impacts downstream .....153

Figure 5.15: Hazards and downstream impact for Thulagi Tsho: (A) avalanche trajectories, (B) rockfall trajectories, (C) ponds on the moraine, (D) future lake expansion, and (E) the extent of the MC-LCP GLOF model (F) highlighting the impacts downstream .....154

Figure 5.16: Hazards and downstream impact for Tsho Rolpa: (A) avalanche trajectories, (B) rockfall trajectories, (C) the moraine complex, (D) future lake expansion, and (E) the extent of the MC-LCP GLOF model (F) highlighting the impacts downstream .....155

## Chapter 1: Introduction

### 1.1 MOTIVATION

Debris-covered glaciers are ubiquitous throughout the Nepal Himalaya and have an important effect on the evolution of the glacier and the formation of glacial lakes. A thick layer of debris (greater than several centimeters) will insulate the glacier and reduce the amount of melt, while a thin layer of debris (less than several centimeters) may enhance melt due to the different spectral properties of debris and ice (Østrem, 1959; Nakawo and Young, 1981; Nicholson and Benn, 2006; Rounce et al., 2015). The debris cover is typically thickest near the terminal moraine and thins upglacier (Nicholson and Benn, 2012; Rounce and McKinney, 2014). This spatial variation of debris cover can cause the ablation rates, the melt and sublimation of ice, to be higher upglacier where the debris cover is thinner. In turn, this differential melting alters the topographic gradient of the glacier thereby promoting glacier stagnation (Benn et al., 2012). Glacial lakes typically develop on the gentle slopes of these stagnant debris-covered glaciers (Reynolds, 2000; Quincey et al., 2007; Bolch et al., 2008) and when this occurs behind a terminal moraine, the lake may grow to a volume exceeding  $10^8 \text{ m}^3$  (Benn et al., 2012).

The terminal moraines are composed of loose boulders, soil, and frequently ice cores and are a significant hazard to downstream communities due to the threat of a glacial lake outburst flood (GLOF). GLOFs unleash stored lake water often causing enormous devastation downstream that can include high death tolls as well as the destruction of valuable farmland and costly infrastructure (e.g., hydroelectric facilities, trails, roads, and bridges). In 1985, Dig Tsho (“tsho” means lake) experienced a GLOF that destroyed a newly built hydroelectric power plant along with bridges, houses, and large swathes of arable farmlands (Vuichard and Zimmerman, 1987). The large fiscal

consequences of this GLOF brought the hazards associated with these glacial lakes into the spotlight. Unfortunately, as the number and area of glacial lakes continues to increase in response to climate change (Bajracharya and Mool, 2009; Sakai et al., 2009; Bolch et al., 2011b), the risk of more GLOFs increases as well (Richardson and Reynolds, 2000).

A variety of methods have been developed to characterize potentially hazardous glacial lakes and the risk of GLOFs (Emmer and Vilímek, 2013). These methods vary considerably based on the parameters used, the weight given to each parameter, the source of the data (field or remote sensing), and their levels of objectivity. The problem with these various approaches is they can lead to different hazard classifications for the same lake. Imja Tsho, located in the Everest region of Nepal, is an excellent example of a glacial lake that was classified as hazardous (ICIMOD, 2011), very low risk (Hambrey et al., 2008), and safe (Fujita et al., 2013). Unfortunately, these conflicting assessments shroud the lake's hazard in confusion as opposed to providing valuable information for the general public and communities downstream. Furthermore, previous studies have strictly performed assessments on the current state of glacial lakes despite these glaciers being highly dynamic systems. As the glaciers and their respective lakes evolve, the associated hazards may vary considerably, which makes it imperative to incorporate future projections of lake growth and glacier morphology into these assessments.

The aims of this research are to *(1) understand the evolution of debris-covered glaciers through the development of techniques that quantify the spatial variations of debris thickness and its respective impact on ablation rates and (2) develop an objective approach for assessing GLOF hazards that may be used to strengthen the management of these glacial lake systems and aid the implementation of successful risk-mitigation strategies.* These aims will be accomplished by (a) modeling the evolution of glaciers and their glacial lakes through the use of a debris-covered glacier energy balance model

in conjunction with lake expansion models derived from satellite imagery and (b) utilizing this information with other globally available data sets to classify the present and future hazard of GLOF events.

## **1.2 RESEARCH QUESTIONS**

The following research questions frame the body of this work:

1. How does debris cover affect the evolution of glaciers and glacial lakes in the Everest region of Nepal?
2. What underlying properties and processes are critical for modeling the ablation of debris-covered glaciers?
3. Can remotely sensed data be used to objectively quantify the hazards associated with dangerous glacial lakes?
4. What role should field campaigns serve in the management of glacial lakes?

## **1.3 HYPOTHESES**

The following hypotheses seek to address these research questions:

1. The spatial variations of debris thickness over a glacier may be derived using an energy balance model in conjunction with satellite imagery to understand the evolution of these glaciers and their glacial lakes.
2. The properties and processes that control the ablation of debris-covered glaciers can be accurately quantified using field techniques and energy balance models.
3. Remotely sensed assessments may be used to objectively classify the hazards associated with a potentially dangerous glacial lake.
4. Site-specific field data provides detailed information that is integral for accurately assessing the hazard of a GLOF and informing future risk-mitigation scenarios.

## **1.4 OUTLINE**

This body of work integrates field data, satellite imagery, and modeling to develop an understanding of the impacts of debris thickness on ablation rates and the hazards associated with glacial lakes on debris-covered glaciers. Chapter 2 provides a brief background regarding the evolution of debris-covered glaciers, details of debris-covered glacier energy balance models that are an integral part of this work, and an overview GLOFs and common triggering events. Chapter 3 applies the debris-covered glacier energy balance model to estimate debris thickness over glaciers in the Everest region (Rounce and McKinney, 2014). Chapter 4 applies the same energy balance model in conjunction with field data to understand the properties and processes that control ablation rates (Rounce et al., 2015). Chapter 5 transitions from debris-covered glaciers to their respective glacial lakes and applies a holistic approach using remotely sensed data to objectively classify the risk of a GLOF, which may be used to guide future glacial lake management actions (Rounce et al., In preparation for submission to Hydrology and Earth System Sciences, expected submission date: March 31, 2016). The main conclusions from this body of knowledge and how they address the aims of this study will be summarized in Chapter 6.

## Chapter 2: Background

### 2.1 EVOLUTION OF DEBRIS-COVERED GLACIERS

Approximately 10% of all glaciers in the Himalaya and Karakoram are debris-covered (Bolch et al., 2012), which fundamentally alters the ablation rates on the glacier. A thin layer of debris may enhance ablation, while a thick layer of debris retards ablation. The critical debris thickness beyond which the glacier is insulated by the debris is typically around 2-3 cm (Figure 2.1). For glaciers in the Everest region of Nepal, the debris thickness near the snout of the glacier is commonly greater than 0.5 m, while further upglacier the debris cover is thinner (Nicholson and Benn, 2012). These spatial variations of debris thickness have significant impacts on the evolution of the glacier.

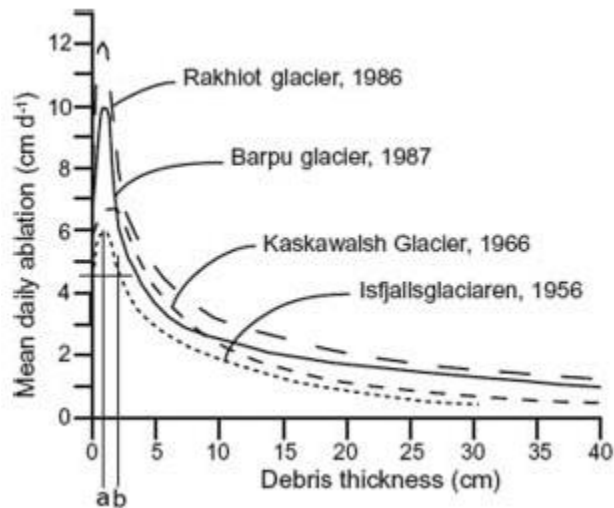


Figure 2.1: Empirical relationship between debris thickness and ablation rates for various glaciers throughout the world (Fig. 1 from Nicholson and Benn, 2006).

Benn et al. (2012) summarizes the response of glaciers in the Everest region to climate change in great detail (Figure 2.2). The debris thickness increases towards the snout of the glacier, which causes the ice near the equilibrium line altitude (ELA) to

ablate more rapidly. This differential melting alters the topographic gradient of the glacier, which reduces the glacier's velocity thereby causing the glacier to stagnate. In response to this stagnation, melt ponds form behind the terminal moraine due to the lack of influx of new glacier ice. These melt ponds act as heat sinks that promote the melting of the surrounding ice and over time may coalesce into a large glacial lake. In this manner, the spatial variation of debris thickness on a glacier is directly linked to its glacial lake. Unfortunately, quantifying the spatial variations of debris thickness is difficult due to the location of these glaciers and the time and effort required to conduct thickness measurements.

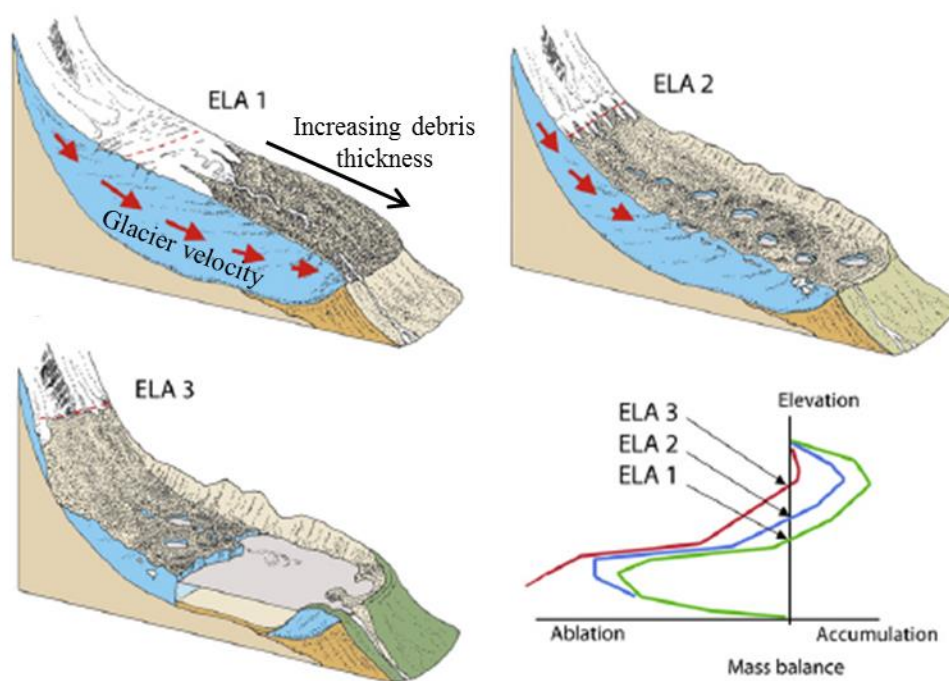


Figure 2.2: The evolution of glacial lakes on debris-covered glaciers as a function of climate change (adapted from Benn et al., 2012).

## 2.2 DEBRIS-COVERED GLACIER ENERGY BALANCE MODEL

Debris-covered glacier energy balance models are commonly used to derive debris thickness from satellite imagery (Nakawo and Rana, 1999; Suzuki et al., 2007; Zhang et al., 2011; Foster et al., 2012) or to estimate ablation rates (Nicholson and Benn, 2006; Reid et al., 2012; Collier et al., 2014; Fujita and Sakai, 2014). A typical debris-covered glacier energy balance model assumes the debris cover is steady-state as follows:

$$R_n + H + LE + P + Q_c = 0 \quad (2.1)$$

where  $R_n$  is the net radiation,  $H$  is the sensible heat flux,  $LE$  is the latent heat flux,  $P$  is the heat flux from precipitation, and  $Q_c$  is the conductive heat flux through the debris.

The net radiation is computed from the incoming shortwave, outgoing shortwave, incoming longwave, and outgoing longwave radiation, which are typically measured using an automatic weather station (AWS) or estimated by reanalysis data sets. The sensible heat flux accounts for the transfer of energy between the surface of the debris and the atmosphere based on their respective temperatures. The latent heat flux accounts for the transfer of energy between the surface and the atmosphere due to phase changes, which is typically the evaporation of moisture on the surface of the debris. The sensible and latent heat fluxes are referred to as turbulent heat fluxes and are commonly estimated using a bulk aerodynamic method (Nicholson and Benn, 2006; Reid and Brock, 2010). The heat flux supplied by precipitation accounts for the differences in temperature between the debris' surface and the precipitation. The conductive heat flux accounts for the propagation of heat from the surface through the debris layer to the glacier ice interface. This heat flux is typically estimated assuming a linear temperature profile

through the debris for time steps greater than 24 hrs (Nicholson and Benn, 2006) or may be modeled using an iterative approach to estimate the non-linear temperature profiles (Reid and Brock, 2010).

Imbedded within these various heat fluxes are specific debris properties that are required to apply the energy balance model. Net radiation requires knowledge of the albedo, which controls the amount of shortwave radiation absorbed by the debris. The turbulent heat fluxes require knowledge of the surface roughness, which governs the amount of energy transferred between the surface and the atmosphere. Lastly, the conductive heat flux requires detailed knowledge of the debris thickness and the thermal conductivity to determine the temperature of the debris. In the event that the surface temperature is known, the energy balance model may be used to solve for the debris thickness instead.

### **2.3 GLOF TRIGGERS AND PROCESS CHAIN**

GLOFs occur when the terminal moraine that is containing the lake is breached and unleashes stored lake water downstream. The most common triggering event for glacial lakes in the Himalaya is mass movement, i.e., an avalanche, rockfall, or landslide, entering the lake (Richardson and Reynolds, 2000; Emmer and Cochachin, 2013). The mass movement causes a displacement wave that propagates across the surface of the lake and potentially overtops the moraine depending on the freeboard of the terminal moraine (Figure 2.3). If the moraine is overtopped, the energy from the wave may begin eroding the moraine thereby causing a positive feedback in which the lake discharges more water and the outflow causes more erosion. The discharged volume of water from the wave overtopping and the lake emptying composes the flood water that may affect

downstream communities. The GLOF from Dig Tsho in 1985 is a good example of this process chain (Vuichard and Zimmerman, 1987).



Figure 2.3: The GLOF process chain for mass movement entering a glacial lake (Worni et al., 2014).

Mass movement entering the lake is the most common form of “dynamic” failure, which refers to a GLOF being caused by a sudden event. Other forms of dynamic failure include a flood from a lake situated upstream, intensive rainfall or snowmelt, the blocking of an outflow channel, and/or an earthquake (Emmer and Cochachin, 2013). These various events greatly alter the natural conditions of the lake by causing a displacement wave, eroding the terminal or lateral moraines, and/or rapidly increasing the water level thereby changing the pressure on the moraines. The other form of failure is referred to as “self-destructive” or “long-term” effects. This body of work uses the term self-destructive to avoid any confusion with a future dynamic failure that was made possible by the growth of a glacial lake. Self-destructive failures include the melting of a buried ice core in the moraine, the influence of hydrostatic pressure, and the effect of time, which refers to the slow degradation of a moraine over time (Emmer and Cochachin, 2013). Unfortunately, it is difficult to determine many self-destructive failures due to a lack of information regarding previous GLOFs and because self-

destructive failures are typically due to a combination of events. For example, the melting of a buried ice core weakens the stability of the moraine, which may result in the lake failing due to the hydrostatic pressure. Once the lake undergoes a self-destructive failure many similar processes within the GLOF process chain occur, i.e., the breach may cause a positive feedback of erosion, the flood propagates downstream, and, depending on the size of the breach, the flood may greatly impact the downstream communities.

Many studies have focused on modeling the GLOF process chain or particular sections of the chain. Westoby et al. (2014) provides a detailed review of the dam-breach and flood models that have commonly been used. The dam-breach models vary greatly depending on the available data and the level of detail, which range from simple empirical models (e.g., Somos et al., 2015) to complex physically-based models (e.g., Worni et al., 2014). Similarly, the propagation of the flood downstream may be estimated using geometric models that only consider the downstream elevations (e.g., Huggel et al. (2003)) or may be estimated using physically-based 1-D (e.g., Khanal et al., 2015) or 2-D models (e.g., Somos et al., 2015). The selection of a physically-based model versus a simpler model is typically based on the desired output. If the output is meant to provide a quick first look at the hazard of glacial lakes in a region, the study may use simplified models as a starting point (Bolch et al., 2011a). On the other hand, if the aim is to quantify the risk of a GLOF at a specific lake and develop flood maps for the downstream areas, then more complex physically-based models should be used (Worni et al., 2014).

# **Chapter 3: Debris thickness of glaciers in the Everest area (Nepal Himalaya) derived from satellite imagery using a nonlinear energy balance model**

David Rounce and Daene McKinney

Published in *The Cryosphere* 8:1317-1329, doi:10.5194/tc-8-1317-2014, 2014

## **3.1 ABSTRACT**

Debris thickness is an important characteristic of debris-covered glaciers in the Everest region of the Himalaya. The debris thickness controls the melt rates of the glaciers, which has large implications for hydrologic models, the glaciers' response to climate change, and the development of glacial lakes. Despite its importance, there is little knowledge of how the debris thickness varies over these glaciers. This paper uses an energy balance model in conjunction with Landsat7 ETM+ satellite imagery to derive thermal resistances, which is the debris thickness divided by the thermal conductivity. Model results are reported in terms of debris thickness using an effective thermal conductivity derived from field data. The developed model accounts for the nonlinear temperature gradient in the debris cover to derive reasonable debris thicknesses. Fieldwork performed on Imja-Lhotse Shar Glacier in September 2013 was used to compare to the modeled debris thicknesses. Results indicate that accounting for the nonlinear temperature gradient is crucial. Furthermore, correcting the incoming shortwave radiation term for the effects of topography and resampling to the resolution of the thermal band's pixel is imperative to deriving reasonable debris thicknesses. Since the topographic correction is important, the model will improve with the quality of the DEM. The main limitation of this work is the poor resolution (60 m) of the satellite's thermal band. The derived debris thicknesses are reasonable at this resolution, but trends related to slope and aspect are unable to be modeled on a finer scale. Nonetheless, the

study finds this model derives reasonable debris thicknesses on this scale and was applied to other debris-covered glaciers in the Everest region.

### **3.2 INTRODUCTION**

Debris-covered glaciers are common in the Everest area of the Himalaya. The debris cover has a large impact on the sub-debris ablation rate and hence the evolution of the glacier. A thin debris layer may enhance ablation by reducing the albedo causing the surface to absorb more radiation compared to clean ice, while a thicker debris layer will insulate the glacier causing the ablation rate to decrease. The critical thickness at which the debris cover reduces ablation is around 2 cm (Ostrem, 1959; Mattson et al., 1993; Kayastha et al., 2000). Field studies have supported these results showing that beyond this critical thickness, the melt rate greatly decreases (Nakawo and Young, 1981; Conway and Rasmussen, 2000; Nicholson and Benn, 2006; Reid and Brock, 2010; Reid et al., 2012). The role that debris cover has on the evolution of glaciers in the Everest area is summarized well by Benn et al. (2012). In short, the debris cover increases towards the tongue of the glacier, where the slopes are gentler. The spatial variation of debris cover causes the ablation to be predominately focused in areas of thinner debris behind the tongue of the glacier. The differential melting causes the tongue of the glacier to become stagnant and promotes the development of supraglacial lakes.

The sub-debris ablation rate is controlled by the debris thickness, the thermal properties of the debris, and meteorological conditions. The debris thickness may be measured by surveying exposed ice faces (Nicholson and Benn, 2012) or via manual excavation (Reid et al., 2012). Surveying exposed ice faces greatly reduces the amount of labor involved in measuring the debris thickness, but may not be representative of the entire glacier and is limited to regions with significant differential melting. Due to the

labor-intensive nature of this work, few other surveys of debris thickness have been performed in the Everest area (Nakawo et al., 1986). The thermal property associated with describing the debris cover is the effective thermal conductivity. Studies have found the thermal conductivity of debris cover in the Khumbu to range from 0.85 to 1.29 W m<sup>-1</sup> K<sup>-1</sup> (Conway and Rasmussen, 2000; Nicholson and Benn, 2012). The water content and lithology of the debris cover may partly explain the variation in thermal conductivity as the water content will change the effective thermal conductivity of the debris (Nicholson and Benn, 2006) and the lithology will influence the bulk volumetric heat capacity, which is used to derive the thermal conductivity (Nicholson and Benn, 2012).

In addition to the properties of the debris cover, the meteorological conditions will affect the sub-debris ablation rate. The net solar radiation has been found to be the main source of energy responsible for ablation on debris-covered glaciers (Inoue and Yoshida, 1980; Kayastha et al., 2000; Takeuchi et al., 2000); however, the turbulent heat fluxes are still significant (Brock et al., 2010). Many studies have modeled the energy balance on debris-covered glaciers with varying levels of success (Nakawo and Young, 1982; Nakawo et al., 1999; Han et al., 2006; Nicholson and Benn, 2006; Mihalcea et al., 2008b; Reid and Brock, 2010; Reid et al., 2012; LeJeune et al., 2013). These models integrate meteorological data from automatic weather stations with knowledge of the debris cover to solve for the surface temperature of the debris, which may then be used to calculate the sub-debris ablation rates. These models are limited by their knowledge of how the debris cover varies over the glacier or they require a great deal of site-specific information.

This has led other studies to use satellite imagery to derive the properties of the debris cover. These studies use surface temperature data from satellite imagery in conjunction with an energy balance model to solve for the thermal resistance, which is

the debris thickness divided by the thermal conductivity (Nakawo and Rana, 1999; Nakawo et al., 1999; Suzuki et al., 2007; Zhang et al., 2011). If the thermal conductivity of the debris is known, the model can solve directly for debris thickness (Foster et al., 2012). Mihalcea et al. (2008a) used a different approach by deriving debris thickness from linear relationships between surface temperature and debris thickness for different elevation bands.

One problem associated with the studies that solved for the thermal resistance is that while the spatial distribution of thermal resistances typically agreed well, the actual values of thermal resistances were significantly lower than those derived from field studies. Suzuki et al. (2007) attributed their low thermal resistances to the mixed pixel effect, which refers to the pixels in the satellite imagery comprising supraglacial ponds, ice cliffs, and bare ice areas. Nakawo and Rana (1999) also commented on areas with exposed ice cliffs reducing the surface temperature of the pixel, thereby lowering the calculated thermal resistances. Zhang et al. (2011) did not address the low values of thermal resistances, but did attribute the small disagreement between modeled and observed melt rates to the unknown variations in meteorological conditions caused by altitude, aspect, and shading in different areas, as well as the unknown nature of water content in the debris. The mixed pixel effect and the spatial variation in meteorological conditions may reduce the thermal resistances, but it is unlikely to cause the satellite-derived thermal resistances to be one or two orders of a magnitude lower than those found in the field.

Foster et al. (2012) is the first study, to the authors' knowledge, that accurately derives debris thickness from satellite imagery. The model uses a DEM generated from an airborne lidar survey and compares the results of a sloped model, which accounts for variations in topography, and a flat model. The sloped model resulted in thicker debris

areas when compared to the flat model, but also identified some pixels as having unrealistically high or negative debris thicknesses. These errors occurred in pixels with steep slopes and high surface temperatures and were replaced with the values from the flat model. Unfortunately, the model is difficult to transfer to other glaciers because a great deal of site-specific data was used. Their modifications to their energy balance include the addition of a heat storage term that is a fraction of the ground heat flux and an empirical relationship between the surface temperature and air temperature. The relationship between the surface and air temperature was used to reduce the values of sensible heat flux, since initial results using an instability correction were found to be unrealistically high.

We report a method for deriving the debris thickness of debris-covered glaciers using an energy balance model with Landsat7 ETM+ satellite imagery and apply the method in the Everest region of Nepal. The performance of various models is assessed via comparison with field data. First, the use of an approximation factor that accounts for the nonlinear temperature gradient of the debris cover is investigated. This simple nonlinear energy balance model is then used to compare a flat model with a sloped model, which accounts for the variations in topography. The affect of the quality of the DEM is then explored by comparing DEMs of different resolutions. Lastly, the model is applied to other glaciers in the Everest region.

### **3.3 DATA**

#### **3.3.1 Meteorological data**

The energy balance model uses meteorological data from an automatic weather station, Pyramid Station (27.959°N, 86.813°E, 5035 m a.s.l), which is located next to the Khumbu glacier (Figure 3.1). Pyramid Station (SHARE network operated by EV-K<sup>2</sup>-

CNR Committee) provides a continuous record of hourly measurements of air temperature, wind speed, incoming shortwave radiation, and incoming longwave radiation from October 2002 to December 2009. All the meteorological data are assumed to be constant over the Khumbu region, except for air temperature and incoming shortwave radiation in the sloped model. The air temperature was adjusted based on the elevation of each pixel using a lapse rate of  $6.5 \text{ K km}^{-1}$ . In the sloped model, the incoming shortwave radiation term was corrected for the effects of topography, altitude, and shading similar to the methods of Hock and Noetzli (1997). The hillshade tool in ArcGIS was used to determine if any pixels were shaded from the surrounding terrain based on the position of the sun at the time the satellite images were taken. The flat model also corrects for the effects of shading due to surrounding terrain, but assumes each pixel has a slope and aspect of zero.

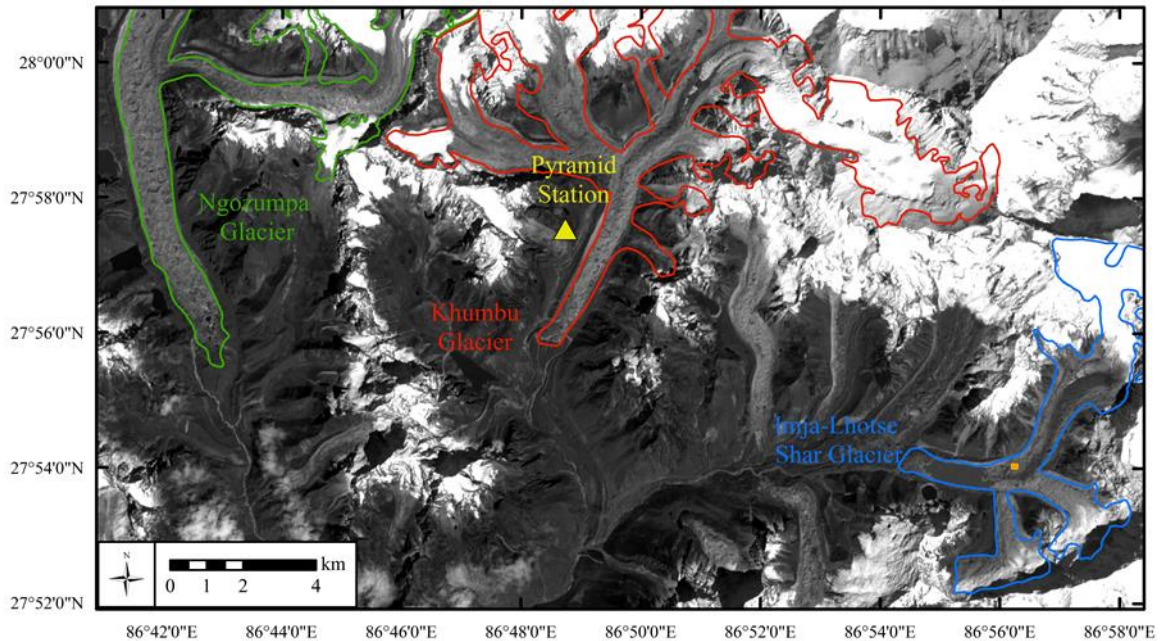


Figure 3.1: Panchromatic band from Landsat7 on 04 Oct 2002 showing Imja Lake, the focus area on Imja-Lhotse Shar Glacier, and Pyramid Station amongst debris-covered glaciers in the Everest region.

### 3.3.2 Remotely sensed data

Landsat7 ETM+ (hereon referred to as Landsat7) satellite imagery over the same period as the meteorological data was used to derive the thermal resistance of the debris. All clear-sky images from the same period of time that meteorological data are available in the melt season were used. The melt season was defined as 15 May to 15 October, which is the time period where the daily mean temperature in the debris was above freezing (Nicholson, 2005). Twelve Landsat7 images met this criterion (Table 3.1). Figure 3.2 shows an example of the Landsat imagery and the corresponding meteorological data from Pyramid Station from 04 October 2002. All scenes were

downloaded from the NASA Land Processes Distributed Active Archive Center (NASA LP DAAC, 2011).

Table 3.1: Overview of satellite imagery used in this study.

<b>Satellite</b>	<b>Year</b>	<b>Date</b>	<b>Purpose</b>	<b>Resolution (m)</b>
Landsat 7	2002	04 Oct	Ts	60
Landsat 7	2003	16 May	Ts	60
Landsat 7	2004	07 Sept	Ts	60
Landsat 7	2004	09 Oct	Ts	60
Landsat 7	2005	21 May	Ts	60
Landsat 7	2005	12 Oct	Ts	60
Landsat 7	2007	27 May	Ts	60
Landsat 7	2007	28 June	Ts	60
Landsat 7	2007	02 Oct	Ts	60
Landsat 7	2008	29 May	Ts	60
Landsat 7	2008	02 Sept	Ts	60
Landsat 7	2009	17 June	Ts	60
ALOS PRISM	2006	04 Dec	DEM	2.5
ASTER	2000 - 2008		DEM	15-50

The processing level of the Landsat7 images were all L1T indicating the images were all geometrically rectified using ground control points (GCPs) from the 2005 Global Land Survey in conjunction with the 90 m global DEM generated by the Shuttle Radar Topographic Mission (SRTM). Landsat7 satellite imagery comprises 8 different bandwidths with various resolutions. The two bands of interest here are the thermal band (Band 6) and the panchromatic band (Band 8). The thermal band has a resolution of 60 m, but is automatically resampled to 30 m and was used to derive surface temperature (Figure 3.2) according to NASA (2011). It was atmospherically corrected using the methods described by Coll et al. (2010). The required meteorological data for the

MODTRAN 4 model used by Coll et al. (2010) was taken from Pyramid Station. The image-to-image co-registration for Landsat7 is 7.3 m and the uncertainty of the derived surface temperature data is estimated to be  $\pm 1.0$  K (Barsi et al., 2003; Coll et al, 2010; Coll et al, 2012). The panchromatic band has a horizontal resolution of 15 m and was used to co-register the images.

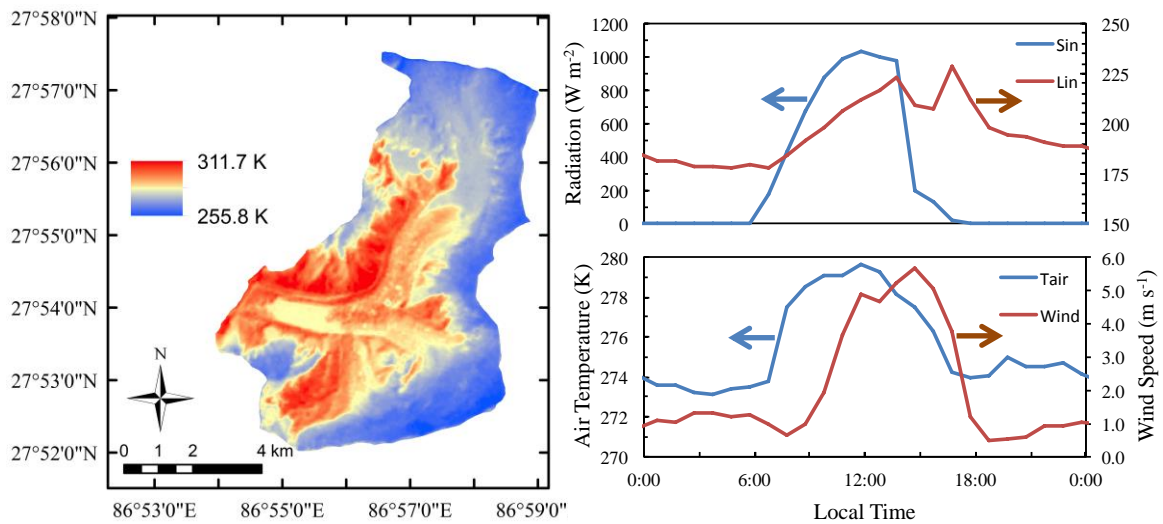


Figure 3.2: Surface temperature derived from Landsat7 imagery (left) and corresponding meteorological data (right) on 04 October 2002.

The high resolution DEM used in this study was generated by Lamsal et al. (2011) from Advanced Land Observing Satellite (ALOS) PRISM images. The generated DEM has a horizontal resolution of 5 m and relative error of  $\pm 4$  m. In order to co-register the DEM with the panchromatic band from the Landsat7 imagery, a shaded version of the DEM was generated using the Hillshade tool in ArcGIS 10.3. The swipe visualization tool in PCI Geomatica 2013 showed that the images were properly co-registered without any further processing. The coarser resolution global DEM used in this study was the ASTER GDEM, which is composed of automatically generated DEMs

from the Advanced Spaceborne Emission and Reflection radiometer (ASTER) stereo scenes acquired from 2000-present (METI/NASA/USGS, 2009). Nuth and Kaab (2011) found the accuracy of the ASTER GDEM to be similar to the validation summary (METI/NASA/USGS, 2009) when applied to debris-covered glaciers in New Zealand. They found the ASTER GDEM to have biases up to 10 m and RMSE of 5-50 m. The horizontal resolution of the ASTER GDEM has been found to be better than 50 m (Fujisada et al, 2005). The swipe visualization tool in PCI Geomatica 2013 was used with a shaded version of the ASTER GDEM to confirm that the images were properly co-registered. While residual anomalies and artifacts may exist in this experimental/research grade product, it has been used in this study to develop an understanding of how the quality of DEM will affect the thermal resistances.

### **3.3.3 Field data**

#### ***3.3.3.1 Study site***

Field research was conducted in September 2013 on the debris-covered portion of Imja-Lhotse Shar Glacier (27.901°N, 86.938°E, ~5050 m a.s.l.). Imja-Lhotse Shar Glacier refers to two debris-covered glaciers, Imja glacier (the southeastern component; ~4.5 km to the confluence) and Lhotse Shar Glacier (the northeastern component; ~3.5 km to the confluence), that converge and terminate into Imja Lake (Figure 3.1). The third glacier that is present south of Imja Lake is Amphu glacier, which appears to no longer contribute to Imja-Lhotse Shar Glacier. Imja and Lhotse Shar Glacier are both avalanche fed and extend from the calving front of Imja Lake (5010 m) up to elevations of 7168 and 8383 m for Imja and Lhotse Shar Glacier, respectively. The thickness of debris cover on Imja-Lhotse Shar Glacier increases towards the terminal moraine of the glacier and is primarily composed of sandy boulder-gravel (Hambrey et al., 2008). The debris cover

extends up to elevations of 5200 and 5400 m on Imja and Lhotse Shar Glacier, respectively. From the calving front of Imja Lake to the confluence of the glacier, the elevation increases less than 50 m, which is consistent with the findings of Quincey et al. (2007) that the tongue of the glacier is relatively stagnant with a surface gradient less than 2°. The debris cover has a hummocky terrain with melt ponds and exposed ice faces scattered throughout.

### ***3.3.3.2 Debris measurements***

Debris thermistors (TR-52 ThermoRecorder, T&D Corporation) were installed at four locations (referred to as LT1, LT2, LT3, and LT4) at depths of 0, 5, 10, 15, 20, 30 cm, and at the debris/ice interface. The debris thickness was 31, 47, 36, and 40 cm for LT1, LT2, LT3, and LT4, respectively. Holes were excavated to the debris/ice interface and as the thermistors were installed, the debris was replaced in its original position as best as possible. The thermistors recorded temperature at hourly intervals from 13 September to 24 September. The first 48 hours of data for each thermistor was discarded to allow the thermistors to equilibrate with the debris. One of the surface thermistors malfunctioned on 23 September, so the data from this thermistor beyond this date was discarded.

Debris thickness measurements were performed at 25 locations and were concentrated in one melt basin (27.901°N, 86.938°E, 5045-5055 m a.s.l.) that appeared to be formed by differential melting and backwasting (Figure 3.1). The melt basin was selected as the focus area of this study because it appeared to be representative of the hummocky terrain on Imja-Lhotse Shar Glacier and was relatively easy to access. The melt basin was approximately 120 m long and 60 m wide with a topographic low in the center of the basin (5045 m a.s.l.) and a topographic high on the perimeter of the basin

(5055 m a.s.l.). The elevation of the melt basin was only 10-20 m higher than the elevation of Pyramid Station. To the best ability of the authors, the measurements were performed randomly throughout the melt basin. Measurements were conducted via manual excavation using a tape measure at 23 of the 25 sites. This process involved digging holes to the ice surface and measuring the perpendicular distance from the ice surface to the surface of the debris. The other two sites were the debris on top of an ice face, which was measured using a laser range finder (TruPulse 360B) because the ice face could not be accessed safely on foot. Twelve debris thickness measurements were also performed outside of the melt basin to understand if the melt basin was representative of the debris-covered glacier. More debris thickness measurements were unable to be made due to time and labor restraints. Furthermore, the maximum depth of excavation was 1 m because further excavation was too physically demanding.

### **3.4 METHODS**

#### **3.4.1 Energy balance model**

The energy balance model used in this study is a steady state surface energy balance for the debris cover similar to that developed by Nakawo and Young (1982)

$$R_n + LE + H - Q_c = 0 \quad (3.1)$$

where  $R_n$  is the net radiation flux,  $H$  is the sensible heat flux,  $LE$  is the latent heat flux (assumed to be zero), and  $Q_c$  is the ground heat flux (all in  $W\ m^{-2}$ ).

The net radiation flux includes the shortwave radiation flux and the longwave radiation flux

$$R_n = S \downarrow (1 - \alpha) + \varepsilon(L \downarrow - \sigma T_s^4) \quad (3.2)$$

where  $S \downarrow$  is the incoming shortwave radiation ( $\text{W m}^{-2}$ ),  $\alpha$  is the albedo (0.30),  $\varepsilon$  is the emissivity assumed to be 0.95 (Nicholson and Benn, 2006),  $L \downarrow$  is the incoming longwave radiation ( $\text{W m}^{-2}$ ),  $\sigma$  is the Stefan-Boltzmann constant ( $5.67 \times 10^{-8} \text{ W m}^{-2} \text{ K}^{-4}$ ), and  $T_s$  is the surface temperature (K). For the sloped model, incoming shortwave radiation was corrected for the effects of topography, altitude, and shading similar to the methods of Hock and Noetzli (1997). The flat model assumes that each pixel has a slope and aspect of 0 degrees. The incoming longwave radiation and surface albedo were assumed to be constant over the entire debris cover. The albedo used in this study (0.30) was the average albedo of the debris cover on Ngozumpa glacier (Nicholson and Benn, 2012).

The latent heat flux was assumed to be zero based on the assumption that the debris cover is dry. The sensible heat flux was tested using two approaches: (1) assuming a neutral atmosphere (Nicholson and Benn, 2006) and (2) correcting for the unstable atmosphere (Reid and Brock, 2010). It is likely that high debris temperatures and low air temperature would cause an unstable atmosphere above the surface of the debris; however, the incorporation of the stability correction caused the sensible heat fluxes to be unrealistically high similar to the initial results of Foster et al. (2012). Therefore, this study calculates the sensible heat flux assuming a neutral atmosphere according to Nicholson and Benn (2006)

$$H = \rho_{\text{air}} \left( \frac{P}{P_0} \right) c_{\text{Au}} (T_{\text{air}} - T_s) \quad (3.3)$$

where

$$A = \frac{k_{vk}^2}{\ln\left(\frac{z}{z_0}\right)\ln\left(\frac{z}{z_0}\right)} \quad (3.4)$$

where  $\rho_{air}$  is the density of air ( $1.29 \text{ kg m}^{-3}$ ),  $P$  is the atmospheric pressure computed using the barometric pressure formula,  $P_0$  is the atmospheric pressure at sea level ( $101,325 \text{ Pa}$ ),  $c$  is the specific heat capacity of air ( $1010 \text{ J kg}^{-1} \text{ K}^{-1}$ ),  $A$  is the dimensionless transfer coefficient,  $u$  is the wind speed at Pyramid Station,  $T_{air}$  is the air temperature two meters above the surface calculated using a lapse rate of  $6.5 \text{ K km}^{-1}$ ,  $k_{vk}$  is Von Karman's constant ( $0.41$ ),  $z$  is the height of meteorological measurements ( $2 \text{ m}$ ), and  $z_0$  is the surface roughness length (assume  $z_0 = 0.016$ ).

The ground heat flux is different for the linear and the nonlinear models

$$\text{Linear Model:} \quad Q_c = \frac{(T_s - 273.15)}{TR} \quad (3.5)$$

$$\text{Nonlinear Model:} \quad Q_c = G_{ratio} \frac{k_{eff}(T_s - 273.15)}{d} \quad (3.6)$$

where  $G_{ratio}$  is the nonlinear approximation factor,  $k_{eff}$  is the effective thermal conductivity ( $\text{W m}^{-1} \text{ K}^{-1}$ ), and  $d$  is the debris thickness ( $\text{m}$ ). In this study, the modeled results will derive debris thickness assuming an effective thermal conductivity from section 4.1. However, this model can also be applied to solve for the thermal resistance in the event that the effective thermal conductivity is unknown. The linear model assumes the temperature gradient in the debris is linear from the surface temperature to the debris/ice interface, which is assumed to be at  $273.15 \text{ K}$ . At the time that Landsat7 images are acquired ( $10:15$  local time), this linear assumption is not accurate.  $G_{ratio}$  is

used to approximate the nonlinear temperature variation in the debris. A linear temperature gradient in the upper 10 cm of the debris is used to make this approximation.  $G_{ratio}$  is therefore defined as the ratio of the linear temperature gradient in the upper 10 cm of the debris to the linear temperature gradient throughout the entire debris

$$G_{ratio} = \frac{-k_{eff} \frac{(T_S - T_{0.1m})}{0.1}}{-k_{eff} \frac{(T_S - T_d)}{d}} = \frac{(T_S - T_{0.1})}{(T_S - T_d)} * \frac{d}{0.1} \quad (3.7)$$

where  $T_{0.1m}$  is the temperature 10 cm below the surface of the debris and  $T_d$  is the temperature at the debris/ice interface (273.15 K). As the Landsat7 images are acquired at 10:15 and the thermistors recorded hourly temperatures, the temperatures in the debris at 10:15 were computed by linearly interpolating between 10:00 and 11:00. These interpolated temperatures were used to compute  $G_{ratio}$ .

## 3.5 FIELD RESULTS

### 3.5.1 Thermal conductivity

The effective thermal conductivity,  $k$ , of the debris cover was computed following the methods in Conway and Rasmussen (2000) assuming a density ( $\rho = 2700 \text{ kg m}^{-3}$ ) and a specific heat capacity ( $c = 750 \text{ J kg}^{-1} \text{ K}^{-1}$ ) of rock. The average effective thermal conductivity was calculated to be  $0.96 (\pm 0.33) \text{ W m}^{-1} \text{ K}^{-1}$ . This effective thermal conductivity agrees well with other thermal conductivities computed in this area, which range from  $0.85$  to  $1.29 \text{ W m}^{-1} \text{ K}^{-1}$  (Conway and Rasmussen, 2000; Nicholson and Benn, 2012). The thermal conductivity was greatly influenced by depth as the average values above and below 10 cm were  $0.60$  and  $1.20 \text{ W m}^{-1} \text{ K}^{-1}$ , respectively. The drastic difference in thermal conductivity above and below 10 cm is likely due to the amount of water content in the debris. Nicholson and Benn (2006) found the thermal conductivity

of wet debris (assuming the pores were saturated with water) to be two to three times larger than dry debris. These results indicate that the top 10 cm of the debris is dry, while 15 cm and lower is wet. This is consistent with observations in the field, where approximately the top 10 cm of the debris was dry and below this depth the debris was wet. The observed moisture in the debris was mainly the wetted surface of the grains.

### **3.5.2 Debris thickness**

The debris thickness in this melt basin ranged from bare ice (0 cm) to depths greater than 1 m (Figure 3.3). The average debris thickness, assuming a maximum thickness of 1 m, was 0.42 ( $\pm 0.29$ ) m. These debris thicknesses are consistent with the debris thickness of other debris-covered glaciers in the Everest region (Nakawo et al., 1986; Nicholson and Benn, 2012). Debris thicknesses greater than 1 m were found in the bottom of these melt basins where the debris had likely accumulated over time due to differential melting and backwasting of the debris cover. Areas of thin debris cover were located on the slopes of the melt basin. These trends are identical to those found by Nicholson and Benn (2012) and were also observed at the 12 other sites where debris thickness was measured outside of the melt basin. There did not appear to be any trends in debris thickness with respect to aspect. Ideally, debris thickness would be sampled over the entire debris-covered glacier to derive a debris thickness map that could be used to validate the modeled results. As this was not feasible due to restraints on time and labor, the modeled results from within this melt basin and the melt basin's adjacent cells will constitute the focus area of the satellite imagery that will be compared to the measured debris thicknesses to qualitatively assess the reasonableness of the modeled results.

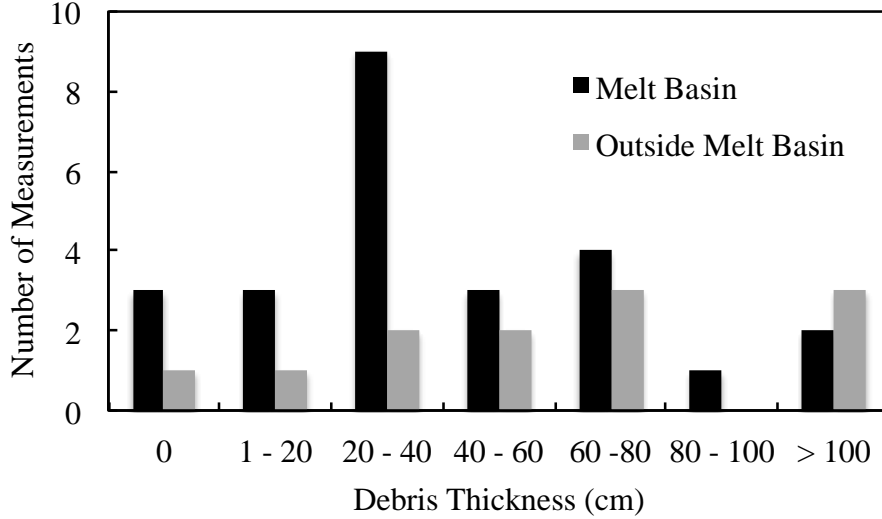


Figure 3.3: Debris thickness measurements on Imja-Lhotse Shar Glacier inside and outside of the melt basin.

### 3.5.3 Nonlinear approximation factor, $G_{ratio}$

$G_{ratio}$  was computed from all the temperature profiles based on the interpolated temperatures at 10:15. Figure 3.4 shows the temperature profiles at site LT3 and a schematic of the temperature gradients used to compute  $G_{ratio}$ . Figure 3.4 shows the temperature at the debris/ice interface was  $0^{\circ}\text{C}$  for each day at site LT3 at 10:15. The temperature remained at  $0^{\circ}\text{C}$  for all the sites throughout the entire study period. The average value of  $G_{ratio}$  for the melt basin was  $2.7 (\pm 0.4)$ . The depth used to approximate the nonlinear temperature gradient was found to greatly influence  $G_{ratio}$ , where  $G_{ratio}$  decreased as the depth increased (Figure 3.5). This relationship was expected because as the depth used to calculate  $G_{ratio}$  approaches the thickness of the debris,  $G_{ratio}$  will approach a value of 1. Ideally, the nonlinear temperature gradient would be approximated by a linear temperature gradient in the upper 1 cm of the debris or smaller.

However, these measurements could not practically be performed in the field. Figure 3.5 shows the values of  $G_{\text{ratio}}$  derived using depths of 5 and 10 cm ( $2.9 \pm 0.8$  and  $2.7 \pm 0.4$ , respectively) are similar; however, the standard deviation of those derived from 5 cm is much larger than those derived from 10 cm. As the two values were similar,  $G_{\text{ratio}}$  derived from a depth of 10 cm was used in this study.

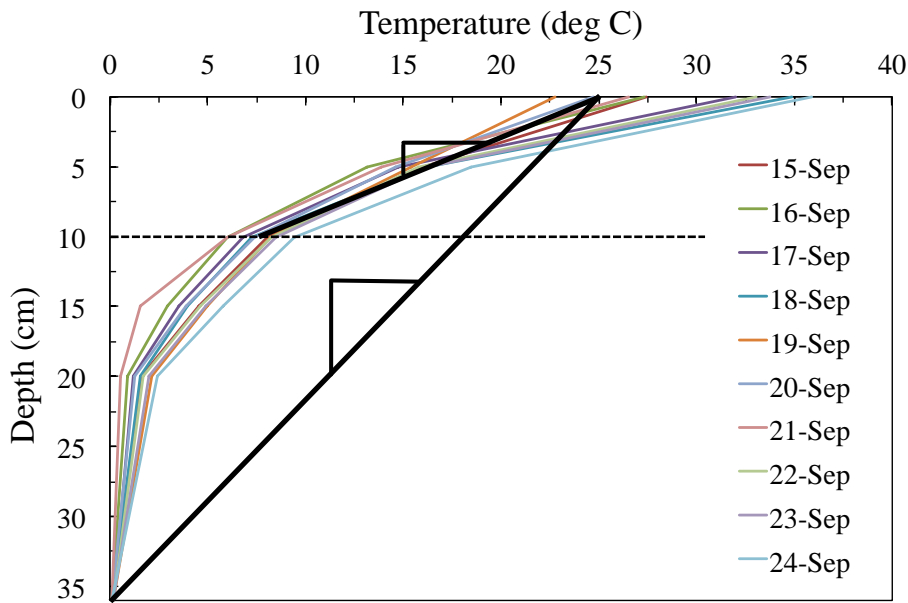


Figure 3.4: Temperature profiles at site LT3 at 10:15 with the temperature gradients used to compute  $G_{\text{ratio}}$  identified.

The other trend that may be expected is for  $G_{\text{ratio}}$  to increase as the surface temperature increases. However, Figure 3.5 shows that there is little correlation ( $R^2 = 0.29$ ) between surface temperature and  $G_{\text{ratio}}$  based on the data from all four sites. When the  $G_{\text{ratio}}$  values are removed from site LT4, there appears to be a stronger relationship ( $R^2 = 0.74$ ), but there is no physical justification for removing this data. Therefore, this

study uses an average value of  $G_{\text{ratio}}$  of 2.7. Conway and Rasmussen (2000) is the only other study, to the author's knowledge, that has measured temperature profiles in the Everest area with a small enough spacing (maximum 10 cm) between thermistors to compute  $G_{\text{ratio}}$ . The values derived from their temperature profiles at Everest Base Camp on May 21-23, 1999 were 3.0, 2.6, and 2.6, respectively. This good agreement lends confidence to the use of  $G_{\text{ratio}}$  in the Everest area.

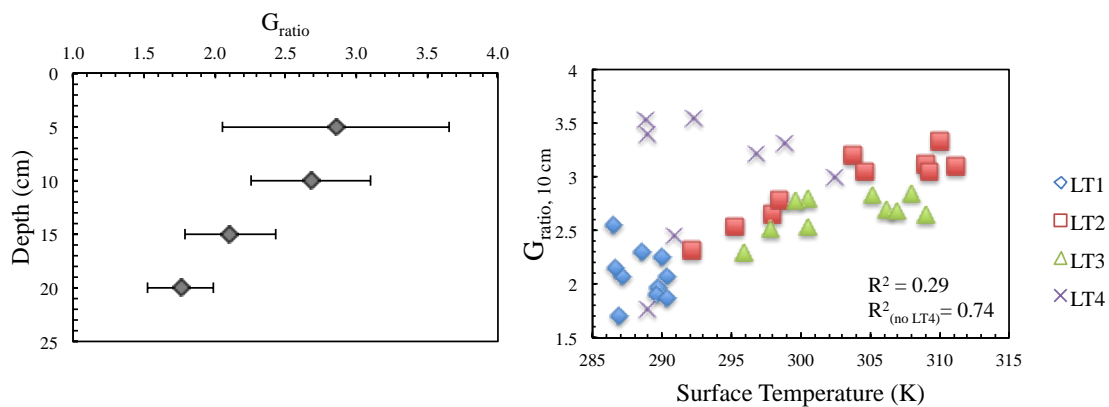


Figure 3.5:  $G_{\text{ratio}}$  as a function of depth (left) and corresponding  $G_{\text{ratio}}$  values at 10 cm depth for each sensor (right).

Foster et al. (2012) noted that the variation in surface temperature is very sensitive to small changes in debris thickness less than 0.5 m, while its change is very gradual for thicker debris. This caused them to have a high level of uncertainty in mapping debris thickness greater than 0.5 m. The debris thickness of the four sites used to derive  $G_{\text{ratio}}$  ranged from 0.31 to 0.47 m, which approaches the upper limit of 0.5 m. This lends confidence to the use of  $G_{\text{ratio}}$  for mapping debris thickness greater than 0.31 m. However, for regions with much smaller debris thicknesses, e.g. Miage Glacier (Reid et al., 2012), where a significant amount of the debris is less than 10 cm thick, it is possible that  $G_{\text{ratio}}$  will be different. Future work should determine the value of  $G_{\text{ratio}}$  for thin

debris layers in addition to determining how  $G_{\text{ratio}}$  varies over the melt season and how  $G_{\text{ratio}}$  is influenced by temperature.

### **3.6 MODELED RESULTS**

#### **3.6.1 Nonlinear sloped model – 5 m pixels**

The nonlinear sloped model accounts for the nonlinear temperature gradient in the debris cover using the  $G_{\text{ratio}}$  approximation factor and corrects the incoming solar radiation at each pixel for the effects of topography and shading. Initially, the model was applied and solved for every individual pixel at a resolution of 5 m. The average debris thickness in the focus area was 0.27 ( $\pm 0.19$ ) m with 17 of the 1080 pixels being undefined. All of the pixels that were undefined were pixels that were shaded by the surrounding terrain causing their net radiation to be very low. These debris thicknesses agree fairly well with the debris thickness observed on Imja-Lhotse Shar Glacier (Figure 3.3), although there are fewer pixels that with very high debris thickness ( $> 0.5$  m). This is likely due to the lack of variation in surface temperature when the debris is greater than 0.5 m as Foster et al. (2012) discussed.

One problem with the modeled results was there were clear trends with respect to slope and aspect (Table 3.2). Table 3.2 shows the average debris thickness increases with increasing slope, which is the opposite trend observed in the field. Furthermore, there was a clear trend with respect to aspect where east facing pixels had the smallest debris thickness, followed by north and south facing pixels, while west facing pixels had the highest values of debris thickness. This trend was not observed in the field. These trends occur from the corrections that are applied to the sloped model to account for the topography and surrounding terrain. Pixels that have steeper slopes are angled such that the incoming solar radiation is reduced. This reduces the net radiation, which lowers the

net energy flux (net radiation and turbulent heat fluxes) used to derive the debris thickness. In some cases, the net energy flux is negative, which causes a pixel to be undefined. Otherwise, the net energy flux is positive, but small, which results in large values of debris thickness. A minimum threshold for the net energy flux of  $10 \text{ W m}^{-2}$  was set, such that unrealistically high debris thicknesses would be classified as undefined. The same changes in incoming solar radiation occur with respect to aspect, where east facing pixels are oriented towards the sun thereby increasing the amount of incoming solar radiation compared to west facing pixels where the opposite occurs. Therefore, despite the modeled debris thickness yielding reasonable results, the model is incapable of capturing the fine local variations.

Table 3.2: Modeled results for the nonlinear sloped and flat model in the focus area with the high resolution DEM showing trends in debris thickness ( $d$ ), surface temperature ( $T_s$ ), and net radiation ( $R_n$ ) with respect to slope and aspect.

Topographic Parameter	Sloped Model (Focus Area)			Flat Model (Focus Area)			
	Average $d$ (m)	Average $T_s$ (K)	Average $R_n$ ( $\text{W m}^{-2}$ )	Average $d$ (m)	Average $T_s$ (K)	Average $R_n$ ( $\text{W m}^{-2}$ )	
Slope	0 - 5	0.17	290.44	448	0.16	290.44	451
	5 - 10	0.18	290.34	448	0.16	290.34	468
	10 - 20	0.23	290.35	457	0.16	290.35	506
	20 - 30	0.38	290.44	420	0.16	290.44	501
	> 30	0.55	290.33	328	0.16	290.33	524
Aspect	N	0.31	290.54	418	0.17	290.54	498
	W	0.32	290.32	399	0.16	290.32	498
	S	0.21	290.26	471	0.16	290.26	485
	E	0.15	290.49	535	0.16	290.49	501

Derived debris thicknesses do not capture local variations with respect to slope and aspect due to the poor resolution of the thermal band. The thermal band has a resolution of 60 m (automatically resampled to 30 m), which causes the surface temperatures over the 60 m pixel to be combined. This is referred to as the mixed-pixel effect. Conventionally, the mixed-pixel effect has been used to explain how bare ice faces reduce the surface temperature of the pixel causing the derived debris thickness or thermal resistance to be low. While this may be true, the mixed-pixel effect also explains how local variations in surface temperature are not properly accounted for. Table 3.2 reveals that the average surface temperature in the focus area is almost constant and does not vary with respect to slope or aspect. A higher resolution thermal band would show higher surface temperatures on south and east facing slopes, since their orientation allows them to receive more incoming shortwave radiation throughout the morning. North and west facing slopes that do not receive radiation would have lower surface temperatures, which would reduce the derived debris thickness. The mixed-pixel effect explains why the modeled results agree well with the average measured values, but do not capture the local variations. One way to overcome this problem is to apply the corrections to the incoming solar radiation and then resample these values of incoming solar radiation to be consistent with the surface temperature pixels (30 m). Ideally, the values of incoming solar radiation would be resampled to a 60 m resolution, since this is the resolution of the thermal band. However, this cannot be performed since the Landsat7 L1T product automatically resamples the thermal band to 30 m. The rest of the results shown in this study compute the incoming solar radiation, air temperature, and pressure for each pixel and then average these values to a resolution of 30 m. The debris thickness is then derived at this 30 m resolution.

### **3.6.2 Nonlinear sloped model – 30 m pixels**

The debris thickness derived using the nonlinear sloped model with 30 m pixels on Imja-Lhotse Shar Glacier are shown in Figure 3.6A. Only two pixels on the entire glacier are classified as undefined. These pixels were almost completely shaded by surrounding terrain and had predominately north and west facing aspects. This is a substantial improvement to the model's performance and shows the importance of resampling the corrected incoming solar radiation. The modeled results also reveal that the debris is thick on the terminal moraine with most pixels having values greater than 0.40 m. Behind the calving front of Imja Lake the debris is also thick, especially in the center of Imja-Lhotse Shar Glacier. This region of thick debris in the middle of Imja-Lhotse Shar Glacier is likely a result of the slope being more gentle thereby allowing debris to accumulate. Furthermore, this portion of the glacier receives debris from both Imja and Lhotse Shar Glacier since it is downstream for their confluence. The latter likely explains why the debris is thinner towards the lateral moraines and thicker in the center. Further up glacier on Imja and Lhotse Shar Glacier, the debris cover thins, which is expected because the slopes are steeper and they are approaching areas of clean ice on each glacier. These trends in which the debris is thicker on the moraine and thins upglacier are consistent with debris-covered thickness surveys performed on the Khumbu glacier (Nakawo et al., 1986) and Ngozumpa glacier (Nicholson and Benn, 2012).

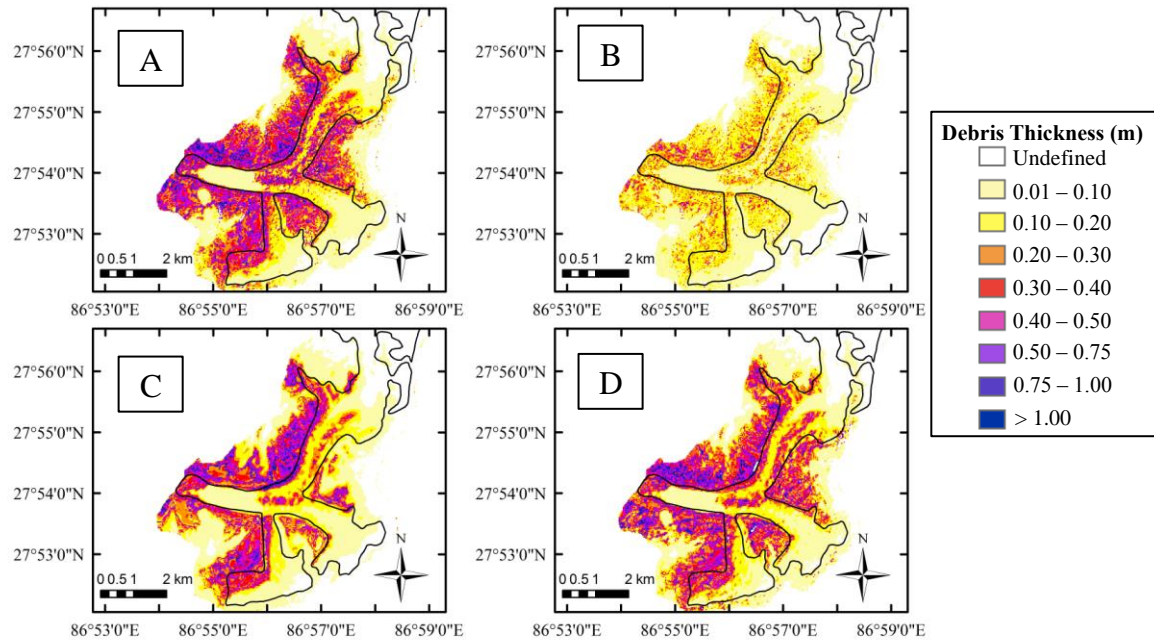


Figure 3.6: Debris thickness (m) with 30 m pixels using the (A) nonlinear sloped model, (B) linear sloped model, (C) nonlinear flat model, and (D) using the ASTER GDEM with the nonlinear sloped model.

The modeled debris thickness in the focus area had an average debris thickness of 0.29 ( $\pm 0.13$ ) m. These debris thicknesses agree fairly well with those measured on the glacier (Figure 3.3) with the exception of the high debris thicknesses ( $> 0.5$  m) being underrepresented as previously discussed. The lack of ability in modeling debris thickness greater than 0.5 m is problematic for estimates of total volume or mass of debris on the glacier. However, if the debris thickness is used to estimate ablation rates, then this limit of 0.5 m is not a problem because there is little change in the ablation rates for debris greater than 0.5 m thick. If a limit of 0.5 m is applied to the field measurements such that any debris thickness greater than 0.5 m is given a value of 0.5 m, then the average debris thickness would be 0.34 ( $\pm 0.18$ ) m. If the same limit is applied to the modeled debris thickness the average is 0.28 ( $\pm 0.11$ ) m, which agrees quite well.

### **3.6.3 Linear sloped model – 30 m pixels**

The debris thicknesses derived using the linear sloped model (Figure 3.6B) are significantly smaller than those using the nonlinear model (Figure 3.6A). The same trends indicating thicker debris on the moraine and behind the calving front with thinner debris upglacier are apparent. The only difference is the nonlinear approximation factor is not included in the linear model, which causes all the debris thicknesses to be 2.7 times smaller than the nonlinear model. The average debris thickness in the focus area is 0.11 ( $\pm 0.05$ ) m. These results indicate that the linear model severely underestimates the debris thickness and show that it is critical to account for the nonlinear temperature profile.

### **3.6.4 Nonlinear flat model – 30 m pixels**

One method to fill in the undefined pixels from the sloped model is to use a flat model (Foster et al., 2012). Figure 3.6C shows the debris thickness map derived from the nonlinear flat model. The flat model captures the trends of greater debris thickness on the terminal moraine and behind the calving front with thinner debris upglacier. However, these trends are not as prominent as in the sloped model and the debris thicknesses appear to be significantly smaller in comparison to the sloped model. The focus area reveals the flat model underestimates the debris thickness on the glacier as it has an average value of 0.19 ( $\pm 0.05$ ) m. These debris thicknesses are greater than the linear model, but much lower than the nonlinear sloped model. Table 3.2 reveals that the large difference between the sloped model and the flat model is caused by differences in the net radiation. The flat model only corrects for pixels that are shaded and does not correct for the effects of topography thereby causing the incoming solar radiation to be overestimated in most cases (the exception is for east facing pixels, which are underestimated). The overestimation in incoming solar radiation causes the net radiation to increase, thereby decreasing the modeled debris thickness. This is important because if the flat model

values are used to fill in the undefined pixels in the sloped model, one must understand that the debris thicknesses will be lower. A preferable alternative may be to use the average debris thickness from the sloped model similar to Table 3.2 based on the average slope and aspect of the 30 m pixel. However, resampling the incoming solar radiation to 30 m eliminates almost all of the undefined pixels.

### **3.6.5 Importance of DEM resolution**

The requirement of a high resolution DEM limits the ability to transfer these models to other regions where this data may not be available. The ASTER GDEM was used to assess the importance of the DEM resolution. Figure 3.6D shows the debris thickness map derived using the nonlinear sloped model with the ASTER GDEM. The average debris thickness in the focus area was 0.18 ( $\pm 0.02$ ) m. These debris thicknesses also underestimate the measured debris thicknesses and are very similar to the values derived using the flat model. This underestimation likely occurs because the 30 m resolution of the DEM is too poor to capture local variations in the surface topography of the glacier. Hence, the variations in incoming solar radiation are not captured as well as those using a high resolution DEM. However, the debris thickness map using the ASTER GDEM and the nonlinear sloped model appears to capture the trends associated with the debris thickness better than the flat model, despite the findings in the focus area. The thick debris region behind the calving front in the center of Imja-Lhotse Shar Glacier (Figure 3.6D) more closely resembles the nonlinear sloped model (Figure 3.6A) than the nonlinear flat model (Figure 3.6C). Therefore, while a high-resolution DEM will yield the best results, we recommend the ASTER GDEM should be used instead of a flat model to get an estimate of the debris thickness in an unknown area. However, one must

use caution with these estimates as the analysis here shows the debris thickness are likely to be significantly underestimated.

### **3.6.6 Debris thickness for glaciers in the Everest region**

The ASTER GDEM was used to derive debris thickness maps for the debris-covered glaciers in the Everest region (Figure 3.7). The Ngozumpa and Khumbu glacier have been outlined using the GLIMS database to compare the derived thermal resistances with previous debris thickness measurements (Nakawo et al., 1986; Nicholson and Benn, 2012). The results on the Khumbu glacier show relatively good agreement with the debris thickness map generated by Nakawo et al. (1986). The debris is thicker close to the terminal moraine and thins upglacier. Furthermore, the modeled debris thickness shows the central zones of thin debris with thicker debris towards the lateral moraines, which Nakawo et al. (1986) observed. The debris thickness is slightly underestimated once again likely resulting from the use of the ASTER GDEM as opposed to a high resolution DEM as previously discussed. There are similar trends with respect to debris thickness on Ngozumpa glacier as well, where the terminal moraine has thicker debris and the debris thins upglacier as measured by Nicholson and Benn (2012). Furthermore, Spillway Lake has been growing near the terminal moraine of Ngozumpa glacier and can clearly be seen as the region of low debris thickness amongst the thicker debris in the terminal moraine. Once again, the debris thickness is underestimated compared to Nicholson and Benn (2012) due to the poor resolution of the DEM. Future work should seek to quantify how much the debris thickness is underestimated and develop a method that is able to accurately quantify the debris thickness from a poor resolution DEM. This would require a detailed debris thickness survey such that the resulting debris thickness maps could be properly validated.

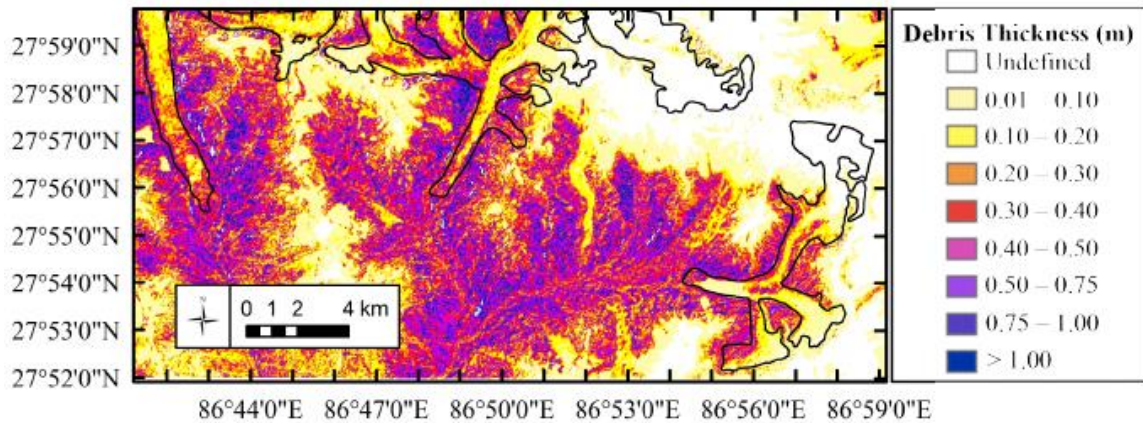


Figure 3.7: Debris thickness (m) using the ASTER GDEM and nonlinear sloped model for debris-covered glaciers in the Everest region with Ngozumpa, Khumbu, and Imja-Lhotse Shar Glaciers, left to right respectively, highlighted with GLIMS outlines.

### 3.6.7 Sensitivity analysis

The model developed in this study relies heavily upon meteorological inputs, measured parameters, and assumed values associated with the debris cover. The meteorological inputs are subject to instrument error and may not be directly transferable from the site of the automatic weather station to the debris-covered glaciers. The particular meteorological parameters of interest are wind speed ( $u$ ), air temperature ( $T_{air}$ ), and incoming solar radiation ( $S_{in}$ ). The parameters associated with the debris cover that may affect results are the surface roughness length ( $z_0$ ), albedo ( $\alpha$ ), and effective thermal conductivity ( $K_{eff}$ ). In addition, there is uncertainty associated with the nonlinear approximation factor ( $G_{ratio}$ ) and the derived surface temperature ( $T_s$ ) from the Landsat7 thermal band. A sensitivity analysis with respect to these parameters was performed on the focus area (Table 3) to identify how each affects the modeled debris thickness ( $d$ ).

Table 3.3: Sensitivity analysis for select meteorological and model parameters.

	$T_s$	$G_{ratio}$	$T_{air}$	$u$	$S_{in}$	$z_0$	$\alpha$	$K_{eff}$	d avg (m)	Change
Baseline	-	2.7	AWS	AWS	AWS	0.016	0.30	0.96	<b>0.29</b>	-
$T_s$	+1	-	-	-	-	-	-	-	0.41	<b>+ 0.12</b>
	-1	-	-	-	-	-	-	-	0.24	- 0.05
$G_{ratio}$	-	+0.4	-	-	-	-	-	-	0.33	+ 0.04
	-	-0.4	-	-	-	-	-	-	0.25	- 0.04
$T_{air}$	-	-	+2	-	-	-	-	-	0.24	- 0.05
	-	-	-2	-	-	-	-	-	0.40	<b>+ 0.11</b>
$u$	-	-	-	+1	-	-	-	-	0.45	<b>+ 0.16</b>
	-	-	-	-1	-	-	-	-	0.21	<b>- 0.08</b>
$S_{in}$	-	-	-	-	+10%	-	-	-	0.21	<b>- 0.08</b>
	-	-	-	-	-10%	-	-	-	0.45	<b>+ 0.16</b>
$z_0$	-	-	-	-	-	0.010	-	-	0.25	- 0.04
	-	-	-	-	-	0.022	-	-	0.39	<b>+ 0.10</b>
$\alpha$	-	-	-	-	-	-	0.20	-	0.20	<b>- 0.09</b>
$k_{eff}$	-	-	-	-	-	-	-	- 0.33	0.39	<b>+ 0.10</b>
	-	-	-	-	-	-	-	+ 0.33	0.19	<b>- 0.10</b>

The sensitivity analysis reveals the model is most sensitive to the wind speed and incoming solar radiation. The assumption that the incoming solar radiation at Pyramid Station is the same as the incoming solar radiation over the study area is a reasonable assumption, since all the images used in this study had completely clear skies over both Pyramid Station and the study area. Therefore, it is unlikely that the incoming solar radiation would be  $\pm 10\%$  different. The model's sensitivity to wind speed is concerning because the automatic weather station is located 10 km away from the glacier. The model assumes the wind is the same on the glacier as it is at the automatic weather station, but no data on this exists. Future work should investigate the relationship between meteorological parameters at Pyramid Station and on the debris-covered glaciers.

The model is moderately sensitive to the surface temperature and air temperature on the glacier. Both these parameters affect the temperature gradient in the sensible heat flux term and hence an increase in the gradient will result in an increase in the sensible heat flux, thereby reducing the net energy flux and increasing the modeled debris thickness. Furthermore, the increased sensitivity to surface temperature is quite interesting when one considers the mixed pixel effect. The mixed pixel effect causes the actual surface temperature to be reduced due to surrounding bare ice faces. This reduction in surface temperature directly reduces the derived debris thickness, but also reduces the temperature gradient in the sensible heat flux term thereby further reducing the debris thickness. The model's sensitivity to the surface temperature shows how much the mixed pixel effect can alter the derived thermal resistances.

With respect to parameters associated with the debris cover, the model is very sensitive to the value of effective thermal conductivity. Therefore, it is important that the effective thermal conductivity is measured at multiple sites for various debris thicknesses throughout the debris-covered glacier such that the modeled debris thickness maps are accurate. In the event that there is large uncertainty in the effective thermal conductivity, the model can be solved for thermal resistance instead. The assumption of a constant albedo over the debris-covered glacier is another limitation of this model, especially since the model is sensitive to albedo. Methods exist to use other Landsat7 bands to estimate albedo (Liang, 2001); however, the authors had no way of validating these results. Therefore, the average value of albedo of 0.30 determined by a previous study on Ngozumpa glacier (Nicholson and Benn, 2012) was used in this study. Future work should seek to derive the albedo from satellite imagery in conjunction with field measurements to validate these results. Lastly, the model was least sensitive to changes in  $G_{ratio}$  lending confidence to its use in this study.

### **3.7 CONCLUSION**

The model described in this study allows the debris cover or thermal resistance on debris-covered glaciers to be derived from Landsat7 satellite imagery in conjunction with meteorological data from an automatic weather station nearby. The model was applied to glaciers in the Everest region and the resulting debris thicknesses were compared to field measurements. The model accounts for the nonlinear temperature gradient in the debris through the use of a nonlinear approximation factor, which yields reasonable results. Furthermore, the use of a high resolution DEM greatly improves the results of the modeled debris thicknesses. In the event that a high resolution DEM is not available, the authors recommend using a lower resolution global DEM to estimate debris thicknesses as opposed to using a flat model. It is important to use caution with these results if a lower resolution DEM is used since the derived debris thicknesses are likely to be underestimated. A sensitivity analysis reveals that the model is most sensitive to wind speed and incoming shortwave radiation. With respect to debris cover parameters, the model is very sensitive to albedo and the effective thermal conductivity. In the event that the thermal conductivity is uncertain, the thermal resistances may be derived instead. Future work should explore how the meteorological conditions vary spatially and seek to derive the albedo from satellite imagery. The main limitation of this work is the poor resolution of the Landsat7 thermal band. The derived debris thickness must be resampled to the resolution of the thermal band before they are used in melt models or other applications.

### **3.8 ACKNOWLEDGEMENTS**

The authors acknowledge the support of the USAID Climate Change Resilient Development (CCRD) project for the support of Rounce. The meteorological data from Pyramid Station used in this study was collected within the SHARE Project thanks to

contributions from the Italian National Research Council and the Italian Ministry of Foreign Affairs. We also acknowledge the support of Dr. Dhananjay Regmi of Himalayan Research Expeditions for logistical support during fieldwork and Dr. Damodar Lamsal for providing us with a digital elevation model of the Imja Glacial Lake and glacier area. The comments of Professor Douglas I. Benn and Lindsey Nicholson are greatly appreciated.

## **Chapter 4: Debris-covered glacier energy balance model for Imja-Lhotse Shar Glacier in the Everest region of Nepal**

David Rounce, Daene McKinney, and Duncan Quincey

Published in *The Cryosphere* 9:2295-2310, doi:10.5194/tc-9-2295-2015, 2015

### **4.1 ABSTRACT**

Debris thickness plays an important role in regulating ablation rates on debris-covered glaciers as well as controlling the likely size and location of supraglacial lakes. Despite its importance, lack of knowledge about debris properties and associated energy fluxes prevents the robust inclusion of the effects of a debris layer into most glacier surface energy balance models. This study combines fieldwork with a debris-covered glacier energy balance model to estimate debris temperatures and ablation rates on Imja-Lhotse Shar Glacier located in the Everest region of Nepal. The debris properties that significantly influence the energy balance model are the thermal conductivity, albedo, and surface roughness. Fieldwork was conducted to measure thermal conductivity and a method was developed using Structure from Motion to estimate surface roughness. Debris temperatures measured during the 2014 melt season were used to calibrate and validate a debris-covered glacier energy balance model by optimizing the albedo, thermal conductivity, and surface roughness at 10 debris-covered sites. Furthermore, three methods for estimating the latent heat flux were investigated. Model calibration and validation found the three methods had similar performance; however, comparison of modeled and measured ablation rates revealed that assuming the latent heat flux is zero may overestimate ablation. Results also suggest that where debris moisture is unknown, measurements of the relative humidity or precipitation may be used to estimate wet debris periods, i.e., when the latent heat flux is non-zero. The effect of temporal

resolution on the model was also assessed and results showed that both 6-hour data and daily average data slightly underestimate debris temperatures and ablation rates, thus these should only be used to estimate rough ablation rates when no other data are available.

## **4.2 INTRODUCTION**

Debris-covered glaciers are commonly found in the Everest region of Nepal and have important implications with regard to glacier melt and the development of glacial lakes. It is well understood that a thick layer of debris (i.e. > several cm) insulates the underlying ice, while a thin layer of debris (i.e. < several cm) may enhance ablation (Østrem, 1959; Nakawo and Young, 1981; Nicholson and Benn, 2006; Reid et al., 2012). Spatial variations in debris thickness, particularly where the debris layer thins up-glacier, can also lead to reverse topographic and ablation gradients, glacier stagnation and, ultimately, the development of lakes (Benn et al., 2012). These glacial lakes and their surrounding bare ice faces also play a crucial role in glacier melt as they typically have ablation rates that are orders of magnitude greater than those observed beneath debris cover (Benn et al., 2012). The importance of debris thickness has led many studies to develop models in conjunction with knowledge of the surface temperature to derive debris thickness (Zhang et al., 2011; Foster et al., 2012; Fujita and Sakai, 2014; Rounce and McKinney, 2014). With knowledge of debris thickness, energy balance models may be used to model debris surface temperature, sub-debris ablation rate, and/or runoff downstream (Nicholson and Benn, 2006; Reid et al., 2012; Collier et al., 2014; Fujita and Sakai, 2014). The main factors affecting the performance of these models are the amount of knowledge of the debris properties, the spatial and temporal resolution of the meteorological data, and the assumptions/complexity of the model.

The properties of the debris typically required in debris-covered glacier energy balance models are the albedo, thermal conductivity, and surface roughness. The albedo of debris on glaciers in the Everest region has been found to range from 0.1 – 0.6 (Inoue and Yoshida, 1980; Kayastha et al., 2000; Nicholson and Benn, 2012; LeJeune et al., 2013). Specifically, Nicholson and Benn (2012) reported that 62% of measured values ranged between 0.1 and 0.3. Similarly, Kayastha et al. (2000) showed that most values fall between 0.2 and 0.4. The thermal conductivity of debris in the Everest region has been found to range from 0.60 to 1.29 W m<sup>-1</sup> K<sup>-1</sup> (Conway and Rasmussen, 2000; Nicholson and Benn, 2012; Rounce and McKinney, 2014). The surface roughness,  $z_0$ , is arguably the most difficult parameter to measure as it requires an eddy covariance instrument, horizontal wind speed measurements at multiple heights above the surface, or detailed microtopographic measurements (Brock et al., 2006). In the Everest region, Inoue and Yoshida (1980) estimated  $z_0$  to be 0.0035 m and 0.060 m for two sites, one consisting of small schist and bare ice and another comprising mainly large granite, respectively. Takeuchi et al. (2000) estimated a similar value of  $z_0$  on the Khumbu glacier of 0.0063 m. On Miage glacier in the Italian Alps, Brock et al. (2010) measured  $z_0$  to be 0.016 m on a debris-covered glacier.

In addition to the properties of the debris, the amount and source of meteorological data available may also greatly influence the model performance. In particular, knowledge related to the latent heat flux on debris-covered glaciers is very limited. This has led previous studies to assume the surface is dry (Foster et al., 2012; Lejeune et al., 2013; Rounce and McKinney, 2014), assume it is dry unless the surface relative humidity was 100% (Reid and Brock 2010; Reid et al., 2012; Fyffe et al., 2014), assume a relationship between debris thickness and wetness (Fujita and Sakai, 2014), or use a reservoir approach to model the moisture in the debris (Collier et al., 2014). Collier

et al. (2014) suggested that if the atmospheric surface layer is well mixed, then the water vapor partial pressure between the surface and the air may be assumed to be constant, thereby resulting in a latent heat flux based on the vapor pressure gradient. Fyffe et al. (2014) also commented that the lower portion of the debris near the ice interface was observed to be saturated indicating that there may be evaporation and condensation occurring within the debris, albeit small, even when the surface relative humidity is less than 100%. The lack of knowledge of the moisture in the debris and at its surface makes it difficult to accurately model the latent heat flux term. These problems are further exacerbated in data scarce regions where automatic weather stations are not available. In these situations, reanalysis datasets must be used for all the required meteorological data (Fujita and Sakai, 2014).

This study develops a method to estimate  $z_0$  using a microtopographic method in conjunction with Structure from Motion (SfM) photogrammetry techniques (Westoby et al., 2012). The  $z_0$  values are used with measured values of thermal conductivity, and previously reported values of albedo to calibrate a debris-covered glacier energy balance model on Imja-Lhotse Shar Glacier. Temperature sensors installed at various depths at debris-covered sites were operated from May to November 2014 on Imja-Lhotse Shar Glacier and are used for calibration and validation of the model. Various methods for estimating the latent heat flux are investigated. Furthermore, sub-debris ablation rates are compared to ablation stake measurements to assess model performance and the effects of temporal resolution are investigated.

## **4.3 DATA**

### **4.3.1 Field data**

Field research was conducted on the debris-covered portion of Imja-Lhotse Shar Glacier (27.901°N, 86.938°E, ~5050 m a.s.l., Figure 4.1) from May to November 2014. Imja-Lhotse Shar Glacier refers to both Imja glacier and Lhotse Shar Glacier, which are avalanche-fed debris-covered glaciers that converge and terminate into Imja Lake. The debris primarily consists of sandy boulder gravel (Hambrey et al., 2008) with the debris thickness increasing towards the terminal moraine. A more detailed description of the glacier may be found in Rounce and McKinney (2014). The field expedition focused on 19 sites on the debris-covered portion of the glacier to determine how debris thickness and topography affect ablation rates. Four sites were used to analyze the surface roughness through the use of SfM and are referred to as Sites A-D (Figure 4.2). These sites were selected to represent various grain sizes and mixes of debris that were observed on Imja-Lhotse Shar Glacier. Site A was relatively homogenous with the majority of debris being cobble and gravel ranging in size from 0.05 to 0.25 m. Site B comprised similar cobbles typically ranging in size from 0.15 to 0.25 m with larger boulders lying on top of the cobble of up to 1.0 m. Site C had the finest debris, which primarily consisted of fines and gravel with some cobbles on the surface up to 0.15 m in size. Lastly, Site D was the most heterogeneous site with boulders ranging up to 0.40 m overlying a surface of cobble of similar size to Site A mixed with the fine and gravel material found in Site C.

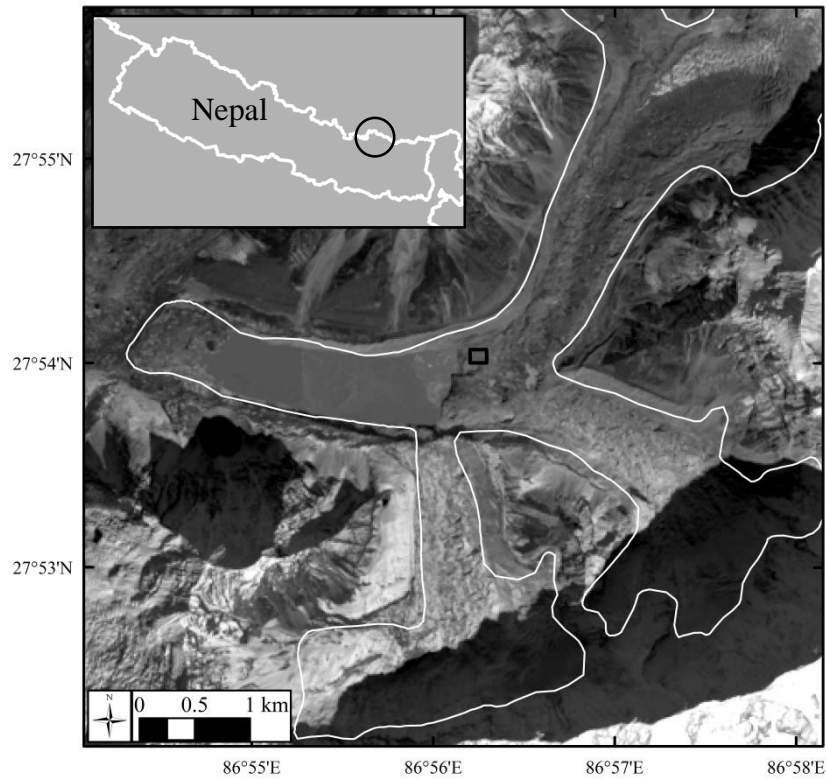


Figure 4.1: Landsat 8 panchromatic image from 14 Nov 2014 of Imja-Lhotse Shar Glacier with the focus area of this study highlighted by the rectangular box several kilometers up-glacier from the terminus, and the site location within Nepal shown in the inset.

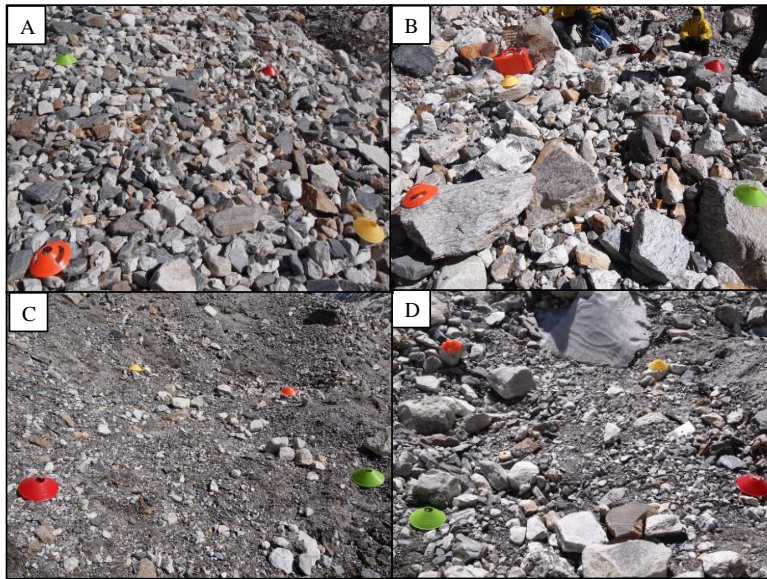


Figure 4.2: Sites A-D highlighting the variations in grain sizes that are found over the debris-covered portion of Imja-Lhotse Shar Glacier (cones 0.19 m diameter).

Temperature sensors and ablation stakes were installed at 20 other sites; however, data could only be retrieved from 15 of the sites (Table 4.1) as sensors were lost due to large changes in the topography and some of the loggers failed. Sites 4-14 were located in a single area that appeared to have developed from differential backwasting over the years. This was the same focus area as described in Rounce and McKinney (2014) and was selected because it appeared to be representative of the debris-covered terrain on Imja-Lhotse Shar Glacier and was accessible. Sites 15-20 were located outside of the focus area in an adjacent melt basin to determine if the focus area was representative of other debris-covered areas. At each site, the debris thickness was determined following the methods described in Rounce and McKinney (2014) with the exception of Site 4, where the debris thickness was greater than 1.0 m and therefore was estimated assuming a linear temperature profile from the mean temperatures over the study period similar to

the extrapolation used in Nicholson and Benn (2012). The debris thickness of these sites ranged from 0.07 m to greater than 1.0 m. A debris thickness of 1.0 m was considered the maximum due to labor constraints. The slope was also approximated by measuring two points, one 0.5 m uphill from the site and the other 0.5 m downhill, using a total station (Sokkia SET520,  $\pm 2.6\text{mm}/100\text{m}$ ). The slope at each site ranged from  $17^\circ$  to  $37^\circ$ . The aspect of each site was measured using a compass (Table 4.1).

Table 4.1: Details of the debris thickness, topography, and monitoring equipment installed at each site. *Italics* note an estimation of debris thickness.  $T_s$  denotes surface temperature.

Site	Debris Thickness (m)	Slope ( $^\circ$ )	Aspect ( $^\circ$ )	Temperature Sensor Depth (m)	Ablation Stake	$z_0$ photos
4	<i>1.50</i>	17	232	$T_s, 0.10, 0.20, 0.40, 0.83$	-	-
5	0.54	24	158	$T_s$	x	-
6	0.08	37	237	$T_s$	x	-
7	0.52	31	65	-	x	-
8	0.20	32	187	-	x	-
10	0.07	32	337	-	x	-
11	0.45	32	197	$T_s, 0.05, 0.10, 0.20, 0.36$	x	-
12	0.15	19	265	-	x	-
13	0.33	29	295	$T_s, 0.05, 0.10, 0.20$	x	-
14	0.26	23	148	$T_s, 0.05, 0.24$	x	-
15	0.37	29	40	$T_s$	x	-
16	0.15	32	264	-	x	-
17	0.27	29	228	$T_s$	x	-
19	0.37	33	198	$T_s$	x	-
20	0.20	29	200	$T_s$	x	-
A	-	-	-	-	-	x
B	-	-	-	-	-	x
C	-	-	-	-	-	x
D	-	-	-	-	-	x

Temperature sensors (TR-42 ThermoRecorder, T&D Corporation) were installed and successfully retrieved at 10 sites. These sensors recorded data every half hour from 19 May to 09 November 2014. Each of the 10 sites had a sensor at its surface, which was considered to be installed 1 cm into the debris since debris was placed on top of the sensor. Sites 4, 11, 13, and 14 also had temperature sensors installed within the debris to capture the nonlinear temperature variations in the debris and at three of the four sites the sensors were retrieved such that the thermal conductivity could be estimated (Conway and Rasmussen, 2000).

Ablation stakes were also installed at 14 sites. One site had a debris thickness greater than 1.0 m, so an ablation stake could not be installed. The ablation stakes were installed by excavating to the debris-ice interface, at which point the debris thickness was measured, and then a 2 inch diameter hole was drilled vertically approximately 1.0 m into the ice using a manual ice drill (Kovacs Enterprise). A 2.0 m piece of 1 ½ inch PVC pipe was placed into the hole and the height from the top of the ice to the top of the pipe was measured to determine the exact length that the PVC pipe was inserted into the ice. A PVC end cap was then placed on top of the pole to prevent anything from entering the hole through the pipe. The debris was then replaced in its approximate original position.

#### **4.3.2 Meteorological data**

The meteorological data used in the model calibration and validation was from an automatic weather station (AWS), Pyramid Station (27.959° N, 86.813° E, 5035 m a.s.l., SHARE Network operated by EV-K<sup>2</sup>-CNR), located off-glacier, next to the Khumbu glacier, approximately 14 km northwest of Imja-Lhotse Shar Glacier. The meteorological data provided by Pyramid Station were unvalidated, i.e., prior to their

quality control processing, minute measurements of air temperature, wind speed, relative humidity, global radiation, precipitation, and snow depth. The data were processed to be consistent with the half-hour debris temperature measurements on Imja-Lhotse Shar Glacier. The air temperature, wind speed, relative humidity, and global radiation data were reviewed and deemed plausible, so no adjustments were performed. The half-hour precipitation data was determined by summing the precipitation over each half-hour time step. A few of the minute measurements recorded negative precipitation, which were assumed to be zero as negative precipitation is not feasible. The half-hour snow depth data was processed to assume a snow depth of zero if snow was not recorded on the ground for the entire half-hour. The average snow depth over the half-hour was then computed and any average snow depth less than 0.001 m was considered to be zero. Wind speed data were collected at 5 m and adjusted to 2 m to be consistent with air temperature measurements for the turbulent heat fluxes assuming a logarithmic dependence (Fujita and Sakai, 2014). The snow depth data were used to derive a snowfall rate assuming a density of snow of  $150 \text{ kg m}^{-3}$ . The data were available from 31 May to 12 October 2014 with a few short gaps (missing 11.9% data). The first two days of meteorological data were used as start-up time for the model.

Longwave radiation was not measured at Pyramid Station during this period; therefore, the downward longwave radiation flux from NCEP/NCAR reanalysis data (Kalnay et al., 1996) was used with a minor modification. A comparison of the downward longwave radiation flux from NCEP/NCAR and the incoming longwave radiation flux at Pyramid Station from 2003 to 2010 (neglecting any data gaps) between the months of June and September revealed that NCEP/NCAR overestimated the incoming longwave radiation by an average of  $29 \text{ W m}^{-2}$  (results not shown). Therefore, the NCEP/NCAR downward longwave radiation flux was adjusted to account for this

overestimation when being used in conjunction with the Pyramid Station data. This reanalysis dataset provides 6-hour meteorological data and was resampled using a linear interpolation such that the temporal resolution of the incoming longwave radiation agreed with the half-hour debris temperature measurements.

Ablation rates were modeled over the same time period as the ablation stakes (18 May to 09 November). For days where no meteorological data was available, i.e., the data gaps, the ablation for that day was assumed to be equal to the daily ablation rate for that specific month. As the available meteorological data began on 31 May, the daily ablation rate for the month of May was assumed to be equal to the daily ablation rate of the first week of June. Temperature sensors revealed the debris was snow covered from 26 May to 01 June, so the melting during these days was assumed to be zero. Temperature profiles also show the debris was snow covered from 13-20 October and deeper thermistors revealed the temperature remained around freezing until the sensors were removed in November. Therefore, the melt rates after the 12 October were assumed to be zero.

## **4.4 METHODS**

### **4.4.1 Surface roughness ( $z_0$ )**

Structure from Motion (SfM) was used to derive fine-resolution (i.e. centimetric) digital elevation models (DEMs) at four sites (Sites A-D) located on the debris-cover of Imja-Lhotse Shar Glacier (Figure 4.2). In brief, SfM relies upon the acquisition of a series of overlapping images that capture the features of the terrain from a number of different vantage points. Computer vision techniques detect matching features between images using multiscale image brightness and colour gradients and a highly iterative bundle adjustment procedure is used to develop a three-dimensional structure of the

surface (Snavely et al., 2008). Camera positions and orientations are solved simultaneously with surface geometry utilizing the high level of redundancy afforded by a large overlapping image set. Ground control points (GCPs), collected using a total station with an error less than 0.4 mm, are then used to transform the relative three-dimensional surface into an absolute coordinate system. The resulting point-cloud data are comparable in both density and accuracy to those generated by terrestrial laser scanning (Westoby et al., 2012) and can either be used as-is, or decimated (as in this study) to generate gridded elevation data. The use of SfM within geoscience is well reviewed by Westoby et al. (2012) and specific details of the mathematical operations involved can be found in Snavely (2008) and Szeliski (2011). Here, we therefore focus mostly on our field method and subsequent roughness analysis.

At each of our sites ~40 photos were taken around a roughly 2 m x 2 m grid. Cones were placed in the four corners of the grid as GCPs and their location was measured using a total station with a local coordinate system. The GCPs and photos were processed using Agisoft PhotoScan Professional Edition Version 1.1.0 to create a DEM for each site. At each stage, the highest accuracy settings were chosen. No *a-priori* information about camera position or orientation was recorded, so these were estimated coincidentally as part of the adjustment. In each case the initial estimates of camera position and altitude were accepted and used to generate a sparse point cloud ( $10^3 - 10^4$  points). A moderate depth filter was then used to derive a dense cloud ( $10^6 - 10^7$  points), and subsequently a mesh was constructed using the height field as the surface type. The error of the DEM was computed as the root mean square error based on the differences between the measured GCPs from the total station and the modeled position of the GCPs from the software. The resulting DEMs were then resampled in ArcGIS 10.3 to a resolution of 0.01 m and were clipped to remove the cones from the subsequent analyses.

The DEM was then fit with an x-y plane using a method of least squares such that the DEM was flattened with a mean elevation of zero.

These processed DEMs of the four sites were analyzed to determine the surface roughness,  $z_0$ . Lettau (1969) developed an empirical relationship to estimate  $z_0$ :

$$z_0 = 0.5h^* \frac{s}{S} \quad (4.1)$$

where  $h^*$  is the average vertical extent or effective obstacle height,  $s$  is the silhouette area or area of the upwind face of an average element, and  $S$  is the specific area or unit ground area occupied by each obstacle. Previous studies have estimated the variables in Equation 1 through a simplified standard deviation approach (which will be referred to as the Lettau-Munro method), based on the variations in elevations and the number of continuous positive groups above the mean elevation (Munro, 1989; Rees and Arnold, 2006; Brock et al., 2006). Initially, the Lettau-Munro method was applied to measure  $z_0$  for every row and column transect of the four DEMs; however, the resulting values of  $z_0$  did not capture the variations between sites and may have been slightly underestimated (see results).

Consequently, an alternative method was developed to estimate the effective height, silhouette area, and unit ground area of each obstacle using a similar transect approach and taking advantage of the high resolution DEM. One problem with applying the method from Lettau (1969) is the lack of a clear definition of what constitutes an obstacle. The surface roughness will greatly vary depending on what is considered to be an obstacle, so a method must be developed that (i) objectively determines the obstacle height and (ii) yields reasonable estimates of surface roughness regardless of the resolution of the DEM. Smith (2014) states that the relationship developed by Lettau

(1969) holds at low roughness densities (< 20-30% of the surface area), beyond which the observed  $z_0$  is less than that predicted by Lettau (1969) because the obstacles begin to aerodynamically interfere with one another. Therefore, a method was developed to select an obstacle height based on an obstacle density of 30%.

Initially, all the relative topographic highs and lows were identified. This was done for all of the transects in each of the four cardinal directions with respect to the DEM, i.e., every East-West, North-South, West-East, and South-North transect. Every elevation change between a relative low and high was considered a potential obstacle. The depth of each obstacle was defined as the distance between two low points surrounding the obstacle's high point. In the event that an obstacle was identified, but there was no low point following the high point, i.e., the low point was outside the extent of the transect, then the depth of the obstacle could not be determined. Figure 4.3 shows an example of a transect from Site B, which identifies the obstacle's height and depth based on the method developed in this study. The obstacle density was then defined as the cumulative depth of all the obstacles above the obstacle threshold divided by the length of the transect. An iterative approach was then used to determine the obstacle height that causes the obstacle density to reach the 30% threshold.

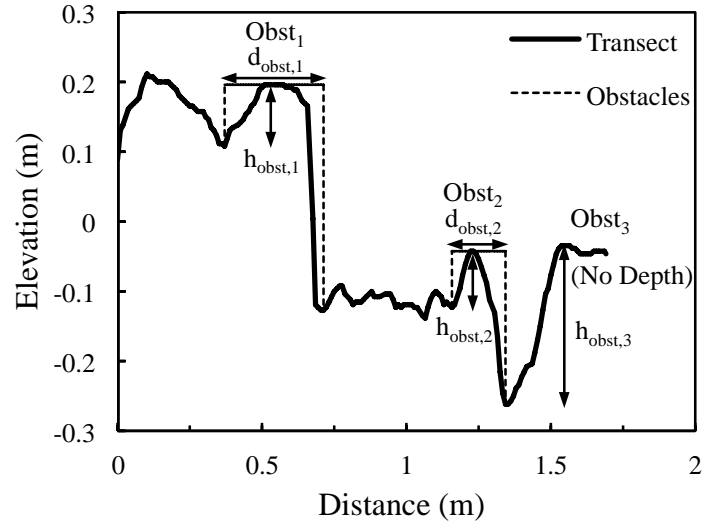


Figure 4.3: Transect from Left-Right of Site B showing the identification of obstacles (Obst) and their corresponding heights ( $h_{obst}$ ) and depths ( $d_{obst}$ ).

Once the obstacle height has been determined, the silhouette area and unit ground area were approximated from the height and depth of the obstacles. Specifically, the silhouette area was taken to be the height of the obstacle times a unit width and the unit ground area was estimated as the depth of the obstacle times a unit width. Based on these definitions, Equation 4.1 may be simplified to (Eqn 4.2):

$$z_0 = 0.5 \frac{h^{*2}}{d_{obst}^*} \quad (4.2)$$

where  $d_{obst}^*$  is the average depth of the obstacle. The surface roughness,  $z_0$ , was computed using the average effective obstacle height and average obstacle depth for each transect. In the event that an obstacle was identified, but did not have a depth, the obstacle's height was still used in the average.

#### 4.4.2 Debris-covered glacier energy balance model

The model used in this study was a steady-state surface energy balance model for a debris-covered glacier, where:

$$R_n(T_s) + H(T_s) + LE(T_s) + P(T_s) + Q_c(T_s) = 0 \quad (4.3)$$

where  $R_n$  is the net radiation flux,  $H$  is the sensible heat flux,  $LE$  is the latent heat flux,  $P$  is the heat flux supplied by rain, and  $Q_c$  is the ground heat flux (all in  $\text{W m}^{-2}$ ). The net radiation and sensible heat fluxes are fully described in Rounce and McKinney (2014); however, in the current study the incoming shortwave radiation was only corrected for the effects of topography as shading could not be considered due to the lack of a high resolution DEM of the glacier.

The latent heat flux is difficult to determine without detailed knowledge of the moisture in the debris or the relative humidity at the surface. As the surface relative humidity was unknown, this study has analyzed three methods for estimating the latent heat flux: (1) assuming the debris is dry ( $LE = 0$ ), (2) assuming it is dry unless the relative humidity is 100%, at which point the surface relative humidity is assumed to also be 100% based on the assumption that the water vapor above the surface is well mixed, and (3) assuming the surface is saturated when it is raining. These methods for modeling the latent heat flux will be referred to herein as  $LE_{Dry}$ ,  $LE_{RH100}$ , and  $LE_{Rain}$ , respectively. The reservoir-approach detailed by Collier et al. (2014) and the empirical relationship between debris thickness and wetness (Fujita and Sakai, 2014) were not applied to this study due to the limited amount of knowledge of moisture within the debris and how the debris properties change with respect to depth. The latent heat flux is thus estimated according to Nicholson and Benn (2006):

$$LE = \left( \frac{0.622 \rho_{air}}{P_0} \right) L_e A u (e_z - e_s) \quad (4.4)$$

where

$$A = \frac{k_{vk}^2}{\ln\left(\frac{z}{z_0}\right)\ln\left(\frac{z}{z_0}\right)} \quad (4.5)$$

where  $\rho_{air}$  is the density of air at standard sea-level pressure ( $1.29 \text{ kg m}^{-3}$ ),  $P_0$  is the standard air pressure at sea level ( $1.013 \times 10^5 \text{ Pa}$ ),  $L_e$  is the latent heat of evaporation of water ( $2.49 \times 10^6 \text{ J kg}^{-1}$ ),  $A$  is a dimensionless transfer coefficient,  $u$  is the wind speed collected at a height of 2 m ( $\text{m s}^{-1}$ ),  $e_z$  and  $e_s$  are the vapor pressures (Pa) at height  $z$ , 2 m, and on the surface of the debris, respectively,  $k_{vk}$  is von Karman's constant (0.41), and  $z_0$  is the surface roughness.

The heat flux due to precipitation was estimated following Reid and Brock (2010):

$$P = \rho_w c_w w (T_r - T_s) \quad (4.6)$$

where  $\rho_w$  is the density of water ( $999.97 \text{ kg m}^{-3}$ ),  $c_w$  is the specific heat capacity of water ( $4.18 \times 10^3 \text{ J kg}^{-1} \text{ K}^{-1}$ ),  $w$  is the rainfall rate ( $\text{m s}^{-1}$ ), and  $T_r$  is the temperature of rain (K), which was assumed to be equal to the air temperature.

The debris layer was broken down into layers of 0.01 m such that the nonlinear temperature profiles in the debris could be captured using a Crank-Nicholson Scheme (Reid and Brock, 2010). The conductive heat flux at the surface and at the debris/ice interface were estimated following Reid and Brock (2010):

$$Q_{c,s} = k_{eff} \frac{T_d(1) - T_s}{h} \quad (4.7)$$

$$Q_{c,ice} = k_{eff} \frac{T_d(N-1) - T_{ice}}{h} \quad (4.8)$$

where  $k_{eff}$  is the effective thermal conductivity ( $\text{W m}^{-1} \text{K}^{-1}$ ),  $h$  is the height of each layer in the debris set at 0.01 m, and  $T_d(1)$ ,  $T_d(N-1)$ ,  $T_{ice}$  are the temperatures (K) of the first layer in the debris, the last layer before the debris/ice interface, and the temperature of the ice (273.15 K), respectively.

The surface temperature was computed at half-hour time steps using an iterative Newton-Raphson method approach as detailed in Reid and Brock (2010). In the event of snow, a simple snowmelt model was used (Fujita and Sakai, 2014), which applies an energy balance over the snow surface that includes net radiation, turbulent heat fluxes, and conductive heat flux with the debris layer in addition to a variable surface albedo of the snow based on the number of days since fresh snow and the air temperature. The thermal conductivity of snow was assumed to be  $0.10 \text{ W m}^{-1} \text{K}^{-1}$  (Sturm et al., 1997; Sturm et al., 2002; Rahimi and Konrad, 2012) and the surface roughness of the snow was assumed to be 0.002 m (Brock et al., 2006). If snow was on the surface, all the heat fluxes at the debris surface were assumed to be zero with the exception of the conductive heat flux in the debris and at the debris/snow interface. If all the snow was melted on the surface, then the next time step returned to the snow-free energy balance model.

As detailed knowledge of albedo, thermal conductivity, and surface roughness was not available for the sites where temperature sensors were installed, the debris-covered glacier energy balance model was calibrated at each site from 02 June to 30 July 2014. The calibration was performed by minimizing the total sum of squares of the measured versus modeled surface temperature for each site and was done independently for the three methods used to estimate the latent heat flux. Bounds for the thermal

conductivity and surface roughness were based on measured field data (see results), while the bounds for the albedo were 0.1 – 0.4 (Inoue and Yoshida, 1980; Kayastha et al., 2000; Nicholson and Benn, 2012; LeJeune et al., 2013). A validation was then conducted at each site using data from 08 August to 12 October 2014 to assess how well the calibrated model performed.

## **4.5 FIELD RESULTS**

### **4.5.1 Thermal conductivity ( $k$ )**

The thermal conductivity,  $k$ , of the debris was computed using the temperature measurements from Sites 4, 11, and 13 over the time period of the study (02 June – 12 October 2014) following the methods of Conway and Rasmussen (2000). The calculations used standard values for the density of rock ( $2700 \text{ kg m}^{-3}$ ), volumetric heat capacity of rock ( $750 \text{ J kg}^{-1} \text{ K}^{-1} \pm 10\%$ ), and effective porosity (0.33) based on Nicholson and Benn (2012). Depending on the vertical spacing of temperature sensors at a site,  $k$  was computed at depths of 0.05, 0.10, and 0.20 m. The values of thermal conductivity ranged from 0.42 ( $\pm 0.04$ ) to 2.28 ( $\pm 0.23$ )  $\text{W m}^{-1} \text{ K}^{-1}$ . The average value of  $k$  for each site was 1.44 ( $\pm 0.14$ ), 1.62 ( $\pm 0.16$ ), and 0.47 ( $\pm 0.04$ )  $\text{W m}^{-1} \text{ K}^{-1}$  for Sites 4, 11, and 13, respectively.

These values agree well with other studies in the Everest region that have found the thermal conductivity to vary between 0.60 to 1.29  $\text{W m}^{-1} \text{ K}^{-1}$  (Conway and Rasmussen, 2000; Nicholson and Benn, 2012; Rounce and McKinney, 2014). In September 2013, Rounce and McKinney (2014) found the thermal conductivity to be greatly influenced by depth; however, this trend was not apparent in our current data. We believe this disparity can be explained by the time period during which the data were collected. It is likely that the temporally-limited data (13-24 Sept 2013) presented in

Rounce and McKinney (2014) represent a constantly dry surface, whereas here we observed an entire melt season, where the surface is exposed to precipitation and snow. The thermal conductivities appeared to have a trend over the monsoon season where the highest thermal conductivities were typically observed in July and August, which coincided with higher average air temperature and increased precipitation compared to the other months. As  $k_{eff}$  is one of the parameters that is used to calibrate the model, the range of average thermal conductivity ( $0.47 - 1.62 \text{ W m}^{-1} \text{ K}^{-1}$ ) will be used to bound  $k_{eff}$ .

#### **4.5.2 Surface roughness ( $z_0$ )**

The DEMs generated using the SfM workflow had a total root mean square error of  $0.008 - 0.024 \text{ m}$ . Table 4.2 shows that the errors in elevation (i.e.,  $z$ ) were smaller than in planform (i.e.,  $x$  and  $y$ ) with a maximum error of  $0.007 \text{ m}$ . The contrast between elevation and planimetric errors is likely a result of the identification of the GCPs in each photo during the SfM workflow, since it was easier to identify the top of the cone in each photo than it was to determine the exact point on the rim of the cone. As the error with the total station is small (maximum of  $0.4 \text{ mm}$ ), this human error likely dominated the total error, although errors in estimates of both camera position and orientation will also have contributed. The DEMs were resampled to a resolution of  $0.01 \text{ m}$  such that their resolution was on the same order as their respective errors (3 of the 4 sites had a total RMSE less than  $0.01 \text{ m}$ ). The DEMs were then de-trended to account for variations in the local topography.

Table 4.2: Errors associated with the DEM for each site.

Site	DEM Error (m)			Total
	$x$	$y$	$z$	
A	0.015	0.018	0.007	0.024
B	0.004	0.007	0.001	0.008
C	0.010	0.007	0.002	0.012
D	0.006	0.007	0.001	0.009

Initially,  $z_0$  was estimated from Equation 4.1 using the Lettau-Munro method. The average value of  $z_0$  was 0.0037, 0.0091, 0.0022, and 0.0033 m for Sites A, B, C, and D, respectively. These values are towards the lower end of those previously reported in literature, which were estimated from wind speed profiles and range from 0.0035 to 0.060 m (Inoue and Yoshida, 1980; Takeuchi et al., 2000; Brock et al., 2010). In particular, the average value of  $z_0$  for Sites A, C, and D was comparable or smaller to Area IV on the Khumbu glacier (Inoue and Yoshida, 1980), which comprised small schist with bare ice. Sites A, C, and D were all debris-covered with boulders ranging up to 0.40 m, so these small estimations of  $z_0$  are concerning. Site B also appears to be underestimated as it has similar debris characteristics to Area III on the Khumbu glacier (Inoue and Yoshida), yet its average value of  $z_0$  was much smaller (0.0091 m compared to 0.060 m, respectively). These apparent underestimations of  $z_0$  led to the development of an alternative method.

The alternative method relies upon the selection of the obstacle height (or threshold) such that the obstacle density is 30% (Smith, 2014). Figure 4.4 shows that as the obstacle threshold is increased, the obstacle density decreases, which makes intuitive sense as there will be fewer obstacles in the transect. Table 4.3 shows the values of  $z_0$

using an obstacle density of 30% and the highest resolution DEM (0.01 m) were 0.016, 0.043, 0.006, and 0.014 m for Sites A-D, respectively. These values agree well with the range of  $z_0$  values previously reported (Inoue and Yoshida, 1980; Takeuchi et al., 2000; Brock et al., 2010). Furthermore, these  $z_0$  values appear to capture the inter-site variability as Site B had the highest value of  $z_0$  (0.043 m), which is expected since the debris cover includes large boulders up to 1 m in size (Figure 4.2). Site C, which comprised the smallest grain sizes of the four sites in this study had the lowest estimation of  $z_0$  (0.006 m). Sites A and D had similar values of surface roughness and the standard deviations of Site A and D (0.008 m and 0.012 m, respectively) appear to capture the more homogenous surface of Site A compared to the highly heterogeneous surface of Site D (Figure 4.2).

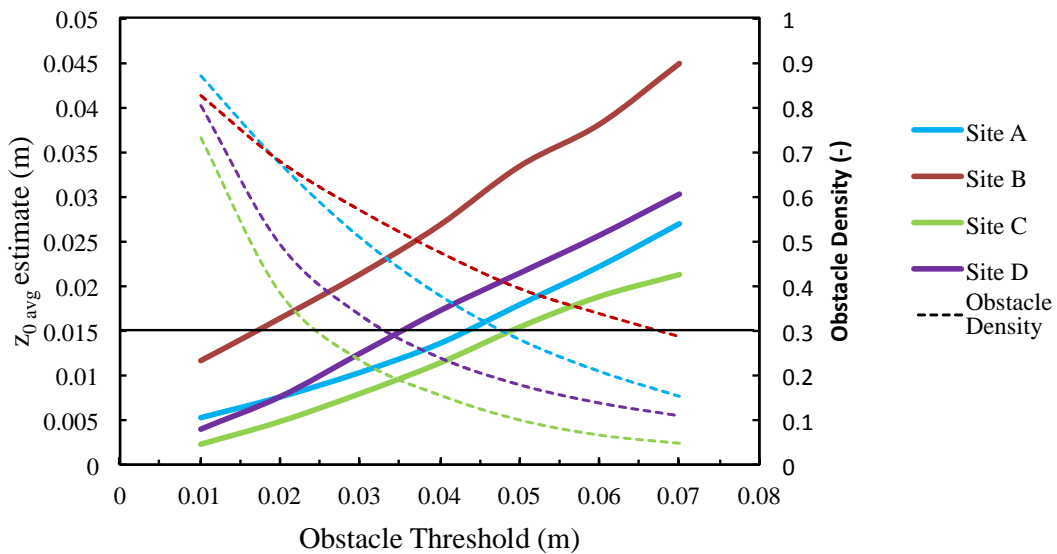


Figure 4.4: The effect of obstacle threshold (m) on both obstacle density and the estimate of surface roughness using the modified method for Sites A-D and the DEMs with a resolution of 0.01 m.

Table 4.3: Surface roughness ( $z_0$ ) estimates and obstacle thresholds as a function of DEM resolution (m) at Sites A-D.

Site	DEM	Obstacle	$z_0$ (m)	
	Resolution (m)	Threshold (m)	avg	std
A	0.01	0.048	0.016	0.008
	0.02	0.052	0.016	0.007
	0.04	0.054	0.015	0.007
B	0.01	0.067	0.043	0.037
	0.02	0.073	0.040	0.029
	0.04	0.078	0.036	0.022
C	0.01	0.024	0.006	0.005
	0.02	0.026	0.006	0.004
	0.04	0.027	0.006	0.006
D	0.01	0.033	0.014	0.012
	0.02	0.037	0.015	0.013
	0.04	0.040	0.014	0.011

The impact of DEM resolution on obstacle threshold and  $z_0$  was analyzed to determine the robustness of this alternative method. Since the terrain is not changing and only the sampling frequency is varying, the  $z_0$  values should remain fairly constant. Table 4.3 shows that the obstacle threshold increases as the resolution of the DEM becomes coarser. This occurs because the coarser resolution cannot capture the subtler changes in surface height over the debris cover. On the other hand, the estimations of  $z_0$  remain relatively constant ( $\pm 0.004$  m) as the DEM resolution is reduced to 0.04 m. The consistency of this method despite variations in DEM resolution and obstacle thresholds, and the objective approach for deriving the obstacle threshold using a 30% obstacle density lends confidence to this method. Furthermore, Nield et al. (2013b) found that

measures regarding surface heights are the best predictor of aerodynamic roughness, specifically for surfaces that comprise large elements or have patches of large and small elements. Therefore, it is expected that the obstacle threshold should vary for different sites as a function of their largest elements, which is consistent with the inter-site variability and the obstacle thresholds reported in this study.

### **4.5.3 Ablation stakes**

Ablation stakes were installed on 18-19 May 2014 approximately 1 m into the ice at 14 sites with debris thicknesses ranging from 0.07 to 0.54 m (Table 4.1). The ablation stakes were measured on 09 November 2014. At 11 of the 14 sites, the ablation stakes completely melted out of the ice indicating there was greater than 1 m of ablation. Sites 8, 13, and 15, had ablation measurements of 0.92, 0.85, and 0.89 m, respectively. These three sites had debris thicknesses of 0.20, 0.33, and 0.37 m and were oriented in the southern, northeast, and northwest directions, respectively. The lower ablation rates of Sites 13 and 15 compared to the other 12 sites is likely due to a combination of their debris thickness and aspect as they are oriented in a manner that receives less solar radiation throughout the day. Site 8 appears to be an anomaly as it has a smaller debris thickness than 8 of the sites with ablation stakes and a southerly aspect, which positions it in a manner to receive a greater amount of solar radiation throughout the day. It is possible that Site 8 had a higher albedo and/or a lower thermal conductivity, which would greatly reduce its ablation; unfortunately, these properties could not be measured in the field. Nevertheless, the ablation measurements indicate that understanding ablation rates on debris-covered glaciers is greatly influenced by slope, aspect, and properties of the debris (albedo, thermal conductivity, and surface roughness).

## 4.6 MODELED RESULTS

### 4.6.1 Model calibration

Three different methods were used to estimate the latent heat flux to determine how well each method models the measured debris temperatures. These methods are referred to as  $LE_{Rain}$ ,  $LE_{RH100}$ , and  $LE_{Dry}$ . The albedo, thermal conductivity, and surface roughness for each of the three methods were optimized by minimizing the sum of squares of the surface temperature for each site (Table 4.4). For the  $LE_{Rain}$  and  $LE_{RH100}$  model, 7 of the 10 sites had a thermal conductivity at the upper bound ( $1.62 \text{ W m}^{-1} \text{ K}^{-1}$ ), while for the  $LE_{Dry}$  model 9 of the 10 sites were at the upper bound. These results indicate that the selection of the upper bound for the thermal conductivity is important and its impact on model performance is detailed in the discussion section. The albedo values ranged from 0.10 – 0.40 and had an average value around 0.32, which is consistent with albedos measured in the Khumbu (Inoue and Yoshida, 1980; Kayastha et al., 2000; Nicholson and Benn, 2012; LeJeune et al., 2013). The values of  $z_0$  had an average around 0.014 m, which is consistent with  $z_0$  measured in this study and those reported on other debris-covered glaciers (Inoue and Yoshida, 1980; Takeuchi et al., 2000; Brock et al., 2010). For the  $LE_{Rain}$  and  $LE_{RH100}$  models, 5 of the 10 sites had a value of  $z_0$  at its lower bound (0.006 m), which highlights the importance of measuring the surface roughness of the debris cover and will be discussed in the sensitivity analysis.

Table 4.4: Optimized values of albedo, thermal conductivity, and surface roughness for three methods of estimating the latent heat flux during calibration period.

Site	$LE_{Rain}$			$LE_{RH100}$			$LE_{Dry}$		
	$\alpha$	$k^1$	$z_0^2$	$\alpha$	$k^1$	$z_0^2$	$\alpha$	$k^1$	$z_0^2$
4	0.26	1.62	0.006	0.24	1.62	0.006	0.23	1.62	0.011
5	0.40	1.62	0.014	0.40	1.62	0.013	0.40	1.62	0.017
6	0.40	1.29	0.043	0.40	1.35	0.043	0.40	1.31	0.043
11	0.37	1.62	0.006	0.37	1.62	0.006	0.39	1.62	0.006
13	0.10	0.92	0.025	0.16	1.03	0.015	0.10	1.62	0.021
14	0.39	1.61	0.015	0.40	1.62	0.012	0.39	1.62	0.017
15	0.38	1.62	0.006	0.37	1.62	0.006	0.38	1.62	0.006
17	0.30	1.62	0.006	0.30	1.55	0.006	0.30	1.62	0.006
19	0.33	1.62	0.019	0.37	1.62	0.013	0.30	1.62	0.028
20	0.28	1.62	0.006	0.29	1.62	0.006	0.30	1.62	0.006
Avg	0.32	1.52	0.015	0.33	1.53	0.013	0.32	1.59	0.016
Std	0.09	0.23	0.012	0.08	0.19	0.011	0.10	0.10	0.012

<sup>1</sup>units of  $W\ m^{-1}\ K^{-1}$ ; <sup>2</sup>units of m

The performance of each model was assessed using the total sum of squares and the  $R^2$  correlation coefficients. The  $R^2$  values ranged from 0.34 to 0.92 for all three models. The average  $R^2$  values over the calibration period for the  $LE_{Rain}$ ,  $LE_{RH100}$ , and  $LE_{Dry}$  models were 0.72, 0.72, and 0.71, respectively. Figures 4.5C and 4.5D show the correlation between the modeled and measured surface temperature at Site 11, which had an  $R^2$  of 0.77 and 0.75 for the calibration and validation periods, respectively. Figure 4.5C shows there is good agreement between the modeled and measured temperature sensors. The modeled temperatures appear to capture the daily variations in temperature

well. However, there are a few days for which a positive bias in temperature can be seen during the daily high and nightly low (e.g., Figure 4.5C from 16-18 June and 25-27 July). Interestingly, the overestimation of the daily high typically occurs after the nightly low has a positive bias in temperature during the previous night. The positive bias of the nightly minimum is apparent between the hours of 0:00 and 6:00 (Figure 4.6). One possible explanation for the positive bias in temperature in the nightly low is an overestimation of the incoming longwave radiation due to the poor temporal and spatial resolution of the NCEP/NCAR reanalysis dataset compared to the other meteorological data from Pyramid Station. Typically, the wind speed during the night is relatively low thereby limiting the turbulent heat fluxes, which causes the incoming longwave radiation to be a major source of energy during this time.

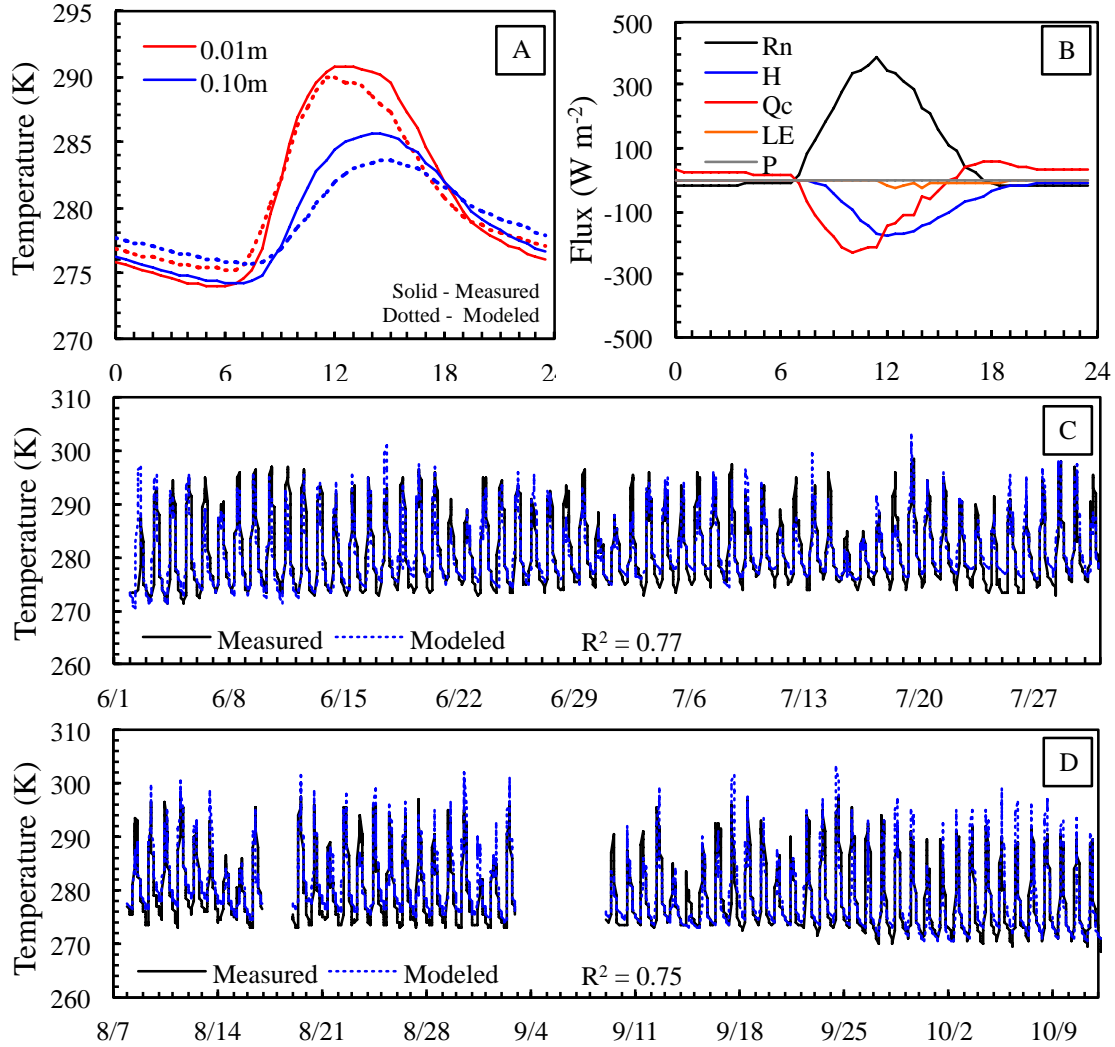


Figure 4.5: Various plots for Site 11 using the  $LE_{Rain}$  model showing (A) average daily temperatures at two depths (solid and dashed lines indicate measured and modeled temperatures, respectively), (B) average daily energy fluxes, (C) measured and modeled temperatures at a depth of 0.01 m over the calibration period, and (D) measured and modeled temperatures over the validation period.

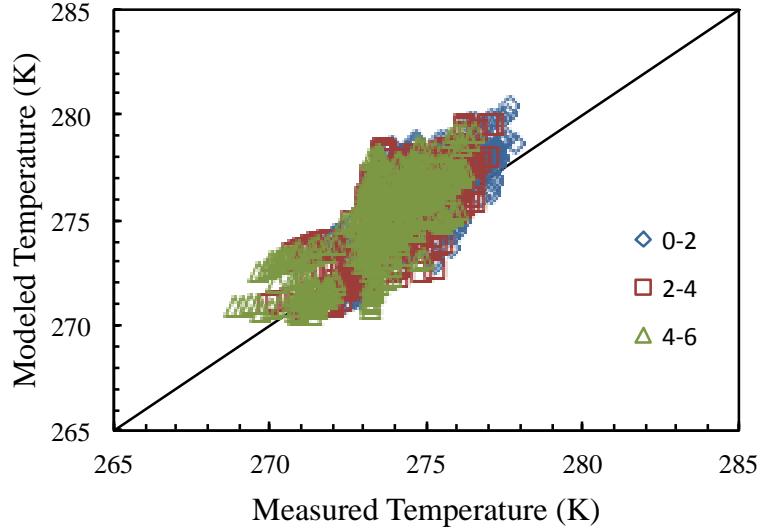


Figure 4.6: Scatterplot of measured and modeled temperature for Site 11 at the surface for the  $LE_{Rain}$  model showing the positive temperature bias overnight.

Nonetheless, the model performs reasonably well for all of the temperature sensors. Unfortunately, it is difficult to determine which latent heat flux model performs the best using the total sum of squares and/or the  $R^2$  values as there was not one particular model that consistently had a lower total sum of squares and/or a higher  $R^2$  at each site. The average  $R^2$  value was fairly comparable for all three models. The total sum of squares of all the sites was the lowest for the  $LE_{RH100}$  model followed by the  $LE_{Rain}$  model and then the  $LE_{Dry}$  model, but the difference between models was less than 5%.

#### 4.6.2 Model validation

Model validation was assessed from 08 August to 12 October 2014 for all three models using the  $R^2$  values for each temperature sensor. The  $R^2$  values for all the temperature sensors at the 10 sites ranged from 0.39 to 0.81 for all three methods. The average  $R^2$  value for the  $LE_{Rain}$ ,  $LE_{RH100}$ , and  $LE_{Dry}$  was 0.67, 0.67, and 0.68,

respectively. Again, the similar performance between the three models does not provide any insight into preference for one model and is likely a result of the calibration procedure. Figure 4.5D shows that the  $LE_{Rain}$  model performs well through the entire validation period. Similar to the calibration period, the  $LE_{Rain}$  model appears to underestimate the nightly low, which causes the following daily high to be overestimated.

Reid and Brock (2010) found  $R^2$  values of 0.94 and 0.52 for temperature sensors at the surface and at a depth of 15 cm, respectively. While the  $R^2$  value of 0.94 is higher than those found in this study, the range of  $R^2$  is comparable. In contrast to the findings of Reid and Brock (2010), the average  $R^2$  value for the surface temperature sensors (0.67-0.68 for all three models) was very similar to the average  $R^2$  value of those buried in the debris (0.66-0.68 for all three models). The slightly lower  $R^2$  values in this study may be a result of using meteorological data from an AWS located 14 km away from the glacier. Furthermore, longwave radiation was estimated from remotely sensed data, which may also influence model performance as previously discussed.

#### **4.6.3 Modeled ablation rates**

Ablation rates were computed for all 15 sites that had a temperature sensor or an ablation stake. For sites that only had an ablation stake, the average calibrated parameters for that particular latent heat flux model were used. Additionally, ablation rates were estimated for the  $LE_{Rain}$  model using the average calibrated parameters for all the sites to assess the differences between using a single set of parameters compared to optimizing the parameters at each site. The modeled ablation over the entire duration of the study period varied from 0.39 to 2.85 m among the three methods (Figure 4.7). On average the  $LE_{Dry}$  model overestimated both the  $LE_{Rain}$  and  $LE_{RH100}$  models by 7.9%. The slight variations in ablation between the models are directly related to the differences in

their calibrated parameters. The slightly higher ablation rates for the  $LE_{Dry}$  model is likely attributed to the higher values of thermal conductivities and the lack of a latent heat flux term to remove heat from the debris. Figure 4.7 shows there is a clear relationship between debris thickness and ablation as thin debris has higher rates of ablation compared to thicker debris, which insulates the ice to a greater extent thereby retarding ablation. The scatter found throughout the curve, specifically between 0.25 and 0.50 m, is due to the site-specific debris properties and the slope and aspect of each site. A comparison between the  $LE_{Rain}$  model using the optimized parameters at each site and those using the average calibrated parameters at each site highlights the effect that site-specific properties has on ablation. Site 6, with a debris thickness of 0.08 m, is a good example as the use of average calibrated parameters increased the melt from 2.03 m to 2.70 m due to an increase in thermal conductivity from  $1.29 \text{ W m}^{-1} \text{ K}^{-1}$  to  $1.52 \text{ W m}^{-1} \text{ K}^{-1}$ . These differences in melt and the sensitivity to thermal conductivity highlight the importance of properly estimating/measuring the thermal conductivity of the debris cover.

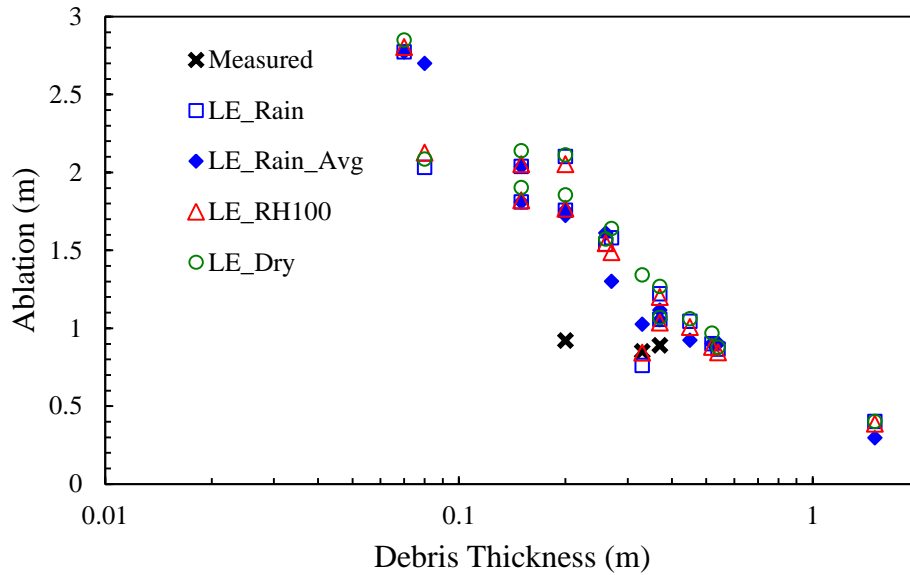


Figure 4.7: Modeled ablation with respect to debris thickness for all 15 sites from 18 May to 09 November 2014 for each of the three latent heat flux models including the  $LE_{Rain}$  model with average values and the three measured stakes that did not exceed 1 m.

The modeled ablation rates may also be compared to the measured ablation rates. Specifically, Sites 8, 13, and 15 had measured ablation rates of 0.92, 0.85 and 0.89 m compared to their modeled ablation rates of 1.76, 0.76, and 1.22 m, respectively, for the  $LE_{Rain}$  model. The large discrepancy between the measured and modeled ablation rates at Site 8 may be due to the lack of knowledge of the debris properties at Site 8 as previously discussed. The difference between the modeled and measured ablation rates at Site 15 may also be a result of the thermal conductivity parameter ( $1.61 \text{ W m}^{-1} \text{ K}^{-1}$ ), which is slightly higher than thermal conductivities previously reported in the Khumbu, which ranged from  $0.60$  to  $1.29 \text{ W m}^{-1} \text{ K}^{-1}$ . A comparison of the daily average temperatures for Site 15 reveals there was about an hour lag between the modeled and measured temperatures (results not shown). Lags between temperatures are typically a result of

their depth (Conway and Rasmussen, 2000), which is apparent in Figure 4.5A as the 0.10 m sensor lags behind the 0.01 m sensor. It is possible that debris may have shifted over the melt season causing the measured temperature to be at a lower depth than 0.01 m, which would greatly influence the model calibration and potentially cause the thermal conductivity to vary. Site 5 was the only other site where a slight lag was observed between the measured and modeled temperatures. The modeled ablation at Site 5 was 0.87 m using the  $LE_{Rain}$  model, while the ablation stake melted completely out of the ice indicating greater than 1 m of ablation. All the other model estimates of ablation were near to or greater than 1 m, which was also observed by their respective ablation stakes as they completely melted out of the ice.

The ablation results also show strong seasonal trends with maximum melt rates occurring in June, July, and August. These ablation rates appear to taper off towards the transition seasons. Melt rates in July and August ranged from 0.3 – 2.5 cm day<sup>-1</sup> based on the debris thickness, which is consistent with empirical relationships between mean daily ablation rate and debris thickness found on other glaciers (Nicholson and Benn, 2006). The total ablation rates may also be compared to measured surface elevation changes on Imja-Lhotse Shar Glacier derived from multiple DEMs, which were found to range from  $-0.82 \pm 0.61$  m yr<sup>-1</sup> to  $-1.56 \pm 0.80$  m yr<sup>-1</sup> (Bolch et al., 2011b, Nuimura et al., 2012; Gardelle et al., 2013; Thakuri et al., 2015) for various time periods between 1999 and 2014. It is important to note that the mass balance estimates in these studies have been converted back to elevation changes using the ice density reported in each study. The total ablation rates are similar to the measured changes in surface elevation, which lends confidence to the results.

#### 4.6.4 Sensitivity analysis

A sensitivity analysis was performed to assess how albedo, thermal conductivity, and surface roughness affect the total ablation (Table 4.5) based on the uncertainty with respect to each parameter. The uncertainty in thermal conductivity was  $\pm 0.40 \text{ W m}^{-1} \text{ K}^{-1}$ , which captures the approximate difference between the highest thermal conductivity measured in this study ( $1.62 \text{ W m}^{-1} \text{ K}^{-1}$ ) and the higher end of those previously reported (Conway and Rasmussen, 2000; Nicholson and Benn, 2012; Rounce and McKinney, 2014). The uncertainty associated with the surface roughness was  $\pm 0.010 \text{ m}$ , which is the approximate standard deviation associated with the  $z_0$  values for each of the three models (Table 4.4) and similar to the standard deviation between the four sites where  $z_0$  was measured ( $\pm 0.016 \text{ m}$ ). Lastly, the uncertainty of the albedo was estimated as  $\pm 0.10$ , which is the approximate standard deviation within the model calibration for each of the three models and also the difference between the mean and median albedo measured by Nicholson and Benn (2012) on Ngozumpa glacier. The  $LE_{\text{Rain}}$  model was used as the baseline case and the average value for each of the calibrated parameters ( $\alpha$ ,  $k$ ,  $z_0$ ) from the model optimized was used for each site.

Table 4.5: Sensitivity analysis showing percent changes relative to the total melt (m) as a function of the uncertainty associated with the calibrated parameters ( $\alpha$ ,  $k$ ,  $z_0$ ) for all sites over the study period using the  $LE_{\text{Rain}}$  model in conjunction with the average calibrated parameters for all sites.

Parameter		$\alpha$		$k$		$z_0$	
Adjustment		+ 0.10	- 0.10	+ 0.40	- 0.40	+ 0.010	- 0.010
Site	Total Melt (m)	% Change					
4	0.30	-12.3	+13.0	+30.1	-29.4	-9.7	+21.7
5	0.90	-12.6	+13.0	+22.3	-24.0	-9.2	+19.4
6	2.70	-11.1	+11.3	+13.1	-16.3	-4.1	+7.9
7	0.92	-12.6	+12.6	+22.0	-23.5	-8.8	+18.8
8	1.03	-11.6	+11.9	+20.7	-22.5	-7.7	+16.1
10	1.61	-12.2	+12.1	+18.9	-21.2	-7.7	+15.3
11	1.12	-12.0	+12.5	+20.3	-22.1	-7.7	+16.2
12	1.30	-11.8	+12.0	+19.8	-21.9	-7.8	+16.1
13	1.05	-12.4	+12.7	+21.2	-22.9	-8.5	+17.8
14	1.72	-11.9	+11.8	+18.1	-20.7	-7.0	+14.1
15	0.90	-12.4	+12.9	+21.8	-23.4	-8.6	+17.7
16	1.76	-11.6	+12.1	+18.3	-20.2	-6.7	+14.0
17	2.77	-10.8	+11.1	+12.0	-15.0	-2.9	+5.7
19	2.04	-11.6	+11.7	+16.5	-19.4	-6.3	+12.3
20	1.81	-11.4	+11.4	+16.5	-19.4	-6.1	+12.1
<b>Average</b>		<b>-11.9</b>	<b>+12.1</b>	<b>+19.4</b>	<b>-21.5</b>	<b>-7.3</b>	<b>+15.0</b>

Table 4.5 shows the total ablation is most sensitive to changes in the thermal conductivity, where a  $\pm 0.40 \text{ W m}^{-1} \text{ K}^{-1}$  change causes a  $\pm 20.5\%$  change in total ablation on average. The uncertainty associated with the thermal conductivity is also more sensitive to thicker debris, which is consistent with the findings of Nicholson and Benn (2012). Total ablation is also moderately sensitive to changes in the albedo, where a  $\pm 0.10$  change causes a  $\pm 12.0\%$  change in total ablation. Lastly, the total ablation is least sensitive to changes in increasing the surface roughness, as a  $+0.010 \text{ m}$  increase in  $z_0$

only caused a -7.3% change in total ablation. However, the model was quite sensitive to a reduction in the  $z_0$  of -0.010 m, which caused an average change in total ablation of +15.0%. The sensitivity associated with  $z_0$  also appears to increase with an increase in debris thickness. These results highlight the importance of properly estimating the thermal conductivity, but also show the surface roughness and the albedo are important as well.

#### **4.6.5 Temporal resolution**

Nicholson and Benn (2006) proposed that the temperature gradient in the debris may be assumed to be linear at a time step greater than a day, but is nonlinear for shorter time steps. This would have important implications for modeling melt on remote debris-covered glaciers where meteorological data is not available and reanalysis datasets could be used instead. The importance of temporal resolution was analyzed using 6-hour and daily average data from Pyramid Station, which are consistent with the temporal resolution of NCEP/NCAR reanalysis datasets. To be consistent with this reanalysis dataset such that only the effects of temporal resolution were analyzed, the wind speed and relative humidity used were instantaneous values from Pyramid Station, while all the other variables were 6-hour averages. For the daily time step, all the parameters were daily averages and the temperature profile in the debris is assumed to be linear. The  $LE_{Rain}$  model was used to model the latent heat flux.

The  $R^2$  correlation coefficients for the sites with temperature sensors and the modeled total melt for all 15 sites were used to assess the effect of temporal resolution on model performance. The  $R^2$  using the 6-hour data ranged from 0.30 to 0.80 with an average of 0.55 over the calibration period and was significantly poorer during the validation period with  $R^2$  values ranging from 0.15 to 0.65 with an average of 0.35.

Figure 4.8A shows the surface temperature at Site 11 does fairly well ( $R^2 = 0.63$ ) at modeling the measured surface temperatures over the calibration period. The lower  $R^2$  values compared to the 30 minute time step appears to be a result of the 6-hour model underestimating the daily high, which occurs around 15:00 each day. Furthermore, Figure 4.8B shows the 6-hour model poorly replicates the measured data towards the transition seasons when snowfall becomes significant, which explains the poorer  $R^2$  values for the validation period. Snowfall is problematic in the model for large time steps because the model assumes the snow is on the surface for the entire time step. Therefore, a small snow event that could melt quickly on the debris and then allow the debris to warm up during the day is perceived to remain on the snow for the 6-hour time step (e.g., Figure 4.8B from 27 Sept to 03 October). The same problem arises at the daily time step, so a snow-free model was used instead. For the daily time step, the  $R^2$  values ranged from 0.18 to 0.63 with an average of 0.29. Figure 4.8C shows the daily time step is able to capture some of the temperature fluctuations over the melt season, but does not perform as well as the 30-minute or 6-hour models.

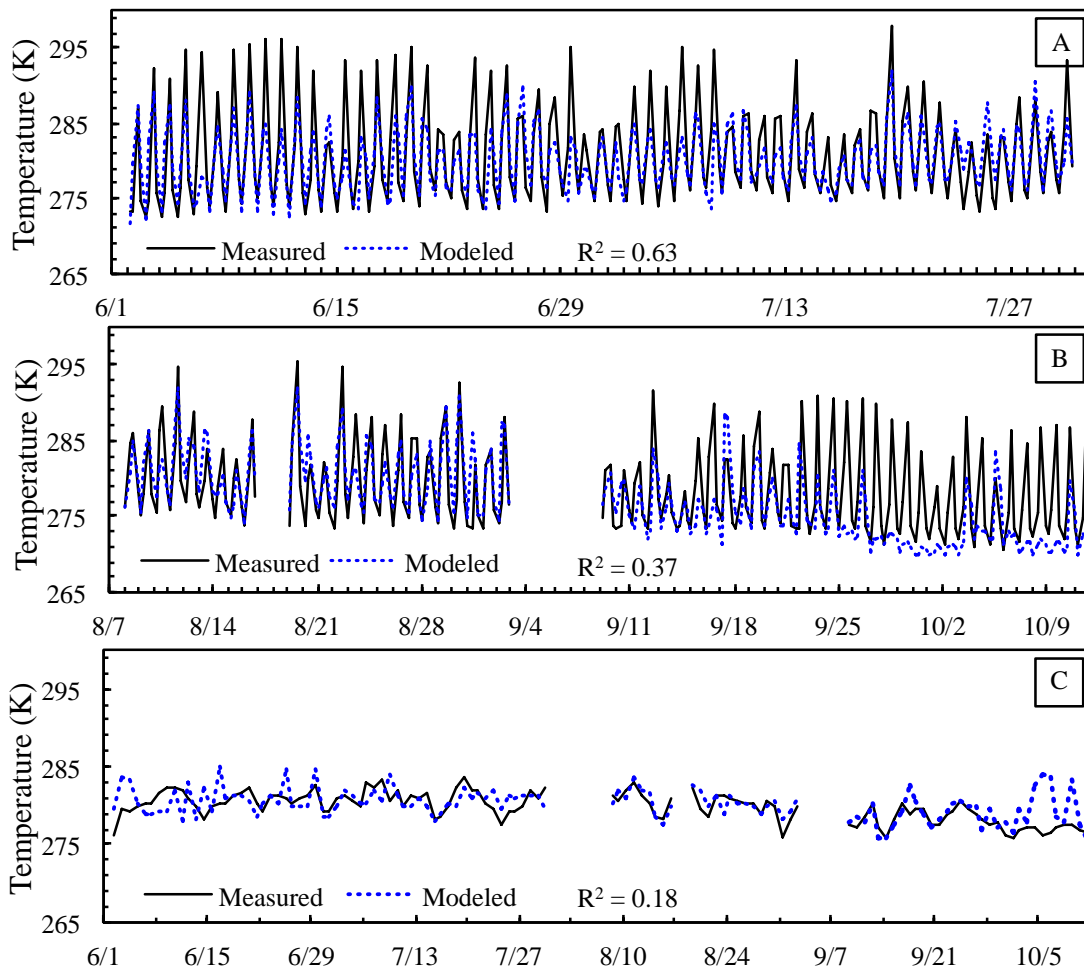


Figure 4.8: Modeled and measured surface temperature at Site 11 over the (A) calibration period and (B) validation period using 6-hour data, and (C) entire period using daily averages.

Since we are most interested in understanding the effects of temporal resolution, the 6-hour data and daily averages from 02 June to 25 September 2014 were assessed, which is prior to the time when snowfall was recorded each day. A comparison of all the modeled and measured temperatures at the surface reveals the 6-hour model underestimates the measured temperatures by an average of  $1.0 (\pm 4.3)$  K over the entire

time period. The modeled total ablation from 02 June to 25 September reveals the ablation is consistently underestimated at all sites by an average of 11 ( $\pm 5$ ) %. The lower estimates of ablation are likely a result of the underestimation of the daily high as previously discussed. Similar to the 6-hour model, the daily time step model slightly underestimates the measured temperatures at the surface on average by 0.3 ( $\pm 1.9$ ) K. The modeled total ablation is also underestimated by an average of 6 ( $\pm 10$ ) %. However, it is important to note that 5 of the 15 sites actually slightly overestimated the melt. These results suggest that if high-temporal meteorological data are not available, a first-order estimate of ablation over a melt season could be obtained using the daily time step model. It is important that the estimate is made over the entire melt season, as the daily model does not capture the daily temperature fluctuations well. Furthermore, caution should be used to avoid the transition seasons as both the daily model and the 6-hour model do not have a small enough time step to properly account for snow melt.

## **4.7 FIELD RESULTS**

### **4.7.1 Thermal conductivity**

One of the limitations with regards to the thermal conductivity measurements is that all the measurements were made near the surface. Therefore, the estimates of the average thermal conductivity at each site are potentially underestimated because the deeper layers that may be more compact and humid are not considered. The lack of any trends with respect to depth appears to dispute this theory; however, this is based on a limited number of measurements near the surface. Interestingly, the thermal conductivities measured at Sites 4 and 11 are similar to those estimated by Nicholson and Benn (2012) for debris cover on Ngozumpa glacier with 10% and 20% of the void space being filled with water (1.42 and 1.55  $\text{W m}^{-1} \text{K}^{-1}$ , respectively).

The number of sites that reached the upper bound during the model calibration is concerning as it may indicate that the actual thermal conductivity throughout the debris is higher. To address this issue, an additional calibration was performed allowing the thermal conductivity to be unbounded. This calibration revealed that 3 or more out of the 10 sites for each method had thermal conductivities greater than  $3.0 \text{ W m}^{-1} \text{ K}^{-1}$  with one thermal conductivity as high as  $4.5 \text{ W m}^{-1} \text{ K}^{-1}$ . The lithology of the debris cover in the Everest region is predominantly granite, gneiss, and pelite (Hambrey et al., 2008). Robertson (1988) found the thermal conductivity of solid granite gneiss to be  $2.87 \text{ W m}^{-1} \text{ K}^{-1}$ , so the unbounded thermal conductivities do not appear to make physical sense when one considers that the thermal conductivity of debris should be much lower than solid rock due to the pore spaces being filled with air and water. Furthermore, an optimization performed using the total sum of squares of all the surface sites reveals that increasing the thermal conductivity from  $1.6 \text{ W m}^{-1} \text{ K}^{-1}$  to its minimum of  $2.6 \text{ W m}^{-1} \text{ K}^{-1}$  only reduces the total sum of squares by 3%. These results and the similar values to Nicholson and Benn (2012) lend confidence to the use of  $1.62 \text{ W m}^{-1} \text{ K}^{-1}$  as the upper bound, but highlights the importance of understanding how the moisture varies within the debris and its influence on the thermal conductivity. Future work should improve measurements of the thermal conductivity by a) accurately measuring the depth of the temperature sensors during installation and retrieval, b) installing additional sensors (e.g. 5 cm spacing) that allow thermal conductivity within the debris to be computed at more depths, and c) measuring moisture in the debris at various depths.

#### **4.7.2 Surface roughness**

The development of an alternative method for estimating  $z_0$  was required, as the Lettau-Munro method appeared to greatly underestimate the values of  $z_0$ . The alternative

method applies the relationship developed by Lettau (1969) to a high resolution DEM using the selection of an obstacle height (threshold) based on an obstacle density of 30%. One of the main limitations of this study is the lack of aerodynamic roughness measurements to validate the developed methods. Previous work, e.g., Rees and Arnold (2006), has relied upon surface roughness estimates from other studies to assess the reasonableness of their results when aerodynamic data were not collected. This study relies upon the results of Inoue and Yoshida (1980), which estimated surface roughness using wind speed profiles at two sites on the Khumbu glacier. Specifically, Sites B and C in this study have similar debris cover to Areas III and IV from Inoue and Yoshida (1980), respectively.

Site B had the highest value of  $z_0$  (0.043 m) of the four sites in this study and consisted of larger boulders up to 1 m in size. This value is similar to the higher value of 0.060 m for  $z_0$  derived from a region on the Khumbu glacier that consisted of large granitic boulders of 1-2 m in size lying on top of schistose rocks with a grain size varying from a few centimeters to 0.5 m (Inoue and Yoshida, 1980). The larger boulders observed by Inoue and Yoshida (1980) may explain the slightly higher value of  $z_0$  compared to Site B. Site C, which comprised the smallest grain sizes of the four sites in this study, agrees well with the smaller value of  $z_0$  (0.0035 m) derived by Inoue and Yoshida (1980) for an area where the supraglacial debris comprised dispersed boulders ranging in size of 0.01 – 0.05 m. The few boulders ranging in size of up to 0.15 m may be the reason for Site C's slightly larger value of  $z_0$  (0.006 m). Sites A and D were composed of boulders and grains that varied in size between those found in Sites B and C; therefore, we deem the value of  $z_0$  of 0.016 and 0.014 m for Sites A and D, respectively, to be reasonable. Furthermore, these values agree fairly well with the  $z_0$  of 0.016 m measured by Brock et al. (2010) on a debris-covered glacier in Italy that

comprised a mixture of granites and schists of predominantly cobble size, with occasional boulders of  $< 1$  m size.

Future work should seek to compare these estimates of surface roughness with aerodynamic roughness to determine the scale at which these two values agree. Brock et al. (2006) found there to be no significant difference between the use of a 3 m and 15 m transect; however, they did state that a shorter pole would be unlikely to capture a sufficient sample of roughness elements if the vertical changes are greater than 1 m. The use of hundreds of transects over a  $\sim 4$  m<sup>2</sup> grid has the benefit of expanding the number of surface roughness elements that can be captured compared to a single transect. However, Brock et al. (2006) compared microtopographic and aerodynamic roughness over snow, slush, and ice, which is significantly different from the hummocky and heterogeneous terrain on debris-covered glaciers. Therefore, it will be important to determine the scale or fetch length at which the surface roughness agrees with the aerodynamic roughness. Nonetheless, the method developed in this paper provides an objective approach to select an obstacle height and yields consistent and reasonable estimates of  $z_0$  for various grain sizes independent of the resolution of the DEM.

#### **4.7.3 Modeled results**

One of the limitations of the calibration procedure is the  $LE_{\text{Rain}}$ ,  $LE_{\text{RH100}}$ , and  $LE_{\text{Dry}}$  models all performed reasonably well. The lack of a single model clearly outperforming the others indicates that either a) the modeling of the latent heat flux is insignificant or b) the latent heat flux is significant, but the calibration procedure allows for changes in the latent heat flux to be compensated for via other model parameters. Brock et al. (2010) found that latent heat fluxes may be a significant energy sink when rain falls on warm debris indicating that the latent heat flux is important to include. They

also assessed the importance of each component of the energy balance and found that including the latent heat flux improved the correlation coefficient of their model. The average latent heat flux for both the  $LE_{Rain}$  and  $LE_{RH100}$  models were comparable with values ranging from -53 to 10  $W m^{-2}$  over the day. The peak instantaneous latent heat fluxes varied greatly between the two models with fluxes as high as -714 and -323  $W m^{-2}$ , for the  $LE_{Rain}$  and  $LE_{RH100}$  models, respectively. These values are similar to those reported by Brock et al. (2010) and support the importance of including the latent heat flux term. However, they do not yield any insight into preference between the  $LE_{Rain}$  or  $LE_{RH100}$  models. These results suggest that the selection of the  $LE_{Rain}$  or  $LE_{RH100}$  model should be based on data availability. Future work should seek to measure the thermal conductivity, albedo, and surface roughness, which would allow the differences between models to be evaluated. Furthermore, detailed knowledge of the debris properties, including how the thermal conductivity and water content vary with depth, would allow the performance of these models to be compared to other debris-covered glacier energy balance models (Collier et al., 2014; Fujita and Sakai, 2014).

#### **4.8 CONCLUSIONS**

Debris thickness greatly impacts ablation rates on debris-covered glaciers; however, incorporating debris cover into energy balance models is still hampered by a lack of knowledge of the debris properties. Fieldwork performed on Imja-Lhotse Shar Glacier over the 2014 melt season was used to develop new techniques to measure surface roughness, which yielded reasonable values for various grain sizes. Temperature sensors and ablation stakes installed in the debris were also used to assess the performance of a debris-covered glacier energy balance model using three different methods for estimating the latent heat flux. All three models performed well, as a result

of the calibration procedure, which allowed variations in the lack of latent heat flux to be compensated for by adjusting the debris properties. However, the  $LE_{Rain}$  and  $LE_{RH100}$  models yielded more reasonable values of latent heat fluxes. This suggests that in a data-scarce region either the  $LE_{Rain}$  or  $LE_{RH100}$  model may be used if relative humidity or precipitation data are available.

A sensitivity analysis revealed ablation rates were most sensitive to variations in thermal conductivity, followed closely by albedo and surface roughness. This highlights the importance of measuring the thermal conductivity and the moisture content in the debris. The effect of temporal resolution on model performance was also explored using a 6-hour time step and a daily time step. The 6-hour time step was found to underestimate the daily high each day, which caused the ablation rates to also be slightly underestimated. The daily time step did not model the daily average temperature as well, but yielded better estimates of ablation over the entire melt season.

Future studies should continue to work on incorporating the water content in the debris into debris-covered glacier energy balance models and determine its effect on thermal conductivity and the latent heat flux. Furthermore, an increased understanding of how the albedo may vary over the course of the day, the course of the melt season, and as a function of debris saturation, may significantly improve model performance. Lastly, the methods developed in this study have the potential to be scaled up such that maps of surface roughness on a whole glacier scale may be developed in the future, but it is imperative to determine the scale at which the surface roughness and aerodynamic roughness agree with one another.

#### **4.9 ACKNOWLEDGEMENTS**

The authors acknowledge the support of the USAID Climate Change Resilient Development (CCRD) project for the support of Rounce. The meteorological data from Pyramid Station used in this study was collected within the SHARE Project thanks to contributions from the Italian National Research Council and the Italian Ministry of Foreign Affairs. The NCEP Reanalysis data provided by the NOAA/OAR/ESRL PSD, Boulder, Colorado USA from their website <http://www.esrl.noaa.gov/psd/> was also very helpful. We also acknowledge the support of Dr. Dhananjay Regmi of Himalayan Research Expeditions for temperature sensors and logistical support during fieldwork.

## **Chapter 5: A new remote hazard and risk assessment framework for glacial lakes in the Nepal Himalaya**

David Rounce, Daene McKinney, Jonathan Lala, Alton Byers, and Cameron Watson

Submitted to Hydrology and Earth System Sciences (April 8, 2016)

### **5.1 ABSTRACT**

Glacial lake outburst floods (GLOFs) pose a significant threat to downstream communities and infrastructure due to their potential to rapidly unleash stored lake water. The most common triggers of these GLOFs are mass movement entering the lake and/or the self-destruction of the terminal moraine due to hydrostatic pressures or a buried ice core. This study initially uses previous qualitative and quantitative assessments to understand the hazards associated with eight glacial lakes in the Nepal Himalaya that are widely considered to be highly dangerous. The previous assessments yield conflicting classifications with respect to each glacial lake, which spurred the development of a new holistic, reproducible, and objective approach based solely on remotely sensed data. This remote hazard assessment analyzes mass movement entering the lake, the stability of the moraine, and lake growth in conjunction with a geometric GLOF to determine the downstream impacts such that the present and future risk associated with each glacial lake may be quantified. The new approach is developed within a hazard, risk, and management action framework with the aim that this remote assessment may guide future field campaigns, modeling efforts, and ultimately risk-mitigation strategies. The remote assessment was found to provide valuable information regarding the hazards faced by each glacial lake and results were discussed within the context of the current state of knowledge to help guide future efforts.

## 5.2 INTRODUCTION

Glacial lakes outburst floods (GLOFs) unleash stored lake water often causing enormous devastation downstream that can include high death tolls as well as the destruction of valuable lands and costly infrastructure. As the number and area of glacial lakes continues to increase (Bajracharya and Mool, 2009; Bolch et al., 2011; Gardelle et al., 2011; Carrivick and Tweed, 2013), the risk associated with these GLOFs increases as well. An assessment of previous GLOFs reveals the most common cause of failure is mass movement (snow, ice, and/or rock) entering the lake (Richardson and Reynolds, 2000; Wang et al., 2012; Emmer and Cochachin, 2013) and subsequently overtopping and eroding the damming moraine. Other triggering mechanisms may include dam settlement and/or piping, the degradation of an ice-cored moraine, the rapid input of water from extreme events, and seismic events (Westoby et al., 2014). Events that occur over a relatively short time period, i.e., minutes to days, such as mass movement entering the lake, intensive rainfall, or intensive snowmelt are referred to as dynamic events, while other events that occur over longer periods of time are referred to as self-destruction or long-term causes (Yamada, 1998; Emmer and Cochachin, 2013). Emmer and Cochachin (2013) highlight the complexity of these self-destructive events as they lump the failure from the degradation of buried ice, hydrostatic pressure, and/or the effects of time all together due to the difficulty of distinguishing the exact cause of failure. Similarly, Richardson and Reynolds (2000) were unable to identify the cause of over 23% of the GLOFs in their study due to a lack of information. This uncertainty regarding other mechanisms of failure stresses the importance of taking a holistic approach towards assessing the hazard of these glacial lakes that accounts for the various triggering mechanisms and the stability of the moraine.

Methods have been developed to characterize the hazard and risk associated with glacial lakes in Cordillera Blanca (Reynolds, 2003; Hegglin and Huggel, 2008; Emmer and Vilímek, 2013; Emmer and Vilímek, 2014), New Zealand (Allen et al., 2009), North America (Clague and Evans, 2000; O'Connor et al., 2001; McKillop and Clague, 2007a, b), the Swiss Alps (Huggel et al., 2004b; Nussbaumer et al., 2014), the Himalaya (Wang et al., 2008; ICIMOD, 2011; Wang et al., 2012; Fujita et al., 2013; Worni et al., 2013), the Tibetan Plateau (Wang et al., 2011), and other parts of high mountain Asia (Bolch et al., 2011; Mergili and Schneider, 2011). These methods vary considerably based on the parameters considered, the level of importance placed upon each parameter, the amount and type of required input data, their ability to be transferred to other regions, and their levels of objectivity. Emmer and Vilímek (2013) applied a suite of existing hazard assessments to glacial lakes in Cordillera Blanca and found good agreement between the various methods despite the various studies using different parameters, various amounts of qualitative and quantitative information, and being developed for specific regions. This good agreement suggests it may be feasible to accurately classify the hazard of a glacial lake and shows the parameters may be qualitative or quantitative as long as the developed analysis and thresholds are objective.

Unfortunately, the use of various approaches can also lead to different classifications of the hazard associated with an individual glacial lake. Imja Tsho<sup>1</sup>, located in the Everest region of Nepal, provides an excellent example of these conflicting classifications. Some studies have stated that Imja Tsho is safe (Watanabe et al., 2009; Fujita et al., 2013), a very low risk (Hambrey et al., 2008), or a moderate risk (Budhathoki et al., 2010). Conversely, ICIMOD (2011) identified Imja Tsho as one of

---

<sup>1</sup> Tsho is Tibetan for lake.

six glacial lakes in Nepal that is a high priority for further investigation and currently remediation efforts to reduce its hazard are under way (UNDP, 2013). These remediation efforts and a similar project completed at Tsho Rolpa (Rana et al., 2000) are excellent steps forward for Nepal with respect to addressing the hazards associated with its glacial lakes. However, it is important that these efforts and resources are properly directed to ensure the development of the most cost-effective, Nepal-specific methods for successfully reducing the risk of glacial lakes as practiced by the Peruvians since the 1950s (Carey, 2010). Conflicting classifications of Imja Tsho suggest relief efforts may be misguided if the lake is indeed safe and also send mixed signals to the general public and downstream communities that these studies are meant to assist. Another good example of these conflicting reports is Chamlang South Tsho (also referred to as West Chamlang), where one study stated the lake was not particularly dangerous (Byers et al., 2013) while another stated the lake was potentially dangerous (Lamsal et al., 2016) despite having access to the same data sets.

These various assessments and conclusions highlight the importance of (1) developing a clear and straight forward holistic method for assessing the hazard associated with a glacial lake and (2) constructing a framework that guides management actions for a given glacial lake that accounts for the various levels of data collection, modeling, and field campaigns. An additional aspect that is important to incorporate is how the hazard associated with these glacial lakes will change as the glacier and glacial lakes continue to evolve. This is especially important when one considers that successful remediation strategies on hazardous lakes often take more than a decade to secure funding and implement (Quincey et al., 2007).

This study assesses the performance of existing hazard assessment methods on potentially dangerous glacial lakes in Nepal to determine how well they agree with one

another. These existing studies are used as the basis for developing a new holistic approach that is objective, repeatable, and uses readily available information such that it may be applied to any glacial lake. This approach will be developed within a management action framework such that it may be used to guide future field campaigns, research, and ultimately risk-mitigation strategies associated with hazardous glacial lakes.

### **5.3 STUDY AREA**

This study assesses the hazard and risk of GLOFs at eight glacial lakes in the Nepal Himalaya (Figure 1). Six of these glacial lakes were identified by ICIMOD (2011) as being high priority for further investigation: Tsho Rolpa, Lower Barun Tsho, Imja Tsho, Lunding Tsho (also referred to as Tsho Og), Chamlang South Tsho (also referred to as West Chamlang), and Thulagi Tsho. The other two glacial lakes considered are Chamlang North Tsho (also referred to as Lake 464), which was found to be dangerous (Byers et al., 2013) and Dig Tsho, which experienced a GLOF in 1985 (Vuichard and Zimmermann, 1987). The level of investigation of each of lake is highly variable.



Figure 5.1: The location of the eight glacial lakes assessed in this study in the Nepal Himalaya.

The three glacial lakes that have received the most attention are Imja Tsho ( $86^{\circ}55.5'$  E,  $27^{\circ}53.9'$  N, 5007.7 m.a.s.l.), Tsho Rolpa ( $86^{\circ}28.6'$  E,  $27^{\circ}51.7'$  N, 4527.8 m.a.s.l.), and Thulagi Tsho ( $84^{\circ}29.1'$  E,  $28^{\circ}29.3'$  N, 4014.8 m.a.s.l.). ICIMOD (2011) provides a detailed review of the development of these lakes and the field investigations that have been performed to measure the bathymetry, use geophysical techniques to identify the presence of buried ice, and broadly investigate the hazard associated with these lakes. Since this study, the stability of their terminal moraines has been investigated (Fujita et al., 2013) and potential GLOFs have been modeled (Khanal et al., 2015). Additionally, a laboratory experiment was conducted to model the stability of Tsho Rolpa (Shrestha et al., 2013) and other detailed investigations of Imja Tsho's

bathymetry (Somos-Valenzuela et al., 2014) and potential floods (Bajracharya et al., 2007; Somos-Valenzuela et al., 2015) have been conducted. Tsho Rolpa is also the only glacial lake in Nepal that has been remediated in an effort to reduce its hazard and subsequently was extensively studied in the field prior to its remediation (Richardson and Reynolds, 2000).

Dig Tsho ( $86^{\circ}35.1'$  E,  $27^{\circ}52.5'$  N, 4365.9 m.a.s.l.) has been extensively studied and used as a site to assess and improve GLOF models (Cenderelli and Wohl, 2001; Bajracharya et al., 2007; Westoby et al., 2014; Westoby et al., 2015; Watson et al., 2015). Chamlang South Tsho ( $86^{\circ}57.5'$  E,  $27^{\circ}45.3'$  N, 4951.8 m.a.s.l.) and Chamlang North Tsho ( $86^{\circ}57.3'$  E,  $27^{\circ}47.0'$  N, 5218.0 m.a.s.l.) were both investigated in the field by Byers et al. (2013), which also included the modeling a GLOF from Chamlang North Tsho. Chamlang South Tsho has since been further investigated using high resolution digital elevation models (DEMs) and a bathymetric survey (Sawagaki et al., 2012; Lamsal et al., 2016). A field investigation was performed at Lower Barun Tsho ( $87^{\circ}05.7'$  E,  $27^{\circ}47.9'$  N, 4534.5 m.a.s.l.) in 1993 in connection to potential hydropower systems downstream (Mool et al., 2001), but has received little attention since with the exception of a visual field assessment of the terminal moraine and potential triggers (Byers, 2014). Similarly, Lumding Tsho ( $86^{\circ}36.8'$  E,  $27^{\circ}46.8'$  N, 4819.3 m.a.s.l.) has received little attention beyond documenting its growth (Bajracharya and Mool, 2009) despite being identified as a high priority glacial lake (ICIMOD, 2011). This study addresses this data gap and shows how a new method and framework may be used to prioritize future glacial lake investigations and management actions.

## **5.4 EXISTING METHODS**

### **5.4.1 Summary**

The first method that was used to assess the hazard of these eight glacial lakes was a “shotgun approach” to determine how their classifications vary using previous qualitative and quantitative assessment methods. The shotgun approach uses the same studies as Emmer and Vilimek (2013) with the exception of Clague and Evans (2000) and Grabs and Hanisch (1993) as these required site specific knowledge that was not possible to obtain from remote sensing. The use of solely remotely sensed data is one of the main goals of the new method and framework developed in this study. The qualitative methods used were O’Connor et al. (2001), Costa and Schuster (1988), and Wang et al. (2008). Wang et al. (2008) highlights ten hazard parameters, but only gives thresholds for eight of them; therefore, the eight parameters with thresholds are used for this qualitative approach. As a specific hazard rating is unable to be determined from these qualitative approaches, the arithmetic mean of the three is used to rank the glacial lakes.

The semi-quantitative method used in the shotgun approach was from Bolch et al. (2011), which was developed for glacial lakes in the Tien Shan using remotely sensed data. Bolch et al. (2011) uses a term called lake area change based on a comparison of lake area to its initial area; however, the initial area of a lake is unclear as they were all small melt ponds at one point in time. Therefore, the lake area change was simplified to give a value of 1 or 0 based on if the lake has grown in the last decade or not, respectively. The quantitative approach of Wang et al. (2011) also used only remotely sensed data with specific thresholds determined from a statistical analysis of 78 lakes in the southeastern Tibetan Plateau. Wang et al. (2011) uses the mean slope of the moraine based on a 100 m buffer around the lake; however, when this was applied to the glacial lakes in this study the mean slope was zero or negative indicating that within the first 100

m of the lake the moraine is higher than the lake level. Therefore, the steep lakefront area (SLA) from Fujita et al. (2013) was used as a surrogate for the mean slope of moraine so the method could still be applied and account for the slope of the moraine. A more detailed description of these studies may be found in Emmer and Vilímek (2013). Additionally, a new quantitative approach developed by Emmer and Vilímek (2014) for the Cordillera Blanca was used in this study. The approach assesses five GLOF scenarios: (1) moraine overtopping due to mass movement entering the lake, (2) overtopping from a flood upstream, (3) moraine failure due to mass movement entering the lake, (4) moraine failure from a flood upstream, and (5) failure resulting from a strong earthquake. Unfortunately, the locations of seepage points required for the last scenario were not identifiable from remote sensing, so the dam instability due to piping was not accounted for.

#### **5.4.2 Application of existing methods**

The qualitative hazard assessments show a good deal of variation between the three approaches (Table 1). The arithmetic mean reveals the most dangerous lakes based on these three qualitative approaches are Chamlang North Tsho, Chamlang South Tsho, and Tsho Rolpa, closely followed by the others with the exception of Imja Tsho and Thulagi Tsho. Imja Tsho has a lower value since these methods all use some form of mass movement entering the lake, which currently is not a threat at Imja Tsho. Thulagi Tsho is also not susceptible to ice avalanches and by some methods has a more stable moraine due to the presence of vegetation. The semi-quantitative and quantitative assessments give very different classifications of the hazard associated with each lake (Table 2). Bolch et al. (2011) emphasizes the size of the lake and its ability to expand, so all the large glacial lakes that have expanded over the last decade are ranked as high

danger (Imja Tsho, Lower Barun Tsho, Lumding Tsho, Thulagi Tsho, and Tsho Rolpa). The other glacial lakes that have already reached their maximum extent are classified as medium danger. Wang et al. (2011) is the complete opposite since the glacial lakes that have already reached their maximum extent are all high risk or very high risk, while the others are medium or low risk. This conflicting classification is due to the emphasis on parameters associated with mass movement entering the lake, i.e., both the distance and the slope between the lake and the glacier. The large glacial lakes that are still expanding have gentle slopes behind their calving fronts, which cause them to be classified as medium or low.

Table 5.1: Previous qualitative hazard assessments applied to eight glacial lakes in Nepal. Fractions are the amount of hazard parameters identified out of the total number of parameters used by each model. Details shown in Tables 5.7 – 5.9.

<b>Lake</b>	O'Connor et al. (2001)	Costa and Schuster (1988)	Wang et al. (2008)	Arithmetic Mean
Chamlang North Tsho	2/2	3/4	6/8	0.83
Chamlang South Tsho	2/2	3/4	6/8	0.83
Dig Tsho	2/2	2/4	5/8	0.71
Imja Tsho	1/2	2/4	5/8	0.54
Lower Barun Tsho	2/2	3/4	5/8	0.79
Lumding Tsho	2/2	2/4	6/8	0.75
Thulagi Tsho	1/2	2/4	5/8	0.54
Tsho Rolpa	2/2	3/4	6/8	0.83

Table 5.2: Previous semi-quantitative and quantitative hazard assessments applied to eight glacial lakes in Nepal. Values and thresholds for classifications are specific to each study. Fractions are the amount of scenarios for each lake that are considered to be highly dangerous. Details shown in Tables 5.10 – 5.12.

<b>Lake</b>	<b>Semi-Quantitative</b>		<b>Quantitative</b>			
	Bolch et al. (2011a)		Wang et al. (2011)		Emmer and Vilímek (2014)	
Chamlang North Tsho	0.45	Medium	0.85	Very High	2/5	High
Chamlang South Tsho	0.57	Medium	0.84	Very High	1/5	High
Dig Tsho	0.41	Medium	0.72	High	2/5	High
Imja Tsho	0.63	High	0.49	Low	1/5	High
Lower Barun Tsho	0.89	High	0.51	Medium	3/5	High
Lumding Tsho	0.79	High	0.61	Medium	4/5	High
Thulagi Tsho	0.71	High	0.51	Medium	1/5	High
Tsho Rolpa	0.89	High	0.60	Medium	2/5	High

Emmer and Vilímek (2014) classify all the glacial lakes as highly dangerous as they are all susceptible to at least one GLOF scenario. Table 2 shows how many of the five scenarios are a potential threat to each glacial lake. The reason for this classification is that the parameters associated with the mass movement and overtopping scenario are dam freeboard and distance between the glacier and the lake. The eight lakes considered in this study all have outlet channels, so their freeboard by definition is zero. Furthermore, these eight glacial lakes are either in contact or within 600 m of their mother glaciers, which results in this methodology considering them all to be susceptible to this dynamic failure. As Emmer and Vilímek (2014) discussed, the method was developed for scenarios related to Cordillera Blanca such that the framework could be transferred to other regions, but the exact scenarios or parameters used may not be representative of the main threats to other regions. Nonetheless, the assessment yields valuable insight showing Lumding Tsho, Lower Barun Tsho, and Tsho Rolpa have the

greatest number of hazard scenarios due to the potential for a flood from a glacial lake upstream, which is important to consider.

The shotgun approach shows that the hazard classification of each glacial lake varies greatly depending upon the selected method, which makes classifying the hazard associated with a particular glacial lake difficult. Fortunately, the shotgun approach is useful as it highlights the most commonly used parameters in previous studies. Table 3 shows the most frequently used parameters are mass movement entering the lake, the moraine width-to-height ratio, the presence of buried ice in the moraine, and the distance between the lake and the glacier. These naturally reflect the most common causes of GLOFs, i.e., mass movement entering the lake and the self-destruction of the moraine due to hydrostatic pressure and/or the degradation of buried ice (Richardson and Reynolds, 2000; Wang et al., 2012; Emmer and Cochachin, 2013). Furthermore, many of the other parameters are simply alternative forms of estimating the potential cause of failure, e.g., glacier snout steepness or the distance between the lake and the glacier are surrogate ways to estimate if the lake is susceptible to an avalanche entering the lake. In this manner, the shotgun approach lends insight into the various parameters or methods that were used to estimate different triggering events. The variety of parameters and the frequency of their use highlight the parameters that are important to consider in addition to highlighting the importance of developing a holistic method that accounts for these various forms of failure.

Table 5.3: Most frequently used parameters associated with previous studies (adapted from Emmer and Vilimek, 2013).

<b>Hazard Parameter</b>	<b>Number of Studies</b>
<b><i>Stability of Moraine</i></b>	
Moraine width-to-height ratio	9
Buried ice in moraine	8
Piping/seepage through moraine	7
Dam freeboard	6
Dam Type	5
Steepness of moraine	5
<b><i>Potential Triggering Events</i></b>	
Mass movement into lake	11
Distance b/w lake and glacier	8
Glacier snout steepness	6
Seismic activity	3
Extreme temp/precip	3
<b><i>Downstream Impact</i></b>	
GLOF Model	6
Lake area and/or volume	5

## 5.5 NEW HAZARD AND RISK FRAMEWORK

The conflicting hazard classifications from the shotgun approach casts uncertainty on the hazard of each glacial lake that can be confusing and misleading to the stakeholders these studies are meant to assist. Furthermore, they cast uncertainty on which glacial lakes should receive more attention through field campaigns and/or detailed analyses and the specific parameters that should be focused on. This study develops a new hazard and risk assessment framework that is holistic, objective, reproducible, and initially relies solely on remotely sensed data. Specifically, this framework focuses on two forms of glacial lake failure: dynamic and self-destructive. The term “self-destructive” failure (Yamada, 1998) is used here to avoid any confusion with long term

failures resulting from dynamic causes and lake growth, i.e., as a lake grows its expansion may make it susceptible to mass movement entering the lake from areas that could not previously reach the lake. Figure 2 shows the seven parameters used in this study are potential mass movement entering the lake from (1) a snow/ice avalanche, (2) a rockfall, or (3) an upstream flood, (4) the future expansion of the glacial lake, the stability of the moraine based on (5) the hydrostatic pressure and (6) the presence of buried ice, and (7) the downstream impact. These parameters are all estimated using simplistic models and globally available data sets. The approach is referred to as a “remote” hazard assessment. The integration of site-specific field data, high resolution data sets, and more complex models to improve upon this remote assessment will be detailed in the discussion in conjunction with a brief description of the current state of knowledge for each glacial lake investigated.

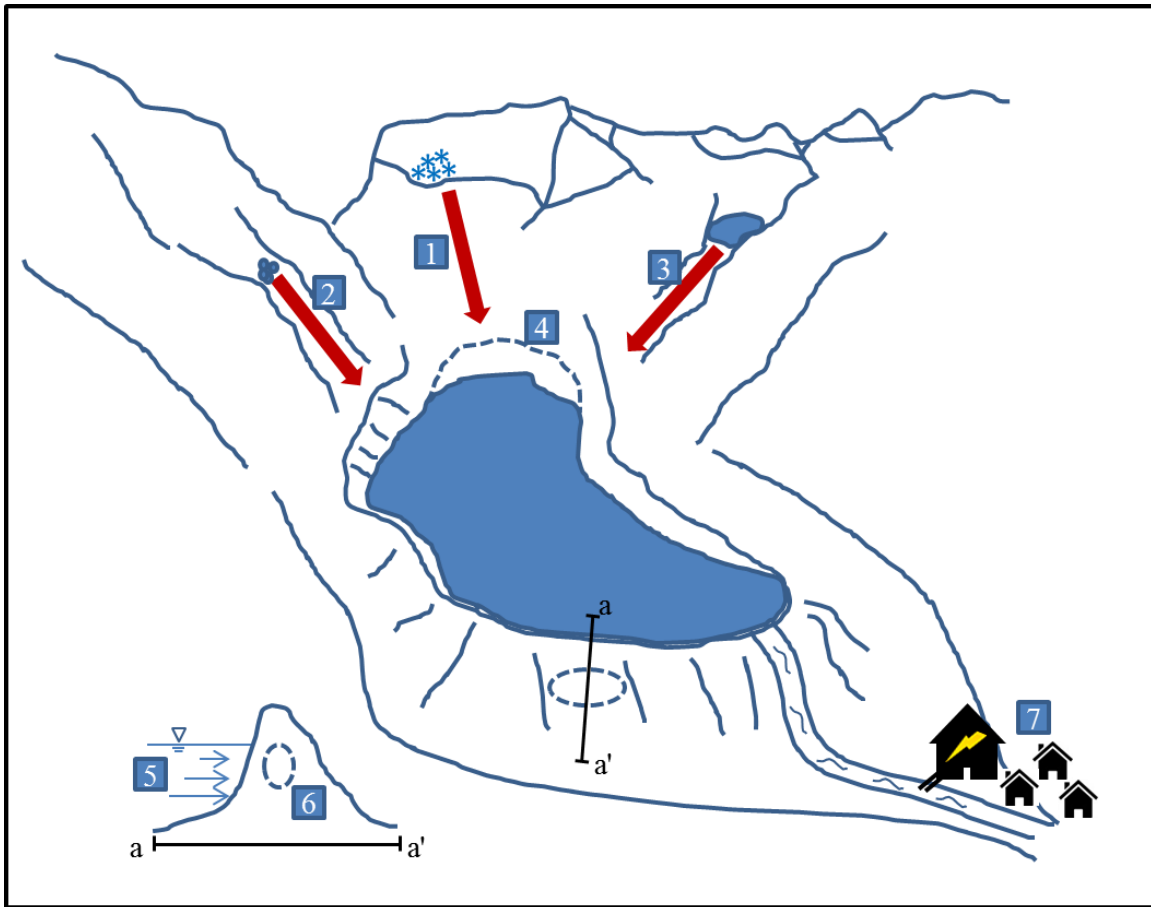


Figure 5.2: Schematic of GLOF hazard parameters used in new method: (1) snow/ice avalanche, (2) rockfall, (3) flood from upstream lake, (4) lake expansion, (5) hydrostatic pressure, (6) ice-cored moraine, and (7) downstream impact.

### 5.5.1 Remote hazard assessment

The remote hazard assessment framework is intended to be used as a launching point for assessing the hazards of glacial lakes. The parameters and models used in this framework are all derived from globally available data sets. The DEM utilized in this study is the ASTER GDEM, which is composed of automatically generated DEMs from the Advanced Spaceborne Emission and Reflection radiometer (ASTER) stereo scenes

acquired from 2000 to 2008. The ASTER GDEM V2 (hereon referred to as GDEM) has a horizontal resolution of 30 m and a vertical RMSE of  $\pm 15.1$  m for mountainous areas (ASTER GDEM Validation Team, 2011). The GDEM was used in this study instead of the SRTM V4 DEM (Farr et al., 2007) due to its higher resolution and its effect on the flood models is discussed in Section 4.1.4. Landsat imagery (Landsat 4/5 TM, Landsat 7 ETM+, and Landsat 8 OLI TIRS) was also used to delineate the glacial lakes and identify areas of snow, ice, and land. Landsat imagery was selected for this study as it is the highest resolution multi-spectral imagery that is ubiquitous.

#### ***5.5.1.1 Mass movement trajectories***

Mass movement entering a glacial lake is a highly hazardous situation for glacial lakes as the entry may cause a tsunami-like displacement wave that can trigger a GLOF. This study considers three types of dynamic failures: snow/ice avalanches, rockfalls, and upstream GLOFs (Figure 2). This section describes the mass movement trajectories for avalanches and rockfalls, while the upstream GLOFs are discussed later (Section 4.1.5). Landsat imagery was used to automatically detect glacierized and non-glacierized areas using a ratio of the NIR and SWIR 1 bands with a threshold of 2.2 (Huggel et al., 2004a). In this simplified model, there is no differentiation between snow and ice. Snow/ice avalanche prone areas were identified as any glacierized area with a slope greater than  $45^\circ$  (Alean, 1985; Bolch et al., 2008), but less than  $60^\circ$  as mass is unlikely to accumulate beyond this threshold (Osti et al., 2011; Shea et al., 2015). Rockfall prone areas were identified as any non-glacierized areas with a slope greater than  $30^\circ$  (Bolch et al., 2011) and less than  $60^\circ$  as well. The lateral moraines were precluded from being rockfall prone areas as they tend to be well developed and are unlikely to lose a large amount of material in one event. A single flow model using the flow direction algorithm in ArcGIS

10.3 in conjunction with a sink-free GDEM was used to model the path of the mass movement.

The runout distance of the mass movement trajectories was computed using an average slope threshold of 17° and 20° for avalanches and rockfalls, respectively. However, avalanches with a volume less than 6.67 million cubic meters had a higher average slope threshold based on a log relationship between avalanche volume and average trajectory slope (Huggel et al., 2004b)

$$\tan(\alpha) = 1.111 - 0.118 \log(V) \quad (5.1)$$

The avalanche volume was determined from estimates of avalanche-prone areas and assumed avalanche thickness. Avalanche-prone area was estimated using a variable kernel filter with a 90% threshold to determine the maximum avalanche-prone area with each pixel. The variable kernel filter begins with an individual pixel and determines if 90% of the surrounding pixels including itself, i.e., a 3 x 3 pixel grid, are avalanche-prone. If this condition is satisfied, then the kernel filter increases by one pixel, i.e., a 5 x 5 pixel grid, and continues this process until the 90% threshold fails. The estimated avalanche-prone area is considered to be the largest area that satisfies the 90% threshold. This study assumed three depths for avalanche thickness (10 m, 30 m, and 50 m) from avalanches previously reported in Russia (Huggel et al., 2005) and common estimates in the Swiss Alps (Huggel et al., 2004) due to a lack of avalanche depth data in the Himalaya. These three scenarios were used in conjunction with the avalanche-prone areas to estimate avalanche volume. The avalanche volumes ranged from  $2.7 \times 10^4 \text{ m}^3$  to  $6.7 \times 10^6 \text{ m}^3$ .

### ***5.5.1.2 Lake expansion***

Lake growth is crucial to incorporate into hazard assessments as the expansion of a glacial lake may greatly alter the lake's proximity to potential hazards and increase the volume of water likely released in a GLOF. Mass movement entering the lake is the most common cause of a GLOF, so one must determine if dynamic failure is both a current and/or future threat. Multi-spectral satellite imagery can be used to determine lake expansion rates semi-automatically using the normalized difference water index (NDWI) (McFeeters, 1996), which is a combination of the near-infrared (NIR) and blue bands. In the event that the blue band is not available or the contrast is not clear, the green (Bolch et al., 2008) and/or shortwave infrared (SWIR) bands (Somos-Valenzuela et al., 2014) may be used as a suitable alternative. Bolch et al. (2008) found the NDWI method yielded accurate estimates of lake area compared to manual delineations performed by Bajracharya et al. (2007).

One difficulty associated with the NDWI analysis is the objective selection of the threshold used to differentiate land and water. Bolch et al. (2011) found the threshold for Landsat images to range from 0.3 – 0.9 for glacial lakes in northern Tien Shan, but no clear instructions exist for selecting the threshold for each image and glacial lake. Thakuri et al. (2015) used the same technique at Imja Tsho and found the lake area to be constant between July and January each year. They suggested this was due to the lake level being constant, but measurements of lake level were not included. This study uses the same approach with Landsat imagery from 2000 to 2015 captured between September and January each year and assumes the width of the lake between the lateral moraines is constant based on the findings from Thakuri et al. (2015) and the assumption of a constant lake level. Two exceptions were made, one for Chamlang North Tsho, which used an image from May as there were less shadows during this time of year and another

for the supplementary image of Lower Barun Tsho in 2008, which used an image from the following April. Additionally, no clear sky, non-banded Landsat imagery was available in 2003, 2004, and 2008 for Lower Barun Tsho, so an Advanced Spaceborne Thermal Emission and Reflection Radiometer (ASTER) image between September and January was used for these years instead.

Thresholds were objectively selected such that the average width of the lake is constant between images. This method forces any changes in lake area to be the result of upglacier and/or downglacier expansion, which was the focus of this study. In the event that clouds or the Landsat 7 stripping caused portions of the lake to have gaps in the imagery, a second Landsat image was used to fill in these missing areas using the same criteria. Additionally, large debris-covered icebergs nearing the calving front that could cause pixels to be misclassified as land instead of water were manually corrected in post-processing.

The expansion rate was estimated as the average rate of areal expansion for all the 10 year intervals available, i.e., if yearly delineations were available from 2000 to 2015, then the six values of the 10 year expansion were averaged to estimate the areal expansion rate. These expansion rates were used in conjunction with ice thickness estimates to determine future lake extents. The ice thickness data used in this study is from the GlabTop2 model (Frey et al., 2014), which estimates the ice thickness from a DEM and glacier outlines. The ice thickness of the glaciers in this study was upwards of 250 m thick behind the calving front of some lakes. The bed topography of the glaciers was computed as the ice thickness subtracted from the surface elevation, which was used to identify potential overdeepenings, i.e., locations in the bed topography that are sinks and allow the lake to expand.

Future lake projections were estimated using the average areal expansion rates based on all 10 year intervals over the next 50 years such that the lake's risk to future dynamic failures could be assessed. Glacier flowlines were used to guide the direction of the expansion. The lake level was assumed to be constant over the next 50 years and was estimated as the average elevation of all the lake pixels based on the lake extent from 2000 as this elevation should be relatively constant over the time period when DEMs for the GDEM were being captured.

### ***5.5.1.3 Hydrostatic pressure***

The exact cause of failure associated with a moraine that spontaneously fails without any external influence is difficult to pinpoint, but is commonly referred to as “self-destruction” (Yamada, 1998; Emmer and Cochachin, 2013). One cause of self-destruction is when the hydrostatic pressure, the pressure a column of water exerts on the moraine, exceeds the structural capacity of the moraine. Many studies account for the moraine stability using a ratio of the moraine width-to-height (Table 2), which is subject to large errors if a global DEM is used (Fujita et al., 2008). Fujita et al. (2013) developed a surrogate parameter known as the steep lakefront area (SLA) using remotely sensed data that is not as susceptible to the uncertainty associated with global DEMs. The SLA is the average slope between the lake and any point within 1000 m of the moraine, which is similar in concept to the mean slope of the moraine based on a 100 m buffer that was used by Wang et al. (2011). The slope of any point within 1000 m of the moraine is meant to capture the steepest slope between the lake and the base of the terminal moraine. Fujita et al. (2013) examined moraines that had previously failed and determined that lakes with a SLA less than 10° were not susceptible to fail.

This study uses the SLA with a threshold of 10° to determine if the hydrostatic pressure may cause the moraine to self-destruct. NDWI delineations of the lake area are used to identify the pixels for the SLA calculation. The elevation of these lake pixels was set equal to the average elevation of the glacial lake from the GDEM based on the year 2000 delineation. Furthermore, the SLA was only computed for the main body of the lake, i.e., the SLA was not computed from melt ponds on the damming moraines of the lakes. Initial results of the SLA reported very high values of the SLA due to the elevation changes between adjacent pixels in the GDEM. These values are not representative of the slope of the moraine or the hydrostatic pressure on the moraine, so a 100 m buffer around the lake was used such that the SLA would be accurately captured.

#### ***5.5.1.4 Buried ice***

The other main cause of failure associated with “self-destruction” is the melting of ice within a lake’s terminal moraine since a disintegrating ice-core can undermine the structural integrity of the moraine (Richardson and Reynolds, 2000). This can have large implications for the hydrostatic pressure, piping/seepage, and reducing the height of the freeboard associated with the terminal moraine (Emmer and Cochachin, 2013). The importance of accounting for ice-cored moraines is apparent from previous studies (Table 2), but requires detailed information regarding the terminal moraine that is typically not available from remotely sensed data. Bolch et al. (2011) used permafrost as a surrogate parameter to suggest the potential of an ice-cored moraine. A similar approach was assessed in this study using permafrost maps (Gruber, 2012); however, a comparison between lakes with known ice cores and the permafrost maps revealed no correlation. McKillop and Clague (2007) assessed the presence of an ice core according to the shape of the moraine using aerial imagery by assuming that a moraine with a rounded surface

with arcuate ridges had an ice core, that a disproportionately large terminal moraine in front of a glacier was potentially ice-cored, and a narrow, sharp-crested moraine with an angular cross-section was ice-free. Unfortunately, this approach is highly subjective and appears to fail for glacial lakes with ice cores in Nepal. For example, Tsho Rolpa has a narrow terminal and lateral moraine that would suggest its moraine is ice free; however, it is known to have an ice core (Yamada, 1998; Richardson and Reynolds, 2000; ICIMOD, 2011).

In the field a common approach to determine if a moraine is ice-cored is by observing ice cliffs or karst topography (Yamada, 1998; Richardson and Reynolds, 2000; ICIMOD, 2011). Another common way is to witness changes in the outlet channel over time, which has been observed at Imja Tsho (Watanabe, 1994), Tsho Rolpa (Yamada, 1998), and Thulagi Tsho (ICIMOD, 2011). This study takes a similar approach using satellite imagery and Google Earth to identify the presence of any water on the moraine or any changes in the outlet. If water is present on the moraine or any changes in the outlet are observed, the moraine is assumed to have an ice core. During the analysis, a combination of Google Earth and satellite imagery was found to help differentiate between shadows and water, but it is recommended to err on the side of caution when one is unsure. Unfortunately, the lack of clear thresholds for identifying water on the moraine or changes in the outlet adds a small amount of subjectiveness to this study. However, as this was the most effective and least subjective approach for identifying the presence of buried ice in the moraine, it was used for the remote assessment.

#### ***5.5.1.5 GLOF modeling***

Flood models play a crucial role in a glacial lake hazard assessment as they identify areas at risk, which allows one to determine the downstream impact. Westoby et

al. (2014) provides a thorough overview of the various types of floods and types of models that may be used to reconstruct a GLOF. In short, if the flood entrains enough sediment from the moraine and channel downstream, the flood may transform into a debris flow, which increases the momentum of the flood thereby increasing the GLOF's extent and potential damage. The models used to reconstruct these debris flows or GLOFs range from simple computationally inexpensive GIS-based methods to computationally expensive, physically based numerical models. The GIS-based methods typically rely solely on the geometry of the downstream channel from a DEM. Numerical models have been used to resolve the flow of a GLOF in one or two dimensions. The benefit of two-dimensional models is their ability to capture more complex features and flow characteristics, e.g., multi-directional flows or super-elevation of flow around a channel bed (Westoby et al., 2014). The selection of a particular model or method typically depends on data availability and the desired model complexity.

This study explored the use of two computationally inexpensive flood models: the Modified Single Flow direction (MSF) model developed by Huggel et al. (2003) and the Monte Carlo Least Cost Path (MC-LCP) model developed by Watson et al. (2015). The MSF model is a standard flow direction model that “allows the flow to divert from the steepest descent direction up to 45° on both sides” (Huggel et al., 2003). The model requires a sink-filled DEM, a starting point in the form of a polygon, and a set threshold to stop the model based on the average angle between the starting point and the downstream flood. The MC-LCP model uses a Monte Carlo simulation to vary the DEM as a function of its uncertainty, while identifying the potential flow path for each simulation using a least cost analysis.

The lack of data related to previous GLOFs makes it difficult to assess the performance of different models. Watson et al. (2015) used the 1985 GLOF at Dig Tsho

to compare the performance of the MSF and MC-LCP models to the actual flood extents. These models used the GDEM resampled to 15 m and were found to perform reasonably well, although the MC-LCP model had a larger inundation area and fewer artefacts. Watson et al. (2015) also observed that in high relief Himalayan catchments, the requirements for an artificially filled DEM by the MSF model created large linear inundation artefacts, whereas the MC-LCP model displayed improved flow routing and hence is more appropriate for assessing first-order socio-economic impacts of a potential GLOF. It is important to note that the GDEM reflects the post-GLOF terrain, which was severely altered by the GLOF (Vuichard and Zimmermann, 1987). Ideally, a pre-GLOF DEM would be used for model validation so modeled flood extents would not be affected by scouring and deposition in the main channel. Furthermore, the comparison reveals multiple areas where the MC-LCP model does not capture the actual flood extent, which would be highly problematic for a hazard assessment if these areas were populated.

As both the MSF and MC-LCP models have no physical basis, model selection was determined by the one that yielded the most reasonable, conservative estimate of inundation areas when compared to a two-dimensional debris-flow model, FLO-2D, from Imja Tsho (Somos-Valenzuela et al., 2015). Figure 3 shows the flood extent for the FLO-2D, MSF, and MC-LCP models along with the performance of the MC-LCP model for various DEMs (GDEM and SRTM) and resolutions (resampled to 15 or 30 m). The comparison revealed the MSF model (Figure 3B) and the MC-LCP model resampled to a 15 m resolution for the SRTM DEM (Figure 3C) and the GDEM (Figure 3D) severely underestimated the flood extent. On the other hand, the MC-LCP model with the 90 m SRTM DEM yielded too conservative of an estimate (Figure 3G). The 30 m results for both the SRTM DEM (Figure 3E) and GDEM (Figure 3F) agreed well with the FLO2D results (Figure 3A); however, a more detailed analysis revealed the GDEM tracked the

main channel better. Therefore, the MC-LCP model with the 30m GDEM was used in this study to model the potential GLOFs from each lake. The GLOF from each lake was routed to the confluence of the Sun Kosi for seven of the eight glacial lakes, and approximately 60 km downstream for Thulagi Tsho based on the assumption that beyond this distance the downstream effects are minimal as the river is able to absorb the flood's energy (Vuichard and Zimmermann, 1987).

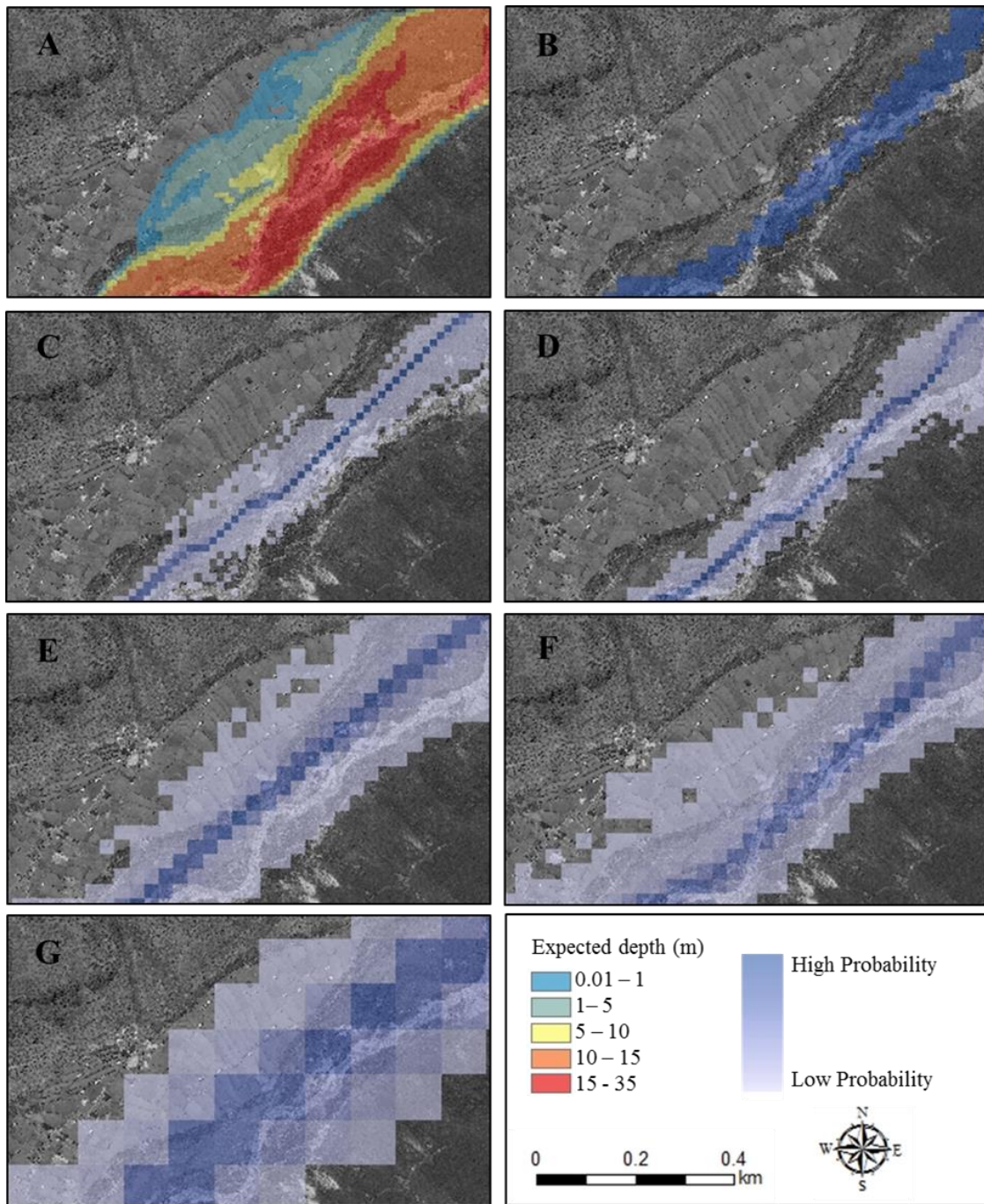


Figure 5.3: Inundated areas at Dingboche for a GLOF from Imja Tsho using (A) FLO2D (Somos-Valenzuela et al., 2015), (B) the MSF model using the GDEM, (C – G) the MC-LCP model with various DEMs and pixel sizes: (C) SRTM 90 m resampled 15 m, (D) GDEM 30 m resampled 15 m, (E) SRTM 90 m resampled 30 m, (F) GDEM 30 m, and (G) SRTM 90 m.

#### ***5.5.1.6 Downstream impact***

Buildings and agricultural land use data were extracted from the inundation extent of each MC-LCP GLOF scenario to provide a first-pass assessment of socio-economic implications. Buildings were downloaded from OpenStreetMap and validated in Google Earth, which also was used to add to the dataset where required using the most recent imagery. Areas of agricultural land were manually digitized in Google Earth and included all visibly managed land, i.e., land that appeared cleared, walled, farmed, or grazed, and would likely have detrimental socio-economic implications if flooded. The potential downstream impact was broken down into three classes: high, medium, and low. High impact is defined as the potential loss of life with no warning (lodges/buildings) and/or costly projects (e.g., hydropower). Medium impact is defined as any damage that is disruptive, which is meant to include damage to agricultural lands, bridges, trails, etc. Lastly, low impact is defined as having no impact on humans, infrastructure, or other projects. For the purpose of this study, buildings are assumed to have permanent occupants whose lives would be threatened in the event of a GLOF. Agricultural lands are considered to be a medium impact as their occupancy changes temporally depending on the season and in the event that people are in the fields they may be able to hear and/or see an upstream flood and have an opportunity to move to safe ground. The definition of costly projects or infrastructure is fairly subjective, but is meant to refer to any hydropower system or similar project since the loss of a mature hydropower system can affect multiple generations and jeopardize the economic development of the country (Richardson and Reynolds, 2000).

### **5.5.2 Risk classification and management actions**

The hazard elements described above are crucial for determining if a glacial lake is susceptible to a dynamic or a self-destructive failure. Figure 4 shows the workflow that is used to determine if the lake is susceptible to failure and how the cause of failures translates into the hazard associated with the lake. The most dangerous situation is a glacial lake that is susceptible to both dynamic and self-destructive failures, which would classify the lake as a very high hazard. Susceptibility is defined as a hazard greater than low, i.e., a lake that is considered a medium hazard for dynamic failure and medium hazard for self-destructive failure is still classified as very high hazard. The other scenario that classifies a lake as very high is a lake with a buried ice core that is susceptible to a snow/ice avalanche as the ice core may alter the height of the moraine over time and/or the erosion and breach of the moraine. A lake that is susceptible to avalanches, but does not have an ice core was classified as high hazard. Snow/ice avalanches were given the highest hazard classification since they are the most frequent cause of failure in the Himalaya (Emmer and Cochachin, 2013). Additionally, any lake with a buried ice core that is susceptible to a rockfall, upstream GLOF, or has a steep SLA is classified as high hazard. These hazard ratings are meant to reflect self-destructive failures being the second most common cause of GLOFs followed by mass movement entering the lake from rock or liquid water (Emmer and Cochachin, 2013). As temperatures continue to increase, thereby promoting the formation of more glacial lakes and altering slope stability due to changes in permafrost, there is a possibility that failures from rockfalls and/or upstream GLOFs may become more common as they are in Cordillera Blanca. A lake that does not have an ice core, but is susceptible to a rockfall, upstream GLOF, or has a steep SLA is considered to be medium hazard.

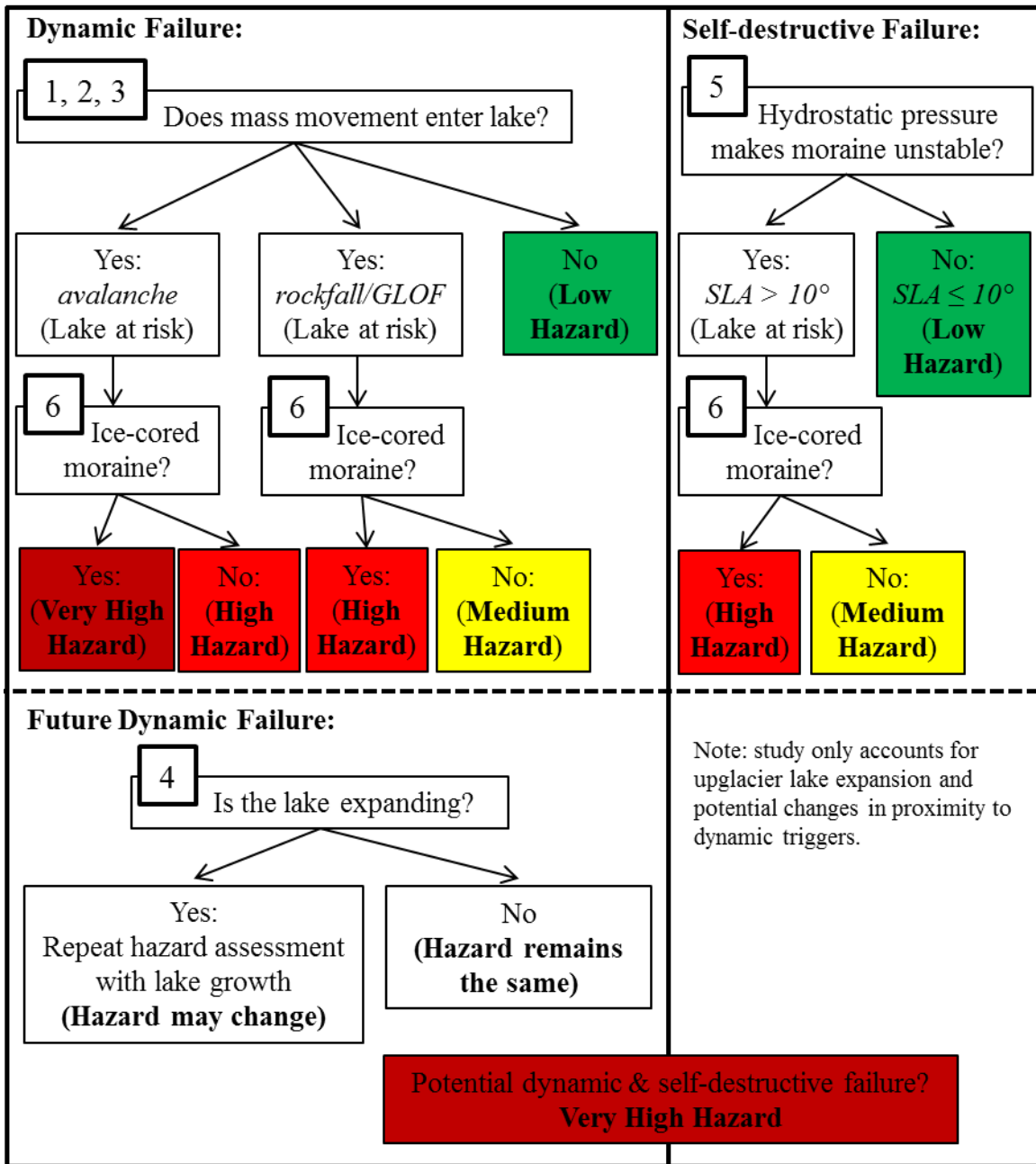


Figure 5.4: Hazard classification flow chart for determining the hazard associated with a glacial lake (numbers refer to hazard parameters in Figure 5.2).

The risk of a GLOF is a function of a glacial lake’s hazard and its potential downstream impact (Figure 5). Very high risk lakes are defined as any lake where the downstream impact is high, i.e., lives or costly projects are threatened, and the hazard of the lake is very high. High risk is defined as a lake that has a high downstream impact and a high hazard or a medium downstream impact with a high or very high hazard. Medium risk refers to lakes that have a high or medium downstream impact, but are only a medium hazard, or a lake that has a low downstream impact, but is a high or very high hazard. Lastly, low risk refers to the remaining lakes that are less of a threat to downstream communities and not a high hazard. It is important to note that any site that is at risk of a dynamic or self-destructive failure is valuable from an academic perspective as they may help improve the current state of knowledge of GLOF hazards.

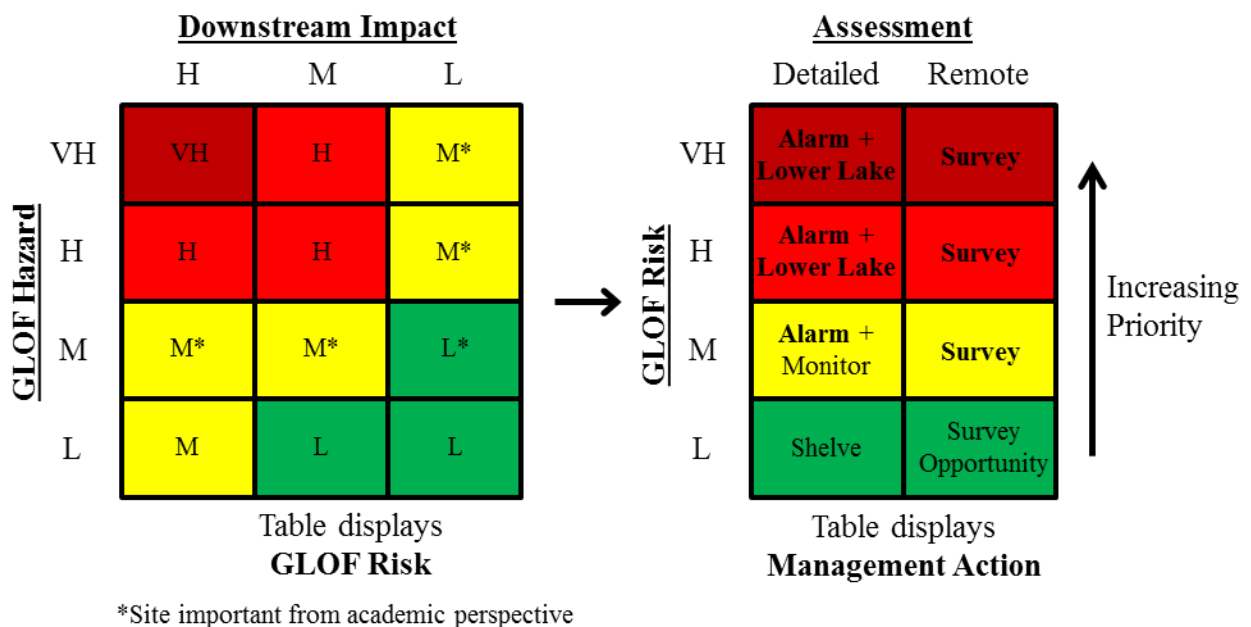


Figure 5.5: Risk and management action framework. Left table: GLOF risk is a function of the hazard and downstream impact. Right table: the recommended course of action for a given glacial lake based on the type of assessment.

## 5.6 RESULTS & DISCUSSION OF REMOTE HAZARD ASSESSMENT

The remote hazard assessment builds off of existing knowledge of glacial lakes in Nepal while integrating new approaches to develop a holistic understanding of their hazard and risks. The mass movement trajectories mark the first time these potential triggers have been modeled at a larger scale, which provides valuable information on the potential for mass to enter a lake in addition to identifying the locations of these avalanche and rockfall prone areas that should be further investigated. The stability of a moraine utilizes a previously developed approach, i.e., the SLA (Fujita et al., 2013), in combination with predictions of the presence of buried ice from satellite imagery such that self-destructive failures may be integrated into the hazard framework with the dynamic failures. Similarly, the downstream impacts use a previously developed GLOF model, i.e., MC-LCP approach (Watson et al., 2015), to obtain a conservative estimate of potentially inundated areas downstream. For three of the eight glacial lakes considered in this study, this is the first time their potential GLOFs have been modeled. Furthermore, this study combined lake expansion rates from satellite imagery with ice thickness estimates to model the evolution of these glacial lakes to determine how their hazard may vary over the next 50 years.

Table 4 provides a brief summary of the hazard parameters for each glacial lake. The potential for avalanches and rockfalls should not be surprising as these glacial lakes have developed on avalanche-fed debris-covered glaciers, so their surrounding slopes are commonly unstable. Three of the eight glacial lakes are threatened by a potential upstream GLOF, which makes it important to assess the hazards associated with these upstream lakes as well. The SLA varies between 4.9° at Lower Barun Tsho up to 18.8°

for Chamlang North Tsho. Buried ice is predicted to be present in the moraines of five of these lakes, but only two of these glacial lakes have a SLA above the 10° threshold thereby classifying these lakes as a high risk of self-destruction.

Table 5.4: Summary of the hazard parameters for the studied glacial lakes.

<b>Lake</b>	<b>Snow/ice avalanche</b>	<b>Rockfall</b>	<b>GLOF upstream</b>	<b>SLA (°)</b>	<b>Ice-cored moraine</b>	<b>Future change to hazards</b>
Chamlang North Tsho	Yes	Yes	No	18.8	No	-
Chamlang South Tsho	Yes	Yes	No	10.5	Yes <sup>1</sup>	-
Dig Tsho	Yes	Yes	No	8.9	No	-
Imja Tsho	No	No	No	6.8	Yes <sup>1,2</sup>	Yes (10-20 yrs)
Lower Barun Tsho	Yes	Yes	Yes	4.9	Yes <sup>1,2</sup>	Yes (10-20 yrs)
Lumding Tsho	Yes	Yes	Yes	10.3	No	Yes (10-20 yrs)
Thulagi Tsho	No	Yes	No	7.1	Yes <sup>1,2</sup>	No change
Tsho Rolpa	Yes	Yes	Yes	17.5	Yes <sup>2</sup>	No change

<sup>1</sup>ponds appear to be on the moraine; <sup>2</sup>changes in the outlet area identified

The hazard of these eight glacial lakes varies from low to very high with five of the eight lakes currently being very high hazard (Table 5). Four of the lakes classified as very high hazard are susceptible to both dynamic and self-destructive failures. Specifically, Chamlang South Tsho and Tsho Rolpa are both very high hazard for dynamic failure and high hazard for self-destructive failure. The MC-LCP GLOF modeling revealed potential to damage buildings and large swathes of agricultural lands for all eight glacial lakes, so the downstream impact was high for all the lakes. The amount of buildings, agricultural land, and bridges affected varied greatly, which was partly due to differences in the distance the GLOF was allowed to propagate downstream, but also due to the amount of development below each glacial lake. Therefore, the

inundated buildings per km<sup>2</sup> and percentage of agricultural land affected are beneficial for comparing the impacts of different glacial lakes. Tsho Rolpa had the highest amount of affected buildings (56.8 buildings km<sup>-2</sup>) and agricultural land (16.0%) followed closely behind by Thulagi Tsho (49.7 buildings km<sup>-2</sup> and 13.1%, respectively). Chamlang North Tsho, Chamlang South Tsho, and Lumding Tsho had the smallest amounts of inundated buildings and agricultural land affected; however, a GLOF from these lakes could potentially impact on the order of 200 buildings, 2.5 km<sup>2</sup> of agricultural land, and 15 bridges, which is still cause for considerable concern. Based on these hazard classifications and downstream impacts, the risk for each glacial lake ranged from medium to very high. These high and very high risk classifications should not be surprising as all the lakes investigated in this study (with the exception of Dig Tsho) were previously deemed hazardous or in need of further investigation (ICIMOD, 2011; Byers et al., 2013).

Table 5.5: Summary of hazard, downstream impact, and risk for each glacial lake.

Lake	Hazard			Downstream Impact	Overall Risk
	Dynamic	Self-Destructive	Overall		
Chamlang North Tsho	High	Medium	Very High	High	Very High
Chamlang South Tsho	Very High	High	Very High	High	Very High
Dig Tsho	High	Low	High	High	High
Imja Tsho	Low*	Low	Low	High	Medium*
Lower Barun Tsho	Very High	Low	Very High	High	Very High
Lumding Tsho	High	Medium	Very High	High	Very High
Thulagi Tsho	High	Low	High	High	High
Tsho Rolpa	Very High	High	Very High	High	Very High

\*Future hazard and risk is very high

Table 5.6: Details of downstream impacts from MC-LCP GLOF models for each glacial lake.

<b>Lake</b>	<b>Total Area (km<sup>2</sup>)</b>	<b>Buildings (total) (# km<sup>-2</sup>)</b>	<b>Agricultural Land</b>		<b>Bridges (total)</b>	<b>Hydropower Systems</b>	
			<b>(km<sup>2</sup>)</b>	<b>(%)</b>			
Chamlang North Tsho	28.2	244	8.7	2.5	8.8	14	-
Chamlang South Tsho	27.1	228	8.4	2.5	9.1	14	-
Dig Tsho	30.2	519	17.2	2.8	9.2	23	-
Imja Tsho	32.9	539	16.4	2.7	8.1	28	-
Lower Barun Tsho	45.8	640	14.0	5.9	12.8	20	Yes
Lumding Tsho	25.5	184	7.2	2.4	9.2	16	-
Thulagi Tsho	15.2	754	49.7	2.0	13.1	20	Yes
Tsho Rolpa	49.0	2787	56.8	7.8	16.0	35	-

Figure 6 shows that Lower Barun Tsho, Imja Tsho, and Lumding Tsho continue to expand rapidly, while Tsho Rolpa and Thulagi Tsho have stagnated in recent years. The other lakes (Chamlang North Tsho, Chamlang South Tsho, and Dig Tsho) have already detached from their glaciers and lack the ability to expand. These expansion estimates combined with the mass movement trajectories reveal that Imja Tsho is susceptible to a dynamic failure in the next 10 – 20 years (Table 4). These results have important implications on the hazard and risk associated with Imja Tsho as they indicate that in 10 – 20 years Imja Tsho may be a very high hazard and very high risk (Table 5). Additionally, the expansion of Lower Barun Tsho and Lumding Tsho makes them susceptible to potential avalanches located further upstream; however, this does not alter their hazard ratings as they are presently at risk as well.

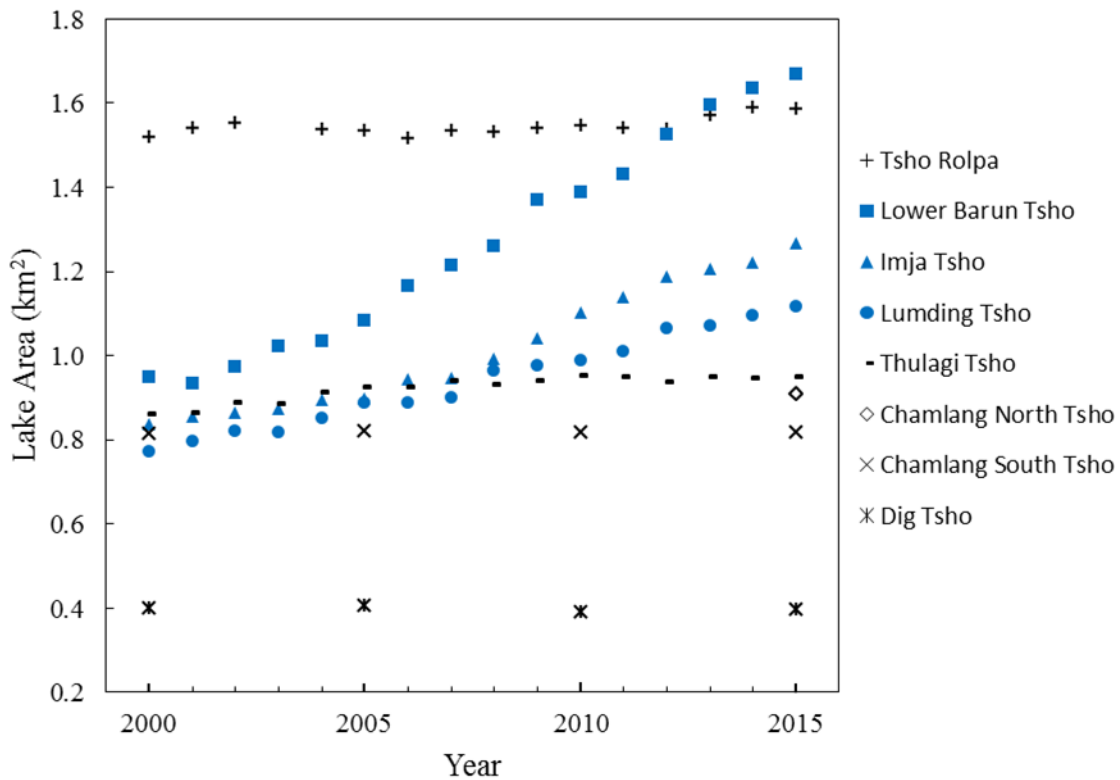


Figure 5.6: Area of glacial lakes derived from satellite imagery using the NDWI method from 2000 to 2015 (details in Table 5.13).

### 5.6.1 Imja Tsho

Imja Tsho is one of the most well studied glacial lakes in Nepal, yet the remote hazard assessment still yields new relevant insight. The mass movement trajectories (Figure 7A,B) show that the lake is currently not at risk of a dynamic failure. These trajectories are conservative estimates of avalanche and rockfall runout and for a worst-case scenario they remain at least 800 m and 400 m from the calving front, respectively. The ice thickness behind the calving front is greater than 200 m thick (Somos-Valenzuela et al., 2014; Frey et al., 2014), which allows the lake to continue to expand (Figure 7D). A detailed analysis of the growth of Imja Tsho (Figure 6) shows the lake is expanding at

an average rate of  $0.034 \pm 0.003 \text{ km}^2 \text{ yr}^{-1}$ . Based on these expansion rates and the ice thickness estimates, the lake may be at risk of a rockfall entering the lake in 10 years and an avalanche entering the lake in 20 years.

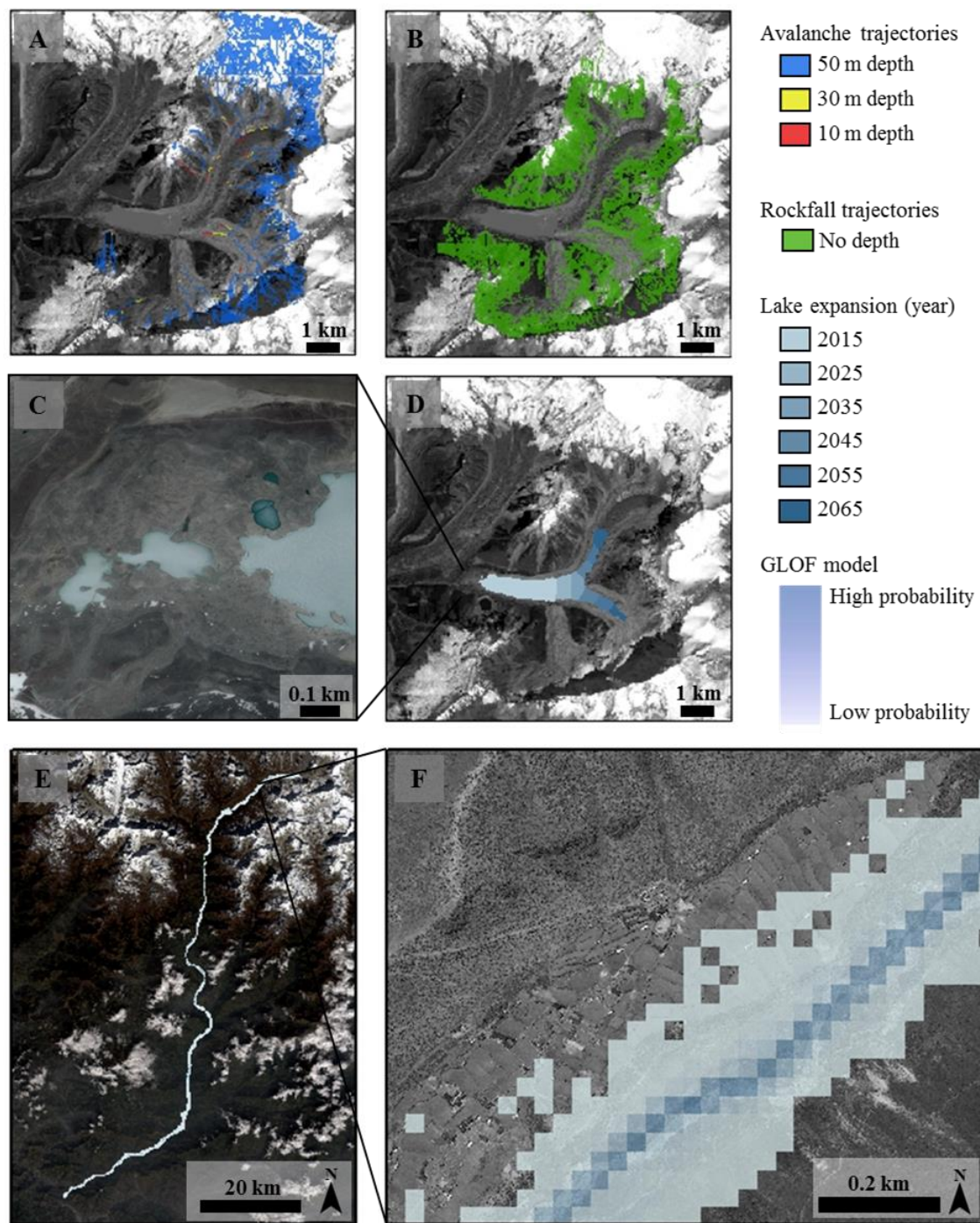


Figure 5.7: Hazards and downstream impact for Imja Tsho: (A) avalanche trajectories, (B) rockfall trajectories, (C) ponds on the moraine, (D) future lake expansion, and (E) the extent of the MC-LCP GLOF model (F) highlighting the impacts at Dingboche.

Fortunately, at the present moment the lake is unlikely to have a self-destructive failure as its SLA is fairly gentle at 6.8°. The melt ponds on the moraine (Figure 7C) suggest the presence of buried ice, which has been confirmed in the field (Hambrey et al., 2008). The ice-cored moraine is currently not a large concern as its gentle slope does not produce hydrostatic pressure that endangers the lake. However, satellite imagery reveals the outlet lakes have been changing rapidly, which is important to monitor as these changes may alter the hydrostatic pressure on the moraine (Fujita et al., 2013). If the outlet lakes on the terminal moraine are considered to be part of the lake, the SLA changes to 11.0° and Imja Tsho would currently be a high hazard and high risk. Therefore, monitoring the development of the outlet lakes and their influence on the hydrostatic pressure should be a top priority. The MC-LCP model (Figure 7E,F) shows that 539 buildings and 2.7 km<sup>2</sup> of agricultural land are at risk (Table 6), which corresponds to a high downstream impact.

Imja Tsho is currently classified as medium risk due to its low hazard and high downstream impact. These high downstream impacts highlight the importance of running hydrodynamic models with high resolution imagery to improve the mapping of inundated areas and inform the local communities (Somos-Valenzuela et al., 2014). The expansion model reveals that if Imja Tsho continues to grow at its current pace it will be a very high risk in the next 10 – 20 years. Since the expansion is highly concerning, one important area of future work should be measuring the ice thickness upglacier of Imja-Lhotse Shar Glacier using geophysical techniques such that the potential future extent of Imja Tsho may be accurately quantified. Additionally, efforts should focus on modeling the GLOF process chain, i.e., mass movement entering the lake, the wave propagation, the possible breach of the moraine due to the overtopping, and the downstream impacts

due to the future risk. The ice-cored moraine has already been well characterized (Hambrey et al., 2008), but is critical to avoid during any lake lowering activities such that a breach is not initiated. Furthermore, while self-destructive failure is not an immediate concern, repeat bathymetric studies on the outlet lakes would provide valuable information regarding the evolution of the moraine to understand how the hydrostatic pressures may change over time. Based on this remote assessment, the current risk mitigation actions to lower the level of the lake, ideally by 20 m (Somos-Valenzuela et al., 2015), are well justified and hopefully will serve as a good example of how to mitigate the risk of a glacial lake before it becomes highly hazardous.

### **5.6.2 Lumding Tsho**

Lumding Tsho was classified as a high priority for further investigation (ICIMOD, 2011), but has received very little attention beyond an analysis of its expansion (Bajracharya and Mool, 2009) and SLA (Fujita et al., 2013). The remote assessment confirms that Lumding Tsho is a very high hazard as it is susceptible to both dynamic and self-destructive failures. The mass movement trajectories reveal the lake is susceptible to avalanches and rockfalls from the southern side slope (Figure S5A,B). Furthermore, the lake is susceptible to a GLOF from Lumding Tsho Teng located 600 m upstream of Lumding Tsho. Lumding Tsho Teng (27°47.4' N, 86°37.3' E, 5141 m a.s.l.) has an area of 0.34 km<sup>2</sup> and is susceptible to a large avalanche from its northeastern slope in addition to potential rockfalls from its surrounding slopes. Lumding Teng Tsho also has a SLA of 31.7° indicating its moraine is highly unstable. These measurements on Lumding Teng Tsho indicate the lake is a very high hazard, so an upstream GLOF should be a great concern for Lumding Tsho.

Lumding Tsho also has a SLA ( $10.5^\circ$ ) that exceeds the stable threshold indicating the lake is susceptible to a self-destructive failure. Fortunately, the lack of ponds and apparently stable outlet channel on the terminal moraine indicate the moraine is unlikely to be ice-cored (Figure S5C). Detailed analysis of the growth of Lumding Tsho reveals the lake is growing at an average rate of  $0.023 \pm 0.002 \text{ km}^2 \text{ yr}^{-1}$  (Figure 6). The lake expansion model estimates the lake may continue to grow 500 m upglacier (Figure S5D), which would make it susceptible to large avalanches (assumed 50 m depth) from Lumding glacier that currently do not reach the lake. Therefore, the lake is likely to become more hazardous in the future as its proximity to more avalanche prone areas increases, but its hazard classification does not change as it was already classified as a very high hazard. The MC-LCP GLOF model (Figure S5E,F) reveals 184 buildings and  $2.0 \text{ km}^2$  of agricultural land are at risk (Table 6). This downstream impact is the smallest of those considered in this study, but still shows there is considerable risk to livelihoods downstream thereby classifying Lumding Tsho as very high risk.

An initial rapid reconnaissance was undertaken from 20 – 24 October 2015 to assess the hazards associated with Lumding Tsho as directed by the management action framework (Figure 5). The short field campaign consisted of a bathymetric study, streamflow measurements of the outlet, and visual inspection of the terminal moraine and surrounding slopes. The bathymetric survey was conducted over two days using an inflatable kayak and a Garmin echoMAP 54dv to measure 4768 points of lake depth. The shoreline was delineated using the NDWI methods as previously reported. The shoreline was converted into point measurements that were used in conjunction with the bathymetric survey to interpolate depth throughout the lake using the Topo to Raster tool in ArcGIS (Somos-Valenzuela et al., 2014). The lake was found to have an average

depth of 51 m, a maximum depth of 114 m, and a total volume of  $57.7 \times 10^6 \text{ m}^3$  (Figure 8).

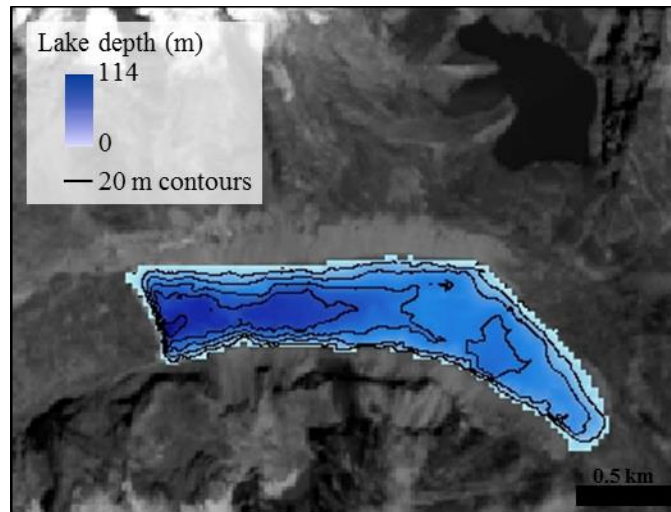


Figure 5.8: Bathymetric survey conducted on Lumding Tsho on 22-23 October 2015.

Streamflow from the outlet of the lake was measured to be  $8.4 \text{ m}^3 \text{ s}^{-1}$  in the afternoon of 23 October using a Pygmy Current Meter with an AquaCalc Pro Plus computer (Rickly Hydrological Company). Inspection of the terminal moraine revealed the outlet was the only source of water exiting the lake, i.e., there was no apparent seepage through the terminal moraine. Additionally, no ponds or karst-like features were present on the terminal moraine, which further indicated that the moraine was relatively stable. In contrast to the SLA, the terminal moraine appeared to be relatively gentle and fairly wide (Figure 9C). A detailed analysis of the SLA calculations reveals that 1 km downstream of Lumding Tsho is a large waterfall. If the distance from the lake used to compute the SLA was changed from 1 km to 950 m, then the SLA changes to  $9.8^\circ$ , which would change the hazard of a potential self-destructive failure from medium to low. The

waterfall is important to consider as this drop in elevation would generate a significant amount of energy that could exacerbate a GLOF downstream. Therefore, a physically-based flood model that can account for this acquisition of energy would be valuable for improving estimates of the potential downstream impacts.

Visual inspection of the side slopes revealed the slopes were very steep and likely lacked the ability to generate a large rockfall (Figure 9A,B). On the southern slope there was one large boulder that could be a potential concern (highlighted in Figure 9B), but its limited elevation above the lake level would likely cause only a small surge wave. The snow and ice above the southern side slopes was also very steep and no hanging glaciers were apparent. A more detailed assessment of the stability of the side slopes would be invaluable in improving the likelihood of a rockfall or avalanche. Specifically, the three hanging glaciers located behind the calving front (Figure 5.9A) are potential hazards as the lake grows. Physically-based mass movement models would generate important information regarding the size and trajectories of these slopes failures. Unfortunately, due to time constraints, a detailed analysis of Lumding Teng Tsho, the upstream glacial lake, was unable to be conducted. Similar knowledge of the stability of the slopes surrounding Lumding Teng Tsho would inform the likelihood of an upstream GLOF. A bathymetric study on Lumding Teng Tsho and an assessment of the stability of its moraine should also be a high priority. In the event of a GLOF, the northern lateral moraine of Lumding Tsho may protect the lake from the upstream flood. A physically-based GLOF model that accounts for erosion would yield insight into the potential breach of the lateral moraine and subsequent GLOF from Lumding Tsho. Based on the rapid field reconnaissance, the hazard associated with Lumding Tsho can be reduced from very high to high due to the apparent stability of the moraine. However, more detailed

analyses of slope stability around Lunding Tsho and Lunding Teng Tsho in addition to modeling the potential GLOFs from both of these lakes should be a top priority.

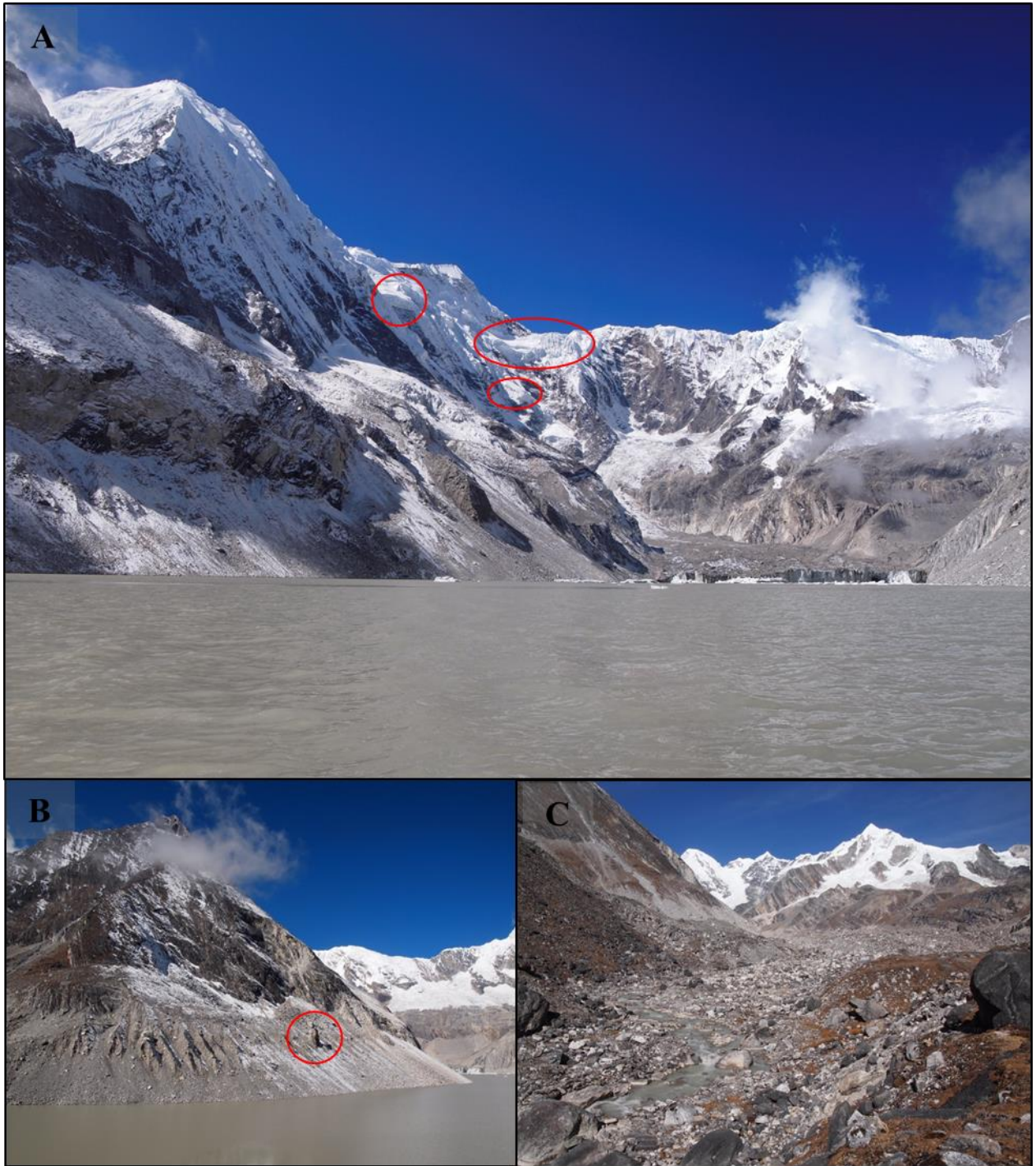


Figure 5.9: Luming Tsho and its surrounding slopes with areas of concern highlighted in red showing (A) the calving front and prone areas behind the glacier, (B) the southern side slope, and (C) the terminal moraine and its gentle outlet.

### 5.6.3 Chamlang North Tso

Chamlang North Tso has already reached its fullest extent, so its proximity to hazards is not going to change over time (Figure S1D). The southern and eastern slopes reveal the lake is very susceptible to rockfalls and avalanches to the extent that any rockfall or avalanche will enter the lake (Figure S1A,B). This potential for a dynamic failure is exacerbated by its steep terminal moraine, which has a SLA of 18.8°. This SLA is the highest among the eight glacial lakes investigated in this study and much greater than the stability threshold of 10°. Fortunately, no melt ponds were observed on the moraine and the outlet appears to be stable from satellite imagery indicating an ice-cored moraine is unlikely (Figure S1C). Nonetheless, the combination of the steep terminal moraine and the likelihood of mass movement entering the lake give Chamlang North Tso a classification of very high hazard. The MC-LCP GLOF model (Figure S1E,F) reveals that 244 buildings and 2.5 km<sup>2</sup> of agricultural land are at risk (Table 6) causing Chamlang North Tso to be a very high risk.

Based on the remote assessment, the most important area of future investigation should be modeling the GLOF process chain. The avalanche prone slopes were observed by Byers et al. (2013), who identified four overhanging glaciers on Chamlang North Tso's southern slopes. The use of high resolution imagery may help quantify the size of a potential avalanche. Byers et al. (2013) modeled a potential GLOF using the GDEM with the U.S. Army Corps of Engineers' Hydrologic Engineering Center River Analysis System (HEC-RAS). The ensuing flood model provides an improved estimate compared to the MC-LCP model, which estimates the water level will rise by 9 m at Bung; however, the downstream impacts were not detailed due to the lack of high resolution

imagery. The acquisition of high resolution DEMs for this region and/or cross sections at critical locations should be a high priority. This high resolution DEM should be used with two-dimensional flood models to more accurately estimate the downstream impacts. Additionally, a geotechnical survey including sedimentological sampling of the moraine should be performed such that erosion can be properly accounted for in breach scenarios (Westoby et al., 2015) and the stability of the moraine with respect to the current hydrostatic pressures may be quantified. Lastly, a bathymetric survey of Chamlang North Tsho is needed for the high resolution physically-based GLOF modeling.

#### **5.6.4 Chamlang South Tsho**

Chamlang South Tsho has very similar hazard characteristics to Chamlang North Tsho. Chamlang South Tsho is no longer expanding as it has already reached its fullest extent (Figure 6). Mass movement trajectories also show that the lake is surrounded by unstable slopes such that any rockfall or avalanche will enter the lake (Figure S2A,B). The SLA exceeds the stability threshold with a value of  $10.5^\circ$  indicating that the moraine is unstable. Additionally, satellite imagery reveals the presence of melt ponds on the moraine thereby suggesting the moraine is ice-cored (Figure S2C), which has been verified from the differencing of multi-temporal high resolution DEMs (Sawagaki et al., 2012; Lamsal et al., 2016). Therefore, the steep ice-cored moraine is considered to be a high risk to self-destruct. The combination of self-destructive failure and the potential for a dynamic failure classifies this glacial lake as a very high hazard. The MC-LCP GLOF model (Figure S2E,F) also reveals 228 buildings and  $2.5 \text{ km}^2$  of agricultural land are at risk (Table 6), so Chamlang South Tsho is considered to be a very high risk.

The remote assessment of mass movement entering the lake from the surrounding slopes was verified by field observations (Byers et al., 2013) and satellite imagery

(Lamsal et al., 2016). Sawagaki et al. (2012) also performed a bathymetric survey on the lake in 2009 and estimated the total volume to be  $35.6 \times 10^6 \text{ m}^3$ . These detailed field measurements and observations are highly valuable for verifying the remote assessment and furthering the current state of knowledge with regard to the lake; however, these observations have led to two drastically different conclusions from Byers et al. (2013) and Lamsal et al. (2016) regarding the danger of the lake. Byers et al. (2013) concluded the lake was safe from any dynamic failure based on the assumption that any mass movement-generated wave would be dampened and repelled by the length and surficial roughness of the terminal moraine. In direct contrast, Lamsal et al. (2016) stated a large surge wave could easily overtop the ice-cored moraine as it is only 4 – 18 m higher than the lake level, but no calculations were performed to support this assessment. Furthermore, Lamsal et al. (2016) measured the steep slope of the distal face of the terminal moraine, the low elevation of the toe of the terminal moraine, and observed seepage through the terminal moraine, which led them to conclude the lake was dangerous.

These conflicting studies, which had access to the same data and had similar on-site observations, highlight the need to take an objective approach towards understanding the risks associated with a glacial lake. The main priority with respect to Chamlang South Tsho should be modeling the entire GLOF process chain. This objective analysis would clarify the conflicting views on the potential for a dynamic failure. As a first-pass approach, the methods used by Heller and Hager (2009) were applied to estimate the impulse wave height using one of the avalanche volumes and tracks from the mass movement modeling. The modeled avalanche was  $8.1 \times 10^4 \text{ m}^3$  (assumed 10 m thickness) located 800 m east of Chamlang South Tsho at an elevation of 5650 m a.s.l. The avalanche density was assumed to be  $500 \text{ kg m}^3$  and the avalanche was assumed to

expand from its initial width of 90 m to the width of the lake at the location where the avalanche enters the lake (300 m). Based on these assumptions, the avalanche would generate a 20.5 m wave, which would likely easily overtop the ice-cored moraine. This simplified approach highlights the importance of using high resolution satellite imagery to determine the potential sizes of avalanches in conjunction with physically-based models to more accurately model the avalanche, the wave propagation, and any potential overtopping and/or breaching that may occur.

Additionally, the potential for a self-destructive failure needs to be explored in further detail as the remote assessment suggests the lake is unstable, which is supported by the SLA calculations in Fujita et al. (2013) and the observations and measurements from Lamsal et al. (2016). A chemical analysis of the seepage would lend insight as to the source of the water, i.e., whether the water is the melting of the ice core or lake water. Geophysical surveys of the terminal moraine should be used to determine the spatial extent and depth of the ice core and geotechnical surveys of the composition of the debris would be valuable for assessing the stability of the moraine in detail. Lastly, Lamsal et al. (2016) highlighted the potential downstream impact and Byers et al. (2013) noted that a GLOF from Chamlang South Tsho is a concern for these communities, so improved modeling using a physically-based GLOF model should be a top priority. The combination of these modeling efforts and field measurements would definitively determine the hazard of the lake and the threat to downstream communities.

#### **5.6.5 Dig Tsho**

Dig Tsho is a prime example of why glacial lakes should not be prioritized based on the size of the lake. In 1985, Dig Tsho was only 0.5 km<sup>2</sup> with a maximum depth of 18 m, yet its GLOF had devastating impacts downstream (Vuichard and Zimmermann,

1987). The breach of its moraine reduced the lake to its present size of 0.4 km<sup>2</sup> (Figure 6). The remote assessment shows that Dig Tsho is still very susceptible to another dynamic failure (Figure S3A,B) as any mass movement from the surrounding slopes is likely to enter the glacial lake. Fortunately, its previously breached moraine appears to be very stable as its SLA is 8.9° and an ice-core is unlikely (Figure S3C). Based on the potential for another dynamic failure, Dig Tsho is classified as a high hazard. The MC-LCP model (Figure S3E,F) shows that 519 buildings and 2.8 km<sup>2</sup> are at risk from a GLOF (Table 6), thereby classifying Dig Tsho as a high risk based on the remote assessment.

Field investigations should assess the current bathymetry of the lake to determine the amount of water that could be displaced by a GLOF. Most likely the maximum depth greatly diminished after the GLOF in conjunction with the reduction in the area of the lake, so the potential GLOF discharge would be smaller than the 1985 GLOF. A 1-D GLOF model that has been applied to other glacial lakes in Nepal (Byers et al., 2013; Khanal et al., 2015) would be beneficial in determining how the downstream impacts have changed based on the new bathymetry.

#### **5.6.6 Lower Barun Tsho**

Lower Barun Tsho has received little attention despite being considered one of the most dangerous glacial lakes in Nepal (ICIMOD, 2011). In this regard, the remote assessment yields valuable information regarding its hazards and can be used to guide future investigations of the lake. The mass movement trajectories show the lake is very susceptible to rockfalls and avalanches from its southern slope (Figure S4A,B). Figure 6 also reveals that Lower Barun Tsho has had the most rapid expansion rate of the eight lakes studied with an average growth of  $0.054 \pm 0.006 \text{ km}^2 \text{ yr}^{-1}$ . The expansion of Lower

Barun Tsho places it at further risk of avalanches and rockfalls located upglacier such that the lake will only be more susceptible to a dynamic failure in the future (Figure S4D). There also exists a smaller glacial lake located 4.5 km north of Lower Barun Tsho called Seto Pohkari (27°50' N, 87°5' E, 4842 m a.s.l.). The MC-LCP model of Seto Pohkari shows that Lower Barun Tsho is at risk of this potential upstream GLOF. Seto Pohkari has an area of 0.41 km<sup>2</sup> and is considered to be a high hazard as the avalanche and rockfall trajectories reveal the lake is susceptible to mass movement entering the lake from its surrounding slopes. Fortunately, the moraine of Seto Pohkari appears to be stable with no melt ponds and a gentle SLA of 4.0°. Similarly, Lower Barun Tsho has a gentle SLA of 4.9° indicating the lake is not susceptible to a self-destructive failure. However, satellite imagery reveals there are apparent ponds on the terminal moraine of Lower Barun Tsho (Figure S4C) and there appear to be changes in its outlet suggesting that Lower Barun Tsho likely has an ice cored moraine. The combination of the ice cored moraine and the lake's susceptibility to a dynamic failure classify the lake as a very high hazard. The MC-LCP model (Figure S4E,F) also reveals that in the event of a GLOF 640 buildings, 5.9 km<sup>2</sup> of agricultural land, and potential hydropower projects (WECS and NEA, 2015) would be at risk (Table 6). Therefore, Lower Barun Tsho is classified as a very high risk.

Similar to Lunding Tsho, Lower Barun Tsho should be a main priority of future field campaigns in Nepal as the lake is a very high risk, but has received little attention. Field campaigns should focus on investigating the potential of mass movement entering the lake from the southern slopes of Lower Barun Tsho. This investigation should be coordinated with physically-based modeling efforts of the GLOF process chain to determine how mass movement entering the lake will propagate across the lake and potentially breach the moraine. While the lake is unlikely to fail due to the hydrostatic

pressures, a sedimentological survey of the composition of the moraine would greatly improve modeling a potential breach. Geophysical techniques should also be performed on the moraine to determine the presence and spatial extent of the potential ice core as this may have large implications on the breach of the GLOF. The expansion of Lower Barun Tsho is a large concern as it only increases its susceptibility to rockfall and avalanche prone areas upglacier; therefore, geophysical techniques should be used on Barun Glacier to determine the maximum potential extent of the glacial lake. Additionally, bathymetric surveys should be performed on Lower Barun Tsho to aid modeling efforts of the GLOF process chain. Seto Pohkari also requires attention with regard to its bathymetry and modeling the process chain for avalanches and rockfalls from its surrounding slopes. Similar to Lumding Tsho, the northern lateral moraine of Lower Barun Tsho may protect the lake from the upstream GLOF. Therefore, a physically-based flood model for both Lower Barun Tsho and Seto Pohkari would greatly improve the understanding of the risk faced by downstream communities.

#### **5.6.7 Thulagi Tsho**

Thulagi Tsho is one of the three glacial lakes where field campaigns were performed to investigate the hazard of a GLOF by ICIMOD (2011). The results from the remote assessment yield valuable information that may be used to supplement these initial field campaigns. Mass movement trajectories reveal the lake is susceptible to rockfalls from both side slopes, but is not susceptible to avalanches (Figure S6A,B). Figure 6 shows that the lake growth has stalled since 2010. The lake expansion model reveals the bed elevation of the glacier behind the calving front is greater than the lake level indicating that the lake may have reached its maximum spatial extent (Figure S6D). An assessment of the terminal moraine shows there are ponds on the terminal moraine

and the outlet channel has changed in the last 15 years, which suggests the moraine is ice-cored. Fortunately, the SLA of 7.1° reveals the terminal moraine is apparently stable. This finding is in direct contrast to Fujita et al. (2013), which estimated a potential flood volume for Thulagi Tsho of 0.6 million m<sup>3</sup> indicating the SLA was greater than the 10° threshold. These differences are likely due to the 100 m buffer, the exclusion of the melt ponds, and/or potential differences in the lake delineations and DEMs used in this study. Based on this analysis, the lake is a high hazard due to the chance of a dynamic failure in conjunction with the ice-cored moraine. The MC-LCP GLOF model (Figure S6E,F) reveals 754 buildings, 2.0 km<sup>2</sup> of agricultural land, and planned hydropower projects (ICIMOD, 2011) are at risk (Table 6). These downstream impacts were among the most severe of the glacial lakes in this study as shown by the second highest buildings per km<sup>2</sup> and percentage of agricultural land. The combination of these high downstream impacts and high hazard classify Thulagi Tsho as a high risk.

As previously mentioned, the results of the remote assessment provide valuable information to supplement the work performed by ICIMOD (2011) and the one dimensional GLOF modeling performed by Khanal et al. (2015). Specifically, the lake expansion model shows that Thulagi Tsho appears to have reached its maximum extent, which should be confirmed with a geophysical survey measuring ice thickness behind the calving front. Additionally, the mass movement trajectories are the first time any slope stability has been modeled at this site. These trajectories reveal the lake's vulnerability to mass movement entering the lake and should be the focus of future modeling efforts at this lake. High resolution satellite imagery and field inspection should be used to determine the potential size of any rockfall such that these estimates may be applied to a physically-based mass movement model. These mass movement models could be used in conjunction with the bathymetric survey by ICIMOD (2011) to model the wave

propagation and breach of the moraine. A sedimentological survey to accompany the geophysical investigations performed by ICIMOD (2011) would allow the moraine stability and breach parameters to be quantified with greater accuracy. Furthermore, Khanal et al. (2015) also found the downstream impacts from a GLOF were very high; therefore, a two-dimensional physically-based model should build off these results to more accurately quantify the risks and vulnerable areas, which may be used to inform the downstream communities.

### **5.6.8 Tsho Rolpa**

Tsho Rolpa is arguably the most well-studied glacial lake in Nepal and currently the only glacial lake that has been remediated (Richardson and Reynolds, 2000). Richardson and Reynolds (2000) thoroughly discuss the hazards associated with the glacial lake. Nonetheless, the remote assessment yields valuable insight into the future development of the lake and potential vulnerabilities that may guide future work that should be performed on the lake. Similar to Thulagi Tsho, the lake expansion model shows that Tsho Rolpa appears to have reached its maximum extent (Figure S7D), which explains why the lake area has been relatively constant over the last decade. A geophysical survey behind the calving front would be beneficial to support this finding. If the model is correct, this has large implications on the hazard of the lake as this will limit the magnitude of future avalanches entering the lake, i.e., Richardson and Reynolds (2000) found that the magnitude of avalanches was increasing as the lake grew. The mass movement trajectories show that the lake is susceptible to avalanches from its northern slope (Figure S7A) and rockfalls from its surrounding side slopes (Figure S7B). The avalanche activity has been a major concern for Tsho Rolpa, so the logical next step is to use physically-based models to model the GLOF process chain and determine how

vulnerable the lake is to these threats. Satellite imagery from the last decade also reveals changes in the islands near the terminal moraine, which suggest the presence of an ice core (Figure S7C). The ice core has been confirmed and well documented (ICIMOD, 2011). Additionally, the SLA of 17.5° is the second highest of any of the glacial lakes in this study and Fujita et al. (2013) found Tsho Rolpa had the highest potential flood volume of the lakes in their study. The combination of the ice core, the high SLA, and the potential for mass movement to enter the lake confirm the previous assessments that Tsho Rolpa is a very high hazard.

Additionally, there are three glacial lakes located upstream that are threats to Tsho Rolpa. The first upstream glacial lake, Tsho Rolpa Upper 1 (27°50.7' N, 86°27.8' E, 4968 m a.s.l.), is located 1.5 km southeast of Tsho Rolpa and has an area of 0.12 km<sup>2</sup>. The hazard assessment reveals this upstream glacial lake is susceptible to ice avalanches, rockfalls, and has a SLA of 13.0°, thereby classifying Tsho Rolpa Upper 1 as a high hazard. The MC-LCP model reveals a GLOF has the potential to enter Tsho Rolpa; however, this would require the upstream GLOF to overtop and/or erode the southern lateral moraine of Tsho Rolpa. Similar to Lunding Tsho and Lower Barun Tsho, flood modeling that incorporates erosion would help determine if this lake is a credible threat to Tsho Rolpa. The second glacial lake located upstream of Tsho Rolpa, Tsho Rolpa Upper 2 (27°50.1' N, 86°29.0' E, 4858 m a.s.l.) has an area of 0.03 km<sup>2</sup> and is only susceptible to potential rockfalls. It also has a SLA of 10.1° thereby classifying the lake as a medium hazard. The third glacial lake, Tsho Rolpa Upper 3 (27°51.4' N, 86°30.0' E, 5316 m a.s.l.) has an area of 0.02 km<sup>2</sup> and is also only susceptible to potential rockfalls. This lake has a greater SLA of 20.2°, which also classifies it as a medium hazard. However, while Tsho Rolpa Upper 1 is much larger and appears to be a greater hazard than the other two upstream glacial lakes, the MC-LCP GLOFs reveal a GLOF from Tsho Rolpa Upper 2 or

3 would flow onto Trakarding Glacier and directly enter Tsho Rolpa. Therefore, the hazard associated with these glacial lakes should be further investigated.

The MC-LCP GLOF model of Tsho Rolpa (Figure S7E,F) shows that 2787 buildings, 7.8 km<sup>2</sup> of agricultural land, and 35 bridges would be at risk (Table 6). These impacts are both the highest number of buildings per km<sup>2</sup> affected and the highest percentage of agricultural land affected, which classified the risk associated with Tsho Rolpa as very high. Khanal et al. (2015) used a one-dimensional model, which confirmed the severe consequences downstream and highlights the importance of applying a two-dimensional model to create accurate hazard maps for the communities. This assessment is in agreement with other studies that Tsho Rolpa is still a high risk despite the fact that the lake was lowered by 3-4 m. Those risk-mitigation efforts serve as a good example that lowering the level of these lakes is possible, but also highlights the need to lower the lake 15 – 20 m further (Reynolds, 1999). A detailed analysis of the changes in the GLOF as a function of the lowered lake level would be a valuable resource to determine the exact amount the lake should be lowered.

## **5.7 CONCLUSIONS**

The remote assessment integrates the key hazard parameters in an objective manner that is repeatable and relies solely on globally available remotely sensed data. This study investigated eight glacial lakes in Nepal that are widely considered to be highly hazardous and was found to yield valuable insight with respect to each lake regardless of the amount of previous attention the lake had received. For Lumding Tsho and Lower Barun Tsho, this was the first time these lakes have been holistically studied since they were listed as a high priority of further investigation. For other glacial lakes that have already been studied extensively, e.g., Tsho Rolpa and Imja Tsho, the remote

assessment yielded valuable information regarding their future expansions. This study is the first of its kind to incorporate detailed modeling of lake growth into a hazard assessment. For Imja Tsho this is particularly valuable as the assessment is able to identify future hazardous conditions before they occur and hopefully shows the benefit of implementing risk-mitigation strategies prior to the lake becoming highly hazardous.

The remote assessment is meant to be a simple tool for understanding the hazards and is meant to guide the focus of future modeling efforts and field campaigns. The difficulty associated with conducting fieldwork in these areas and the scarcity of site-specific field data required to adequately model the risk at each site, as discussed in this study, highlights the need for coordinated efforts amongst institutions and local agencies to address these knowledge gaps. This collaborative effort is crucial when one considers the variety of expertise that is required to conduct these field campaigns and effectively model the GLOF scenarios. Furthermore, despite the methods in this study only being applied to eight glacial lakes, the framework was developed such that future work may apply the remote assessment to all the glacial lakes in Nepal. In this manner, a holistic and objective understanding of the current and future state of GLOF hazards may be developed.

## **5.8 ACKNOWLEDGEMENTS**

The authors acknowledge the support of the NSF-CNH program (Award #1516912), the USAID Climate Change Resilient Development (CCRD) project, and NASA Goddard Space and Flight Center / UMBC Maryland for the support of Rounce. We also acknowledge the support of Dr. Dhananjay Regmi of Himalayan Research Expeditions for logistical support during fieldwork. The Landsat imagery used in this study was provided by the Land Processes Distributed Active Archive Center (LP

DAAC). The base dataset of buildings used in this study is © OpenStreetMap contributors and is licensed under the Creative Commons Attribution-ShareALike 2.0 license.

## 5.9 SUPPLEMENTARY MATERIAL

Table 5.7: Results of O'Connor et al. (2001) hazard assessment.

Lake	Freeboard	Steep glacier calving	Total
Chamlang North Tsho	None	Yes	2/2
Chamlang South Tsho	None	Yes	2/2
Dig Tsho	None	Yes	2/2
Imja Tsho	None	No	1/2
Lower Barun Tsho	None	Yes	2/2
Lumding Tsho	None	Yes	2/2
Thulagi Tsho	None	No	1/2
Tsho Rolpa	None	Yes	2/2

Table 5.8: Results of Costa and Schuster (1988) hazard assessment.

Lake	Ice-cored moraine	Unstable young moraine, no vegetation	Steep slope moraine (> 40°)	Rock/ice avalanche into lake	Total
Chamlang North Tsho	No	Yes	Yes	Yes	3/4
Chamlang South Tsho	Yes	Yes	No	Yes	3/4
Dig Tsho	No	Yes	No	Yes	2/4
Imja Tsho	Yes	Yes	No	No	2/4
Lower Barun Tsho	Yes	Yes	No	Yes	3/4
Lumding Tsho	No	Yes	No	Yes	2/4
Thulagi Tsho	Yes	No	No	Yes	2/4
Tsho Rolpa	Yes	Yes	No	Yes	3/4

Table 5.9: Results of Wang et al. (2008) hazard assessment.

Lake	Top width of dam (< 600 m)	Distal flank steepness* (> 20°)	Ice-cored moraine	Dam width : height (< 2)	Slope of glacier snout (> 8°)	Temp & precip (hot & wet)	Freeboard : dam height (0)	Lake-glacier proximity (< 500 m)	Total
Chamlang North Tsho	530	41.5°	No	5.4	27.4°	Yes	0	0	6/8
Chamlang South Tsho	1050	39.7°	Yes	6.2	26.6°	Yes	0	270	6/8
Dig Tsho	460	30.1°	No	7	37.6°	Yes	0	960	5/8
Imja Tsho	650	31.7°	Yes	11.1	1.7°	Yes	0	0	5/8
Lower Barun Tsho	1000	26.7°	Yes	15	7.0°	Yes	0	0	5/8
Lumding Tsho	530	31.3°	No	13.7	12.4°	Yes	0	0	6/8
Thulagi Tsho	1000	28.1°	Yes	22.7	5.7°	Yes	0	0	5/8
Tsho Rolpa	530	39.2°	Yes	3.4	3.0°	Yes	0	0	6/8

\*maximum slope on terminal moraine was used

Table 5.10: Results of Bolch et al. (2011a) hazard assessment.

Lake	Lake area change	Risk of ice avalanche	Rick of rockfall	Ice core	Debris flow	Flash flood	Contact with glacier	Lake area (km <sup>2</sup> )	Glacier shrinkage	Glacier slope	Stagnant glacier	Hazard Score
Chamlang North Tsho	No	Yes	Yes	No	Yes	-	No	0.90	No	27.4°	No	Medium 0.45
Chamlang South Tsho	No	Yes	Yes	Yes	Yes	-	No	0.82	No	26.6°	Yes	Medium 0.57
Dig Tsho	No	Yes	Yes	No	No	Yes	No	0.40	No	37.6°	No	Medium 0.41
Imja Tsho	Yes	No	No	Yes	No	Yes	Yes	1.22	Yes	1.7°	Yes	High 0.63
Lower Barun Tsho	Yes	Yes	Yes	Yes	No	Yes	Yes	1.61	Yes	7.0°	Yes	High 0.89
Lumding Tsho	Yes	Yes	Yes	No	No	Yes	Yes	1.09	Yes	12.4°	Yes	High 0.79
Thulagi Tsho	Yes	No	Yes	Yes	No	Yes	Yes	0.95	Yes	5.7°	Yes	High 0.71
Tsho Rolpa	Yes	Yes	Yes	Yes	Yes	-	Yes	1.59	No	3.0°	Yes	High 0.89

Table 5.11: Results of Wang et al. (2011) hazard assessment.

Lake	Area of mother glacier (km <sup>2</sup> )	Distance between lake and glacier (m)	Slope between lake and glacier (°)	Slope of downstream face of dam (°)	Mother glacier snout steepness (°)	Hazard	Score
Chamlang South Tsho	7.5	270	45	10.4	26.6	Very High	0.84
Chamlang North Tsho	0.01	0	27.5	12.2	27.5	Very High	0.85
Dig Tsho	23.9	600	31.3	8.9	37.6	High	0.72
Imja Tsho	2.12	0	1.7	6.8	1.7	Low	0.49
Lower Barun Lake	55	0	7	4.9	7	Medium	0.51
Lumding Lake	29.1	0	12.4	10.5	12.4	Medium	0.61
Thulagi Tsho	56.8	0	5.7	7.1	5.7	Medium	0.51
Tsho Rolpa	61.5	0	3	16.4	3	Medium	0.6

Table 5.12: Results of Emmer and Vilimek (2014) hazard assessment.

	Chamlang North Tsho	Chamlang South Tsho	Dig Tsho	Imja Tsho	Lower Barun Tsho	Seto Pohkari	Lumding Tsho	Lumding Teng Tsho	Thulagi Tsho	Tsho Rolpa
<b>Terminal Moraine</b>										
Dam Type	moraine	moraine	moraine	moraine	moraine	moraine	moraine	moraine	moraine	moraine
Dam Freeboard (m)	0	0	0	0	0	0	0	0	0	0
Dam Width (m)	1770	1050	460	750	1000	900	490	475	1000	530
Dam Height (m)	330	169.8	66	69	66.6	50	32.3	200	44	165
Maximum slope of distal face of dam (°)	40	27.4	34.6	15	23.2	31.3	31.3	46.6	21.5	30
Remedial work	no	no	no	no	no	no	no	no	no	yes
<b>Lake Characteristics</b>										
Lake Area (m <sup>2</sup> )	9.1E+05	8.2E+05	4.0E+05	1.2E+06	1.6E+06	3.6E+05	1.1E+06	3.3E+05	8.8E+05	1.6E+06
Lake Perimeter (m)	6990	4920	3480	6540	8310	2850	7530	3260	7230	10140
Maximum lake width (m)	650	550	450	690	800	430	510	475	830	600
Lake Volume (m <sup>3</sup> )	3.7E+07	3.2E+07	1.2E+07	7.5E+07	8.1E+07	9.9E+06	4.7E+07	9.1E+06	3.5E+07	8.6E+07
<b>Lake Surrounding Characteristics</b>										
Distance b/w lake and glacier (m)	0	200	600	0	0	500	0	500	0	0
Width of calving front (m)	175	0	0		700	0	510	0	575	240
Mean slope b/w lake and glacier (°)	27.5	30.6	31.3	1.0	7.0	46.1	12.4	30.0	5.7	3.0
Mean slope of last 500m of glacier tongue (°)	27.5	26.6	31.3	1.0	7.0	18.8	12.4	20.0	5.7	3.0
Max slope of moraine surrounding lake (°)	74.5	73.2	67.8	54.5	70.1	57.8	66.0	56.3	68.8	57.0
Mean slope of lake surroundings (°)	34.0	45.0	45.0	37.5	45.0	35.0	35.0	30.0	45.0	45.0
<b>Results</b>										
Dam overtopping from mass movement into lake	1.00	0.96	0.93	1.00	1.00	0.85	1.00	0.83	1.00	1.00
Dam overtopping from upstream GLOF	0.00	0.00	0.00	0.00	0.85	0.00	0.83	0.00	0.00	0.00
Dam failure from mass movement into lake	0.64	0.46	0.57	0.21	0.39	0.52	0.52	0.73	0.37	0.50
Dam failure from upstream GLOF	0.00	0.00	0.00	0.00	1.00	0.00	0.83	0.00	0.00	0.00
Dam failure from strong earthquake	0.03	0.03	0.02	0.01	0.00	0.00	0.00	0.18	0.00	0.10
<b>Number of failures lake is susceptible to</b>	<b>2/5</b>	<b>1/5</b>	<b>2/5</b>	<b>1/5</b>	<b>3/5</b>	<b>2/5</b>	<b>4/5</b>	<b>2/5</b>	<b>1/5</b>	<b>2/5</b>

Table 5.13: Details concerning the satellite imagery, dates, bands, thresholds, and area (km<sup>2</sup>) for each glacial lake in this study.

Year	Date	Imagery (Bands)	Area (km <sup>2</sup> ) [Threshold]							
			Chamlang N. Tsho*	Chamlang S. Tsho	Dig Tsho	Inja Tsho	Barun Tsho	Lumding Tsho	Tsho Rolpa	Thulagi Tsho
2000	09/12	L7(1,4)	-	0.815 [0.68]	0.400 [0.55]	-	-	0.773 [0.64]	-	-
	09/26	L7(1,4)	-	-	-	-	-	-	-	0.860 [0.56]
	09/28	L7(2,4)	-	-	-	-	0.949 [0.43]	-	-	-
	10/14	L7(2,4)	-	-	-	0.835 [0.50]	-	-	-	-
	10/14	L7(1,4)	-	-	-	-	-	-	1.520 [0.43]	-
	10/30	L7(2,4)	-	-	-	-	Supp [0.25]	-	-	-
2001	09/15	L7(2,4)	-	-	-	0.853 [0.55]	0.932 [0.45]	-	-	-
	09/29	L7(1,4)	-	-	-	-	-	-	-	0.864 [0.56]
	10/07	L7(1,4)	-	-	-	-	-	0.797 [0.61]	1.541 [0.43]	-
2002	12/20	L7(2,4)	-	-	-	-	Supp [0.05]	-	-	-
	10/04	L7(2,4)	-	-	-	0.863 [0.35]	0.974 [0.23]	-	-	-
	10/04	L7(1,4)	-	-	-	-	-	0.821 [0.41]	1.553 [0.27]	-
	10/20	L7(2,4)	-	-	-	-	Supp [0.43]	-	-	-
2003	12/05	L7(1,4)	-	-	-	-	-	-	-	0.887 [0.35]
	10/23	A(1,3)	-	-	-	-	1.022 [0.00]	-	-	-
	11/08	L7(2,4)	-	-	-	0.871 [0.50]	-	-	-	-
	11/08	L7(1,4)	-	-	-	-	-	0.818 [0.64]	-	-
	11/14	L5(1,4)	-	-	-	-	-	-	-	0.885 [0.54]
2004	11/16	L7(1,4)	-	-	-	-	-	Supp [0.60]	-	-
	10/09	A(1,3)	-	-	-	-	1.035 [0.00]	-	-	-
	10/17	L5(1,4)	-	-	-	-	-	0.851 [0.62]	1.536 [0.44]	-
	11/10	L7(2,4)	-	-	-	0.893 [0.35]	-	-	-	-
	11/16	L5(1,4)	-	-	-	-	-	-	-	0.912 [0.51]
2005	10/10	L7(2,4)	-	-	0.406 [0.12]	-	1.082 [0.45]	-	-	-
	10/28	L7(2,4)	-	-	-	0.898 [0.10]	Supp [0.15]	0.887 [0.20]	-	-
	11/03	L5(1,4)	-	-	-	-	-	-	-	0.923 [0.48]
	11/05	L5(1,4)	-	0.822 [0.63]	-	-	-	Supp [0.34]	1.535 [0.41]	-
2006	09/05	L5(1,4)	-	-	-	-	-	0.888 [0.57]	1.517 [0.44]	-
	10/15	A(1,3)	-	-	-	-	1.165 [0.45]	-	-	-
	11/16	L7(4,5)	-	-	-	0.943 [0.35]	-	-	-	-
	11/22	L5(1,4)	-	-	-	-	-	-	-	0.925 [0.50]
	09/22	L5(1,4)	-	-	-	-	-	-	-	0.940 [0.48]
2007	10/02	L7(2,4)	-	-	-	0.947 [0.30]	-	-	-	-
	10/02	L7(1,4)	-	-	-	-	-	Supp [0.41]	Supp [0.25]	-
	10/18	L7(2,4)	-	-	-	-	1.213 [0.45]	-	-	-
	11/03	L7(2,4)	-	-	-	-	Supp [0.30]	-	-	-
	11/19	L7(1,4)	-	-	-	-	-	0.900 [0.48]	1.534 [0.25]	-
	10/12	L5(1,4)	-	-	-	-	-	0.965 [0.65]	1.532 [0.41]	-
2008	10/20	L7(2,4)	-	-	-	0.992 [0.30]	-	-	-	-
	10/26	L5(1,4)	-	-	-	-	-	-	-	0.932 [0.47]
	11/05	L7(2,4)	-	-	-	-	1.261 [0.45]	-	-	-
	04/30	L7(2,4)	-	-	-	-	Supp [0.45]	-	-	-
2009	09/27	L5(1,4)	-	-	-	-	-	-	-	0.941 [0.45]
	10/15	L5(2,4)	-	-	-	-	1.370 [0.15]	-	-	-
	10/15	L5(1,4)	-	-	-	-	-	0.977 [0.64]	1.541 [0.41]	-
	10/23	L7(2,4)	-	-	-	1.041 [0.30]	-	-	-	-

Table 5.13 (Continued)

2010	10/10	L7(1,4)	-	-	0.390 [0.54]	-	-	Supp [0.65]	Supp [0.36]	
	10/26	L7(2,4)	-	-	-	1.101 [0.30]	1.389 [0.30]	-	-	
	10/26	L7(1,4)	-	0.817 [0.48]	-	-	-	0.989 [0.54]	1.545 [0.29]	
	12/03	L5(1,4)	-	-	-	-	-	-	-	0.952 [0.43]
2011	01/14	L7(2,4)	-	-	-	-	Supp [0.05]	-	-	
	09/03	L5(1,4)	-	-	-	-	-	-	1.542 [0.43]	
	10/13	L7(2,4)	-	-	-	-	1.432 [0.35]	-	-	
	10/13	L7(1,4)	-	-	-	-	-	Supp [0.44]	-	
	10/19	L5(1,4)	-	-	-	-	-	-	-	0.950 [0.43]
	10/29	L7(2,4)	-	-	-	1.139 [0.30]	Supp [0.35]	-	-	
	10/29	L7(1,4)	-	-	-	-	-	1.001 [0.45]	-	
2012	09/27	L7(1,4)	-	-	-	-	-	-	-	Supp [0.28]
	09/29	L7(4,5)	-	-	-	1.187 [0.10]	-	-	-	
	09/29	L7(2,4)	-	-	-	-	1.525 [0.40]	-	Supp [0.18]	
	10/13	L7(1,4)	-	-	-	-	-	-	-	0.936 [0.28]
	10/31	L7(2,4)	-	-	-	-	Supp [0.40]	-	-	
	10/31	L7(1,4)	-	-	-	-	-	1.064 [0.44]	-	
	11/16	L7(1,4)	-	-	-	-	-	Supp [0.21]	1.538 [0.05]	
2013	10/08	L8(2,5)	-	-	-	-	-	-	-	0.950 [0.05]
	10/10	L8(3,5)	-	-	-	1.206 [0.10]	1.595 [0.10]	-	-	
	10/10	L8(2,5)	-	-	-	-	-	1.071 [0.22]	1.571 [0.08]	
2014	09/27	L8(3,5)	-	-	-	1.220 [0.15]	1.635 [0.08]	-	-	
	09/27	L8(2,5)	-	-	-	-	-	Supp [0.22]	-	
	10/11	L8(2,5)	-	-	-	-	-	-	-	0.947 [0.04]
	11/14	L8(2,5)	-	-	-	-	-	1.094 [0.18]	1.589 [0.05]	
2015	05/25	L8(2,5)	0.910 [0.05]	-	-	-	-	-	-	
	09/30	L8(2,5)	-	0.818 [0.21]	0.396 [0.14]	1.265 [0.15]	1.670 [0.08]	1.115 [0.20]	1.588 [0.06]	
	11/15	L8(2,5)	-	-	-	-	-	-	-	0.948 [0.04]

\*Required heavy manual editing to account for shadows

"Supp" stands for supplementary image used to fill in for clouds or stripping

"L5" stands for Landsat 5

"L7" stands for Landsat 7

"L8" stands for Landsat 8

"A" stands for ASTER

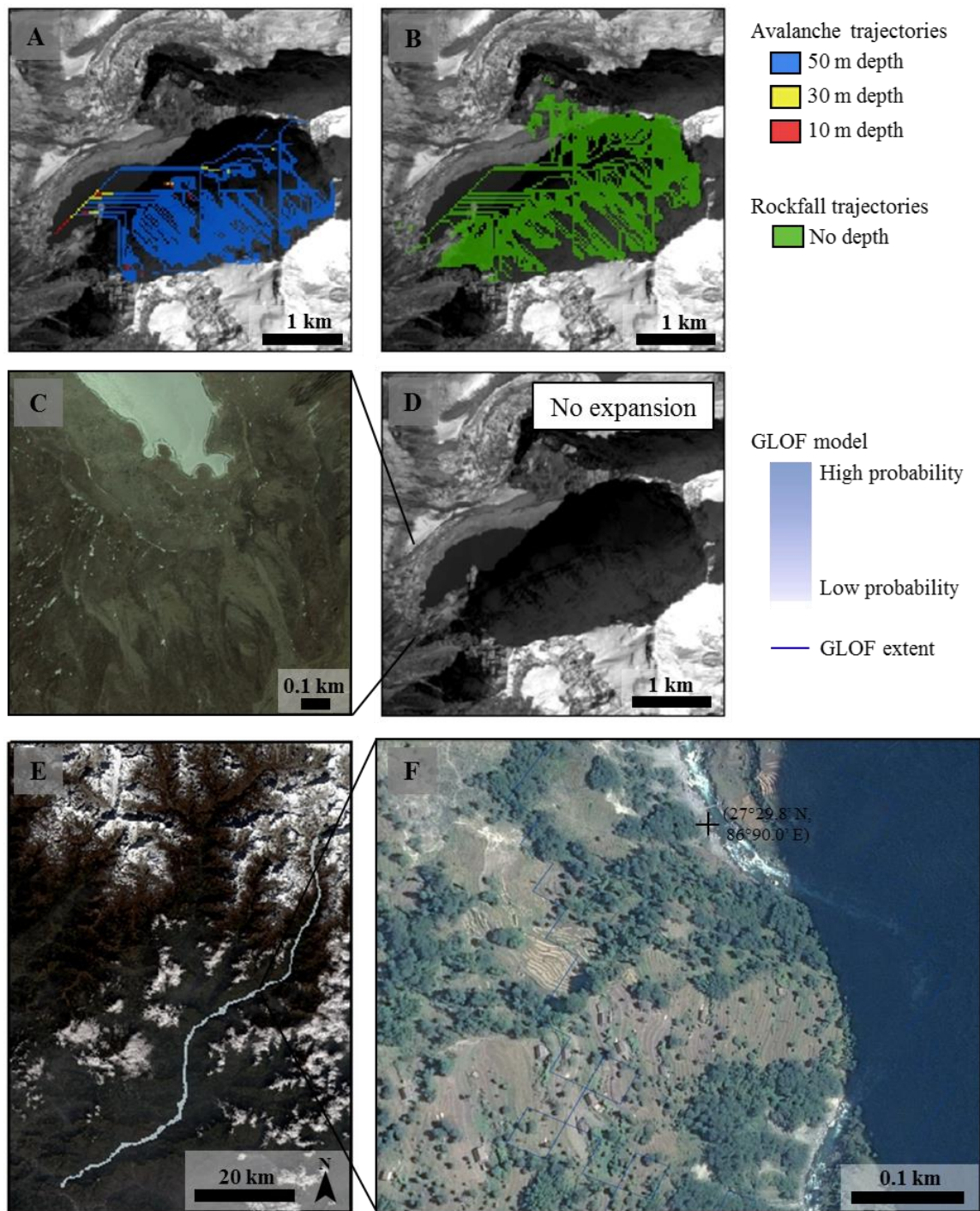


Figure 5.10: Hazards and downstream impact for Chamlang North Tsho: (A) avalanche trajectories, (B) rockfall trajectories, (C) lack of ponds on the moraine, (D) future lake expansion, and (E) the extent of the MC-LCP GLOF model (F) highlighting the impacts downstream.

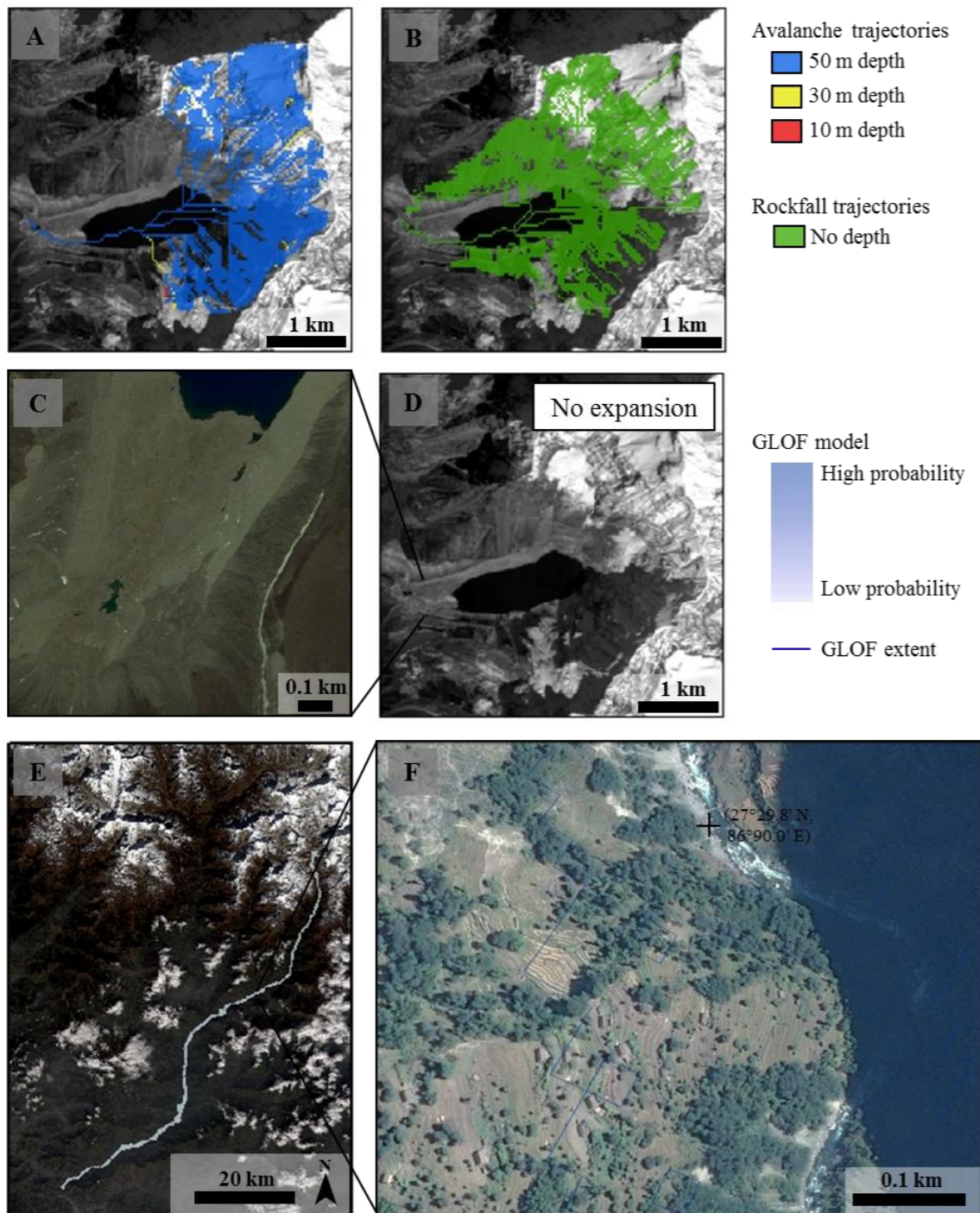


Figure 5.11: Hazards and downstream impact for Chamlang South Tsho: (A) avalanche trajectories, (B) rockfall trajectories, (C) ponds on the moraine, (D) future lake expansion, and (E) the extent of the MC-LCP GLOF model (F) highlighting the impacts downstream.

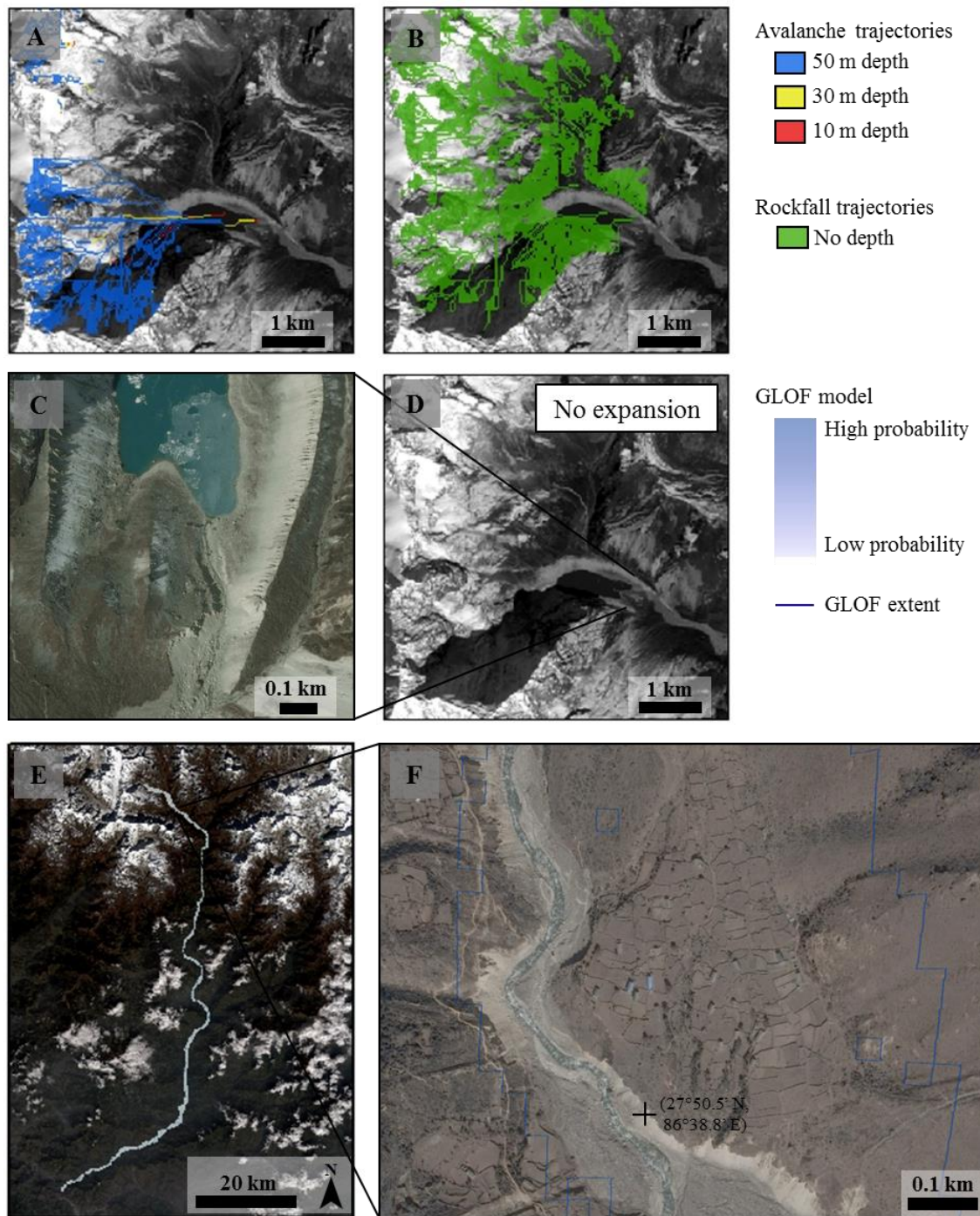


Figure 5.12: Hazards and downstream impact for Dig Tsho: (A) avalanche trajectories, (B) rockfall trajectories, (C) lack of ponds on the moraine, (D) future lake expansion, and (E) the extent of the MC-LCP GLOF model (F) highlighting the impacts downstream.

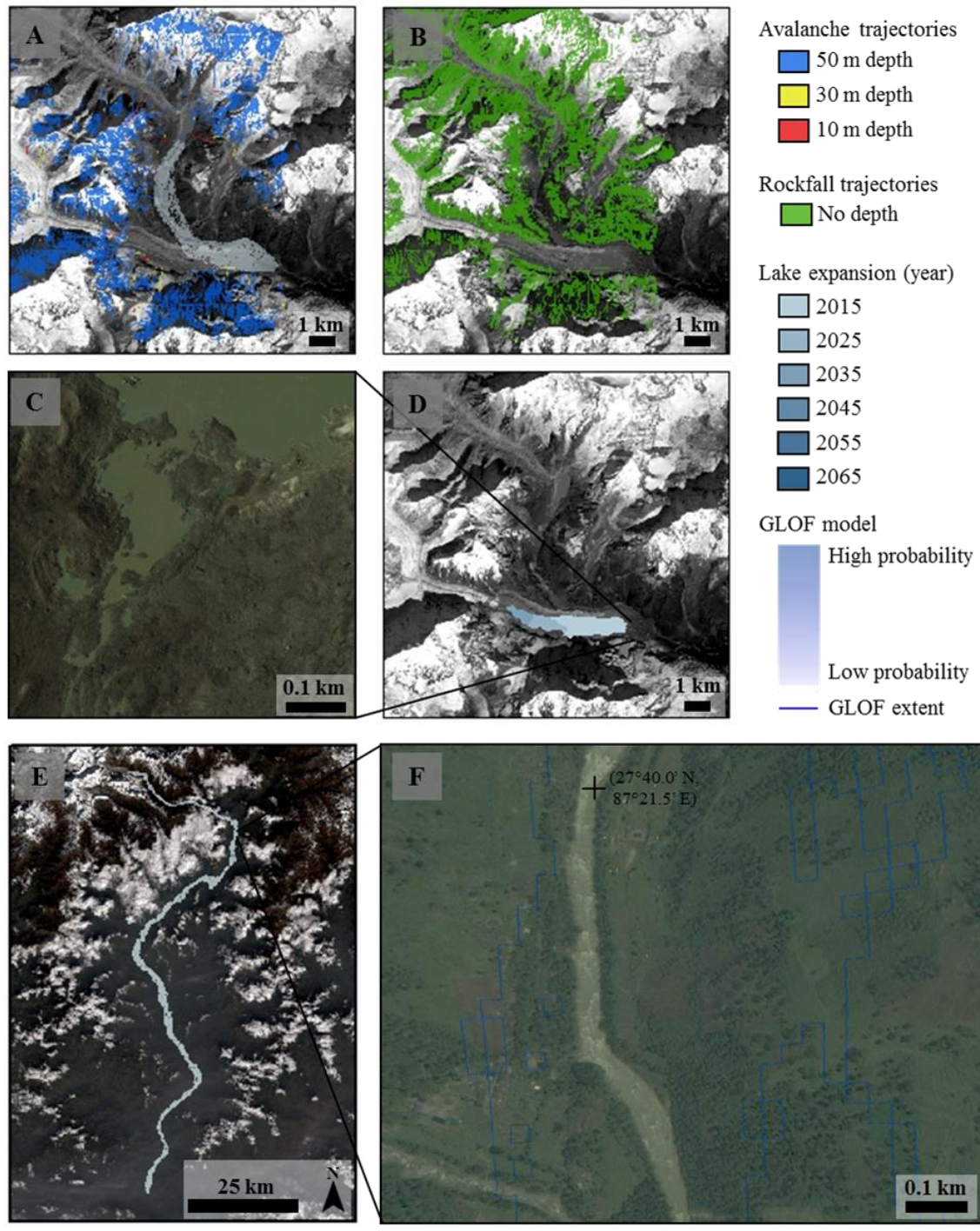


Figure 5.13: Hazards and downstream impact for Lower Barun Tsho: (A) avalanche trajectories, (B) rockfall trajectories, (C) ponds on the moraine, (D) future lake expansion, and (E) the extent of the MC-LCP GLOF model (F) highlighting the impacts downstream.

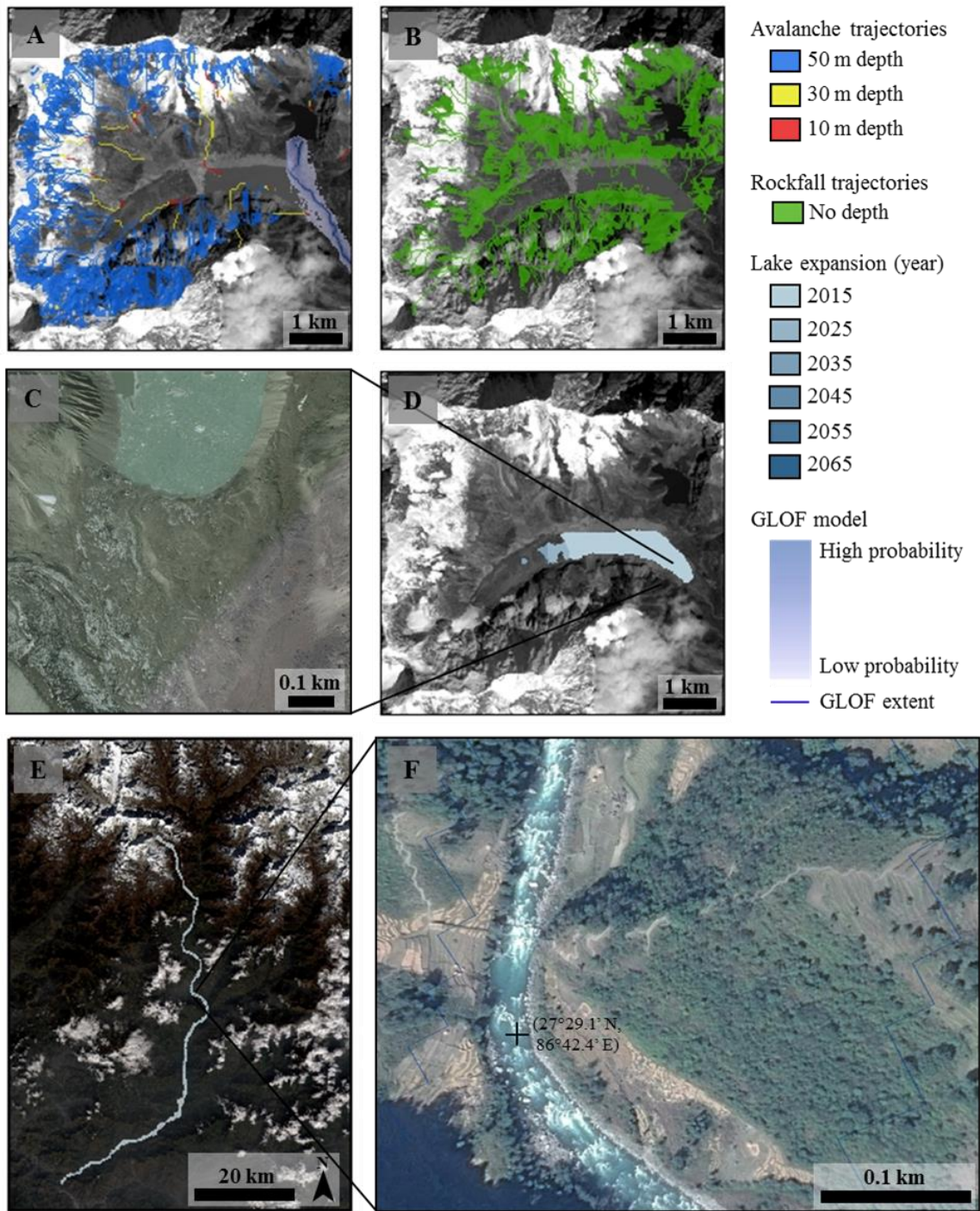


Figure 5.14: Hazards and downstream impact for Lumding Tsho: (A) avalanche trajectories, (B) rockfall trajectories, (C) lack of ponds on the moraine, (D) future lake expansion, and (E) the extent of the MC-LCP GLOF model (F) highlighting the impacts downstream.

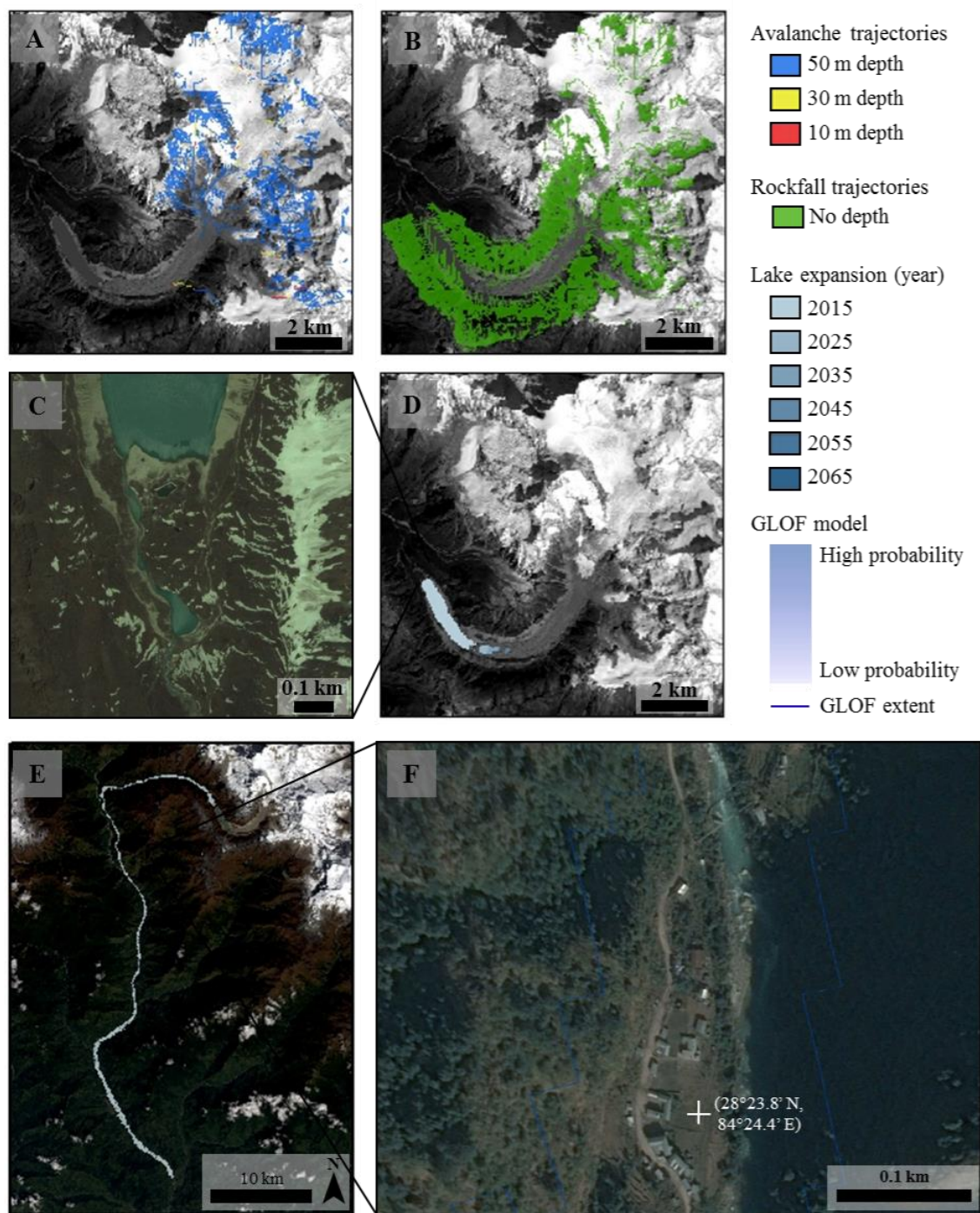


Figure 5.15: Hazards and downstream impact for Thulagi Tsho: (A) avalanche trajectories, (B) rockfall trajectories, (C) ponds on the moraine, (D) future lake expansion, and (E) the extent of the MC-LCP GLOF model (F) highlighting the impacts downstream.

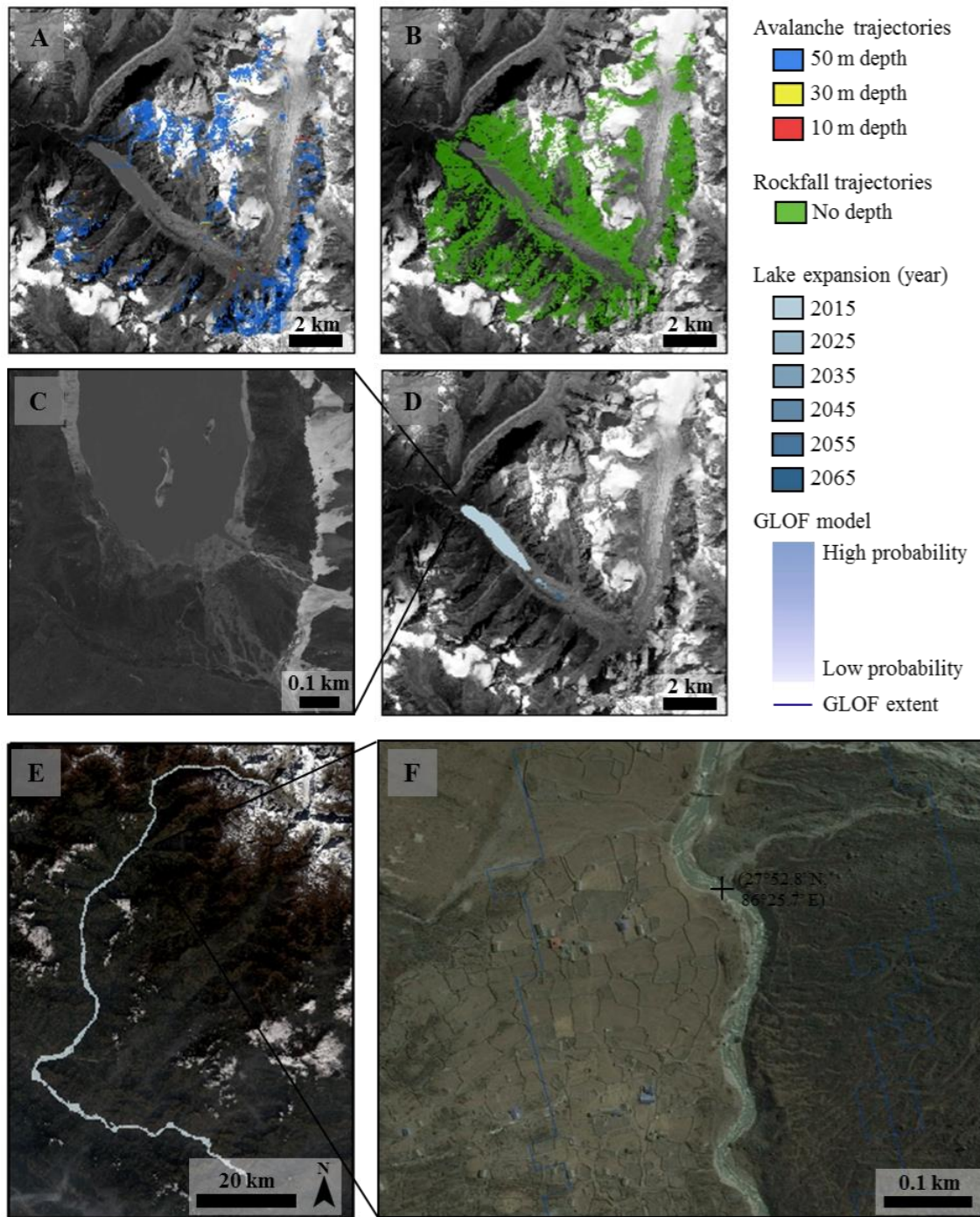


Figure 5.16: Hazards and downstream impact for Tsho Rolpa: (A) avalanche trajectories, (B) rockfall trajectories, (C) the moraine complex, (D) future lake expansion, and (E) the extent of the MC-LCP GLOF model (F) highlighting the impacts downstream.

## **Chapter 6: Conclusions and future perspective**

### **6.1 RESEARCH QUESTIONS**

This body of work integrates remotely sensed data, fieldwork, and modeling to analyze debris-covered glaciers and the hazards associated with their glacial lakes. Chapters 3 and 4 provide details regarding the thickness of debris on these glaciers and their respective ablation rates, while Chapter 5 details a framework that may be used to assess GLOF hazards and risks downstream. The following section will return to the research questions to summarize how this body of work has advanced the current state of knowledge and discuss perspectives moving forward.

#### **6.1.1 How does debris cover affect the evolution of glaciers and glacial lakes in the Everest region of Nepal?**

The role of debris cover on the evolution of glacial lakes has been well documented from an observational perspective (Benn et al., 2012), i.e., the spatial variations in debris cover cause high melt rates upglacier that reduce the topographic gradient of the glacier thereby causing the glacier to stagnate. These stagnant glaciers with gentle slopes ( $< 2^\circ$ ) are susceptible to the formation of melt ponds that may coalesce into a large glacial lake (Quincey et al., 2007). Imja Tsho is a great example of a glacial lake that formed from the coalescence of melt ponds (Watanabe et al., 2009), which originated on a gentle slope (Quincey et al., 2007). One shortfall of these thresholds and observations is they rely on current DEMs and satellite imagery to measure slope and observe melt ponds. The vital component that is missing to understand the evolution of these glaciers and glacial lakes is knowledge regarding the debris thickness.

Fortunately, Chapter 3 presents a method to derive debris thickness from satellite imagery using a debris-covered glacier energy balance model. Debris thickness measurements from fieldwork were used to show that the satellite-derived debris

thickness estimates are quite reasonable. Unfortunately, only a limited number of debris thickness measurements (25 total) were performed due to time and labor constraints such that the satellite-derived debris thickness measurements could not be completely validated. Future work should perform this validation by (1) increasing the sampling frequency and areal extent of samples to match the spatial resolution of the thermal band, (2) improving the spatial resolution of the thermal band through the use of a thermal camera or (3) applying the methods to a large sample of surface temperature measurements at sites with known debris thickness.

Nonetheless, these debris thickness maps provide crucial information regarding the glacier's susceptibility to form a glacial lake. The spatial variation of debris thickness may now be quantified to determine if the debris cover upglacier will cause significant differential melting to alter the topographic gradient and cause glacier stagnation. Future work should model the evolution of debris-covered glaciers using debris thickness maps in conjunction with melt models to understand the future topography of the glacier. A 2° threshold could then be applied to these projections to estimate the time frame and how likely the glacier is to form a glacial lake.

### **6.1.2 What underlying properties and processes are critical for modeling the ablation of debris-covered glaciers?**

Debris-covered glacier energy balance models are a crucial component of modeling the evolution of debris-covered glaciers as they may be used to estimate ablation rates. These energy balance models are dependent on site-specific properties including the debris thickness, thermal conductivity, albedo, and surface roughness. Models also have trouble accounting for the latent heat flux due to a lack of knowledge regarding the moisture within the debris. Furthermore, these models are constrained by the availability of meteorological data, which can vary drastically depending on the

data's temporal and spatial resolution. Chapter 4 analyzed the effect that each of these debris properties and processes has on model performance in addition to assessing the influence of temporal resolution.

The latent heat flux was found to be a crucial component to include using assumptions related to the relative humidity or the precipitation depending on the availability of data. These assumptions allow the latent heat flux to account for the evaporative losses associated with a moist debris surface after a rainfall event. Future work should investigate the role that moisture in the debris has on the latent heat flux and determine the performance of the assumptions regarding the relative humidity and precipitation. The sub-debris ablation rates were most sensitive to thermal conductivity, which governs the rate of heat transfer through the debris. Fieldwork should investigate the link between the thermal conductivity and the moisture in the debris as the moisture is unlikely to be homogenous throughout the debris and will likely significantly alter the heat transfer. The moisture may also have a large impact on the albedo, specifically after rainfall events when the moist surface is likely to reduce the debris' albedo. Net radiation was found to be the dominant component of the energy balance, so understanding how the albedo may vary over time may significantly improve model performance. There are few measurements of albedo on debris-covered glaciers in the Himalaya, which highlights the importance of utilizing satellite imagery to estimate the spatial variations in albedo.

Chapter 4 also developed a new technique to measure the surface roughness on debris-covered glaciers, which has arguably been the least studied debris property in the Himalaya. The surface roughness has large implications on the turbulent heat flux and may vary greatly over the heterogeneous surface of the glacier. This technique appeared to capture the differences resulting from various grain sizes, but should be validated

against aerodynamic roughness measurements. Future work should also investigate linking the in-situ surface roughness measurements to remotely sensed data such that surface roughness maps could be generated. Lastly, the effect of temporal resolution on model performance was investigated. Chapter 4 revealed the 6-hr model underestimated the daily high each day thereby greatly underestimating the total ablation over the melt season. The daily time step was unable to capture the average daily surface temperature; however, the daily model yielded better estimates of total ablation. This effect of temporal resolution is important to consider when using reanalysis datasets. Future work should also assess the performance of simplified melt models, e.g., degree day factor models, which are easier to use especially with future climate scenarios that may not provide the detailed meteorological data required by a full energy balance model.

### **6.1.3 Can remotely sensed data be used to objectively quantify the hazards associated with dangerous glacial lakes?**

Remotely sensed data provides vital information concerning glacial lakes and their surroundings that may be used to classify the hazard of the lake without requiring extensive field campaigns. Chapter 5 details a holistic, reproducible, and objective remote hazard assessment that may be used to understand the hazards associated with glacial lakes throughout Nepal and the Himalaya. The remote assessment analyzes the potential for a dynamic failure from mass entering the lake in the form of snow/ice, rock or debris, and an upstream GLOF. Mass movement entering the lake is the most common cause of GLOF in the Himalaya, so detecting avalanche prone areas remotely and estimating their trajectories is an excellent first step towards understanding the hazards a glacial lake faces. The second most common cause of GLOFs in the Himalaya is self-destruction, which refers to the failure of the terminal moraine due to hydrostatic pressure, a buried ice core, and or time. The remote assessment uses a calculation of the

steep lakefront area to quantify the hydrostatic pressures on the moraine in addition to recognizing melt ponds or changes in the outlet of the moraine that may indicate a buried ice core.

Unfortunately, the implementation of risk-mitigation strategies requires a great deal of time and effort and over that time period the hazards associated with a glacial lake may change. Specifically, as these lakes continue to expand their proximity to potential avalanches and/or rockfalls may change in addition to their expansion likely increasing the volume of water that would be released in a GLOF. The remote assessment described in Chapter 5 is the first model that incorporates future estimations of lake growth into its hazard assessment based on estimates of the glacier's ice thickness and the glacial lake's expansion rate from satellite imagery. These expansion estimates allow one to characterize both the current and future hazards associated with the glacial lakes.

The remote assessment also incorporates the downstream impact through the use of a computationally inexpensive, geometric flood model. These flood models may be used with high resolution satellite imagery, Google Earth, or other platforms to quantify the areas that are at risk in the event of a GLOF. These risk classifications may then be used to direct field campaigns and modeling efforts such that the lakes that are at the highest risk may receive the most attention. The framework developed in this body of work is meant to be widely applicable such that this objective remote assessment may be used to classify the risk of all the glacial lakes in Nepal and guide future work.

#### **6.1.4 What role should field campaigns serve in the management of glacial lakes?**

While the remote assessment provides vital information regarding the hazards and risks associated with glacial lakes, the approach relies on many assumptions and simplistic models that should be improved upon. In this manner, the remote assessment

may be used as a starting point to direct the field campaigns to focus on the most likely triggers for a given glacial lake. For example, if the lake is highly susceptible to an avalanche from a particular slope on the glacier, high resolution satellite imagery and/or fieldwork may be used to determine if this avalanche prone area is in fact a hanging glacier in addition to potentially estimating the size of the avalanche. These field observations or remote estimates may then be used in conjunction with physically based mass movement models to more accurately estimate the avalanche's trajectory. If the trajectory enters the lake, a physically-based GLOF model should be performed to understand the breach of the moraine and the potential impact downstream. However, these models require detailed knowledge of the bathymetry of the lake that may only be measured in the field.

Lumding Tsho described in Chapter 5 is an excellent example of how the remote assessment may be used to guide field efforts. Lumding Tsho is susceptible to avalanches, so detailed measurements of its bathymetry were performed such that the GLOF process chain may be modeled. Additionally, the remote hazard assessment identified the terminal moraine of Lumding Tsho to be susceptible to failure from hydrostatic pressures; however, the fieldwork revealed the slope of its terminal moraine is relatively gentle. Additionally, the flow from Lumding Tsho was entirely constrained to the outlet channel, which further indicated the moraine is fairly stable. Based on this rapid reconnaissance, the hazard associated with the moraine's stability was improved and vital data for modeling a potential GLOF was collected.

In this manner, field campaigns serve a critical role of improving the knowledge regarding the hazard of each glacial lake and providing vital information that may be used in physically based models. The remote assessment reveals that each glacial lake should be treated independently from one another based on the hazard that poses the

biggest threat. Field campaigns are laborious, time-consuming, and expensive, which stresses the importance of directing these efforts to provide the maximum amount of information to further the knowledge of the hazards and risks facing each glacial lake. Ultimately, the goal of these remote assessments and field campaigns is to provide the downstream communities with detailed knowledge of the hazards posed by each glacial lake. The remote, field, and modeling efforts all need to supplement one another in order to be effective.

## **6.2 CONTRIBUTION TO KNOWLEDGE AND CONCLUDING REMARKS**

This body of work improved the current state of knowledge related to debris-covered glaciers and their respective glacial lakes. A debris-covered glacier energy balance model was used to yield reasonable estimates of debris thickness from satellite imagery. These estimates provide vital information regarding the evolution of debris-covered glaciers as the debris thickness controls the sub-debris ablation rates. Field data was used to analyze the performance of the debris-covered energy balance model to determine the properties and processes that have the most impact on the sub-debris ablation rates. This analysis was combined with field techniques that were used to measure some of these debris properties such that future field campaigns can continue to improve model performance. Specific efforts should focus on understanding how the moisture within the debris affects the thermal conductivity and the latent heat flux. The debris-covered glacier energy balance model in conjunction with the estimates of debris thickness allows one to develop an understanding of the evolution of the debris-covered glaciers.

Similarly, the remote assessment developed a technique to model the evolution of a glacial lake based on ice thickness and expansion rates. The combination of sub-debris

ablation rates and the lake expansion allow one to accurately model the evolution of the glacier and the glacial lake. The remote assessment also developed a framework to assess the hazard and risk associated with these glacial lakes that is holistic and repeatable. The framework was developed in a manner that identifies the triggers that pose the biggest threat to each glacial lake such that future field campaigns and modeling efforts can focus on the greatest hazards to each lake with the ultimate goal of providing the downstream communities a thorough understanding of the hazards they face. Future work should aim on upscaling this work to all of Nepal such that field campaigns and risk-mitigation efforts can deliver the maximum benefit to the citizens of Nepal.

## References

- Alean, J.: Ice avalanches: some empirical information about their formation and reach, *J. Glaciol.*, 31(109):324-333, 1985.
- Allen, S.K., Schneider, D., Owens, I.F.: First approaches towards modelling glacial hazards in the Mount Cook region of New Zealand's Southern Alps, *Nat. Hazards Earth Syst. Sci.*, 9:481-499, 2009.
- ASTER GDEM Validation Team, 2011. ASTER global digital elevation model version 2 summary of validation results. <[https://lpda.acaster.cr.usgs.gov/GDEM/Summary\\_GDEM2\\_validation\\_report\\_final.pdf](https://lpda.acaster.cr.usgs.gov/GDEM/Summary_GDEM2_validation_report_final.pdf)> (accessed 02.10.2016).
- Bajracharya, B., Shrestha, A.B., and Rajbhandari, L.: Glacial lake outburst floods in the Sagarmatha region, *Mt Res Dev*, 27(4):336-344, 2007.
- Bajracharya, S.R. and Mool, P.: Glaciers, glacial lakes and glacial lake outburst floods in the Mount Everest region, Nepal, *Ann. Glaciol.*, 50(53):81-86, 2009.
- Barsi, J.A., Schott, J.R., Palluconi, F.D., Helder, D.L., Hook, S.J., Markham, B.L., Chander, G., & O'Donnell, E.M.: Landsat TM and ETM+ thermal band calibration. *Can. J. Remote Sensing*, 29(2):141-153, 2003.
- Benn, D.I., Bolch, T., Hands, K., Gulley, J., Luckman, A., Nicholson, L.I., Quincey, D., Thompson, S., Toumi, R., Wiseman, S.: Response of debris-covered glaciers in the Mount Everest region to recent warming, and implications for outburst flood hazards, *Earth-Science Reviews* 114:156–174, 2012.
- Bolch, T., Buchroithner, M.F., Peters, J., Baessler, M., and Bajracharya, S.: Identification of glacier motion and potentially dangerous glacial lakes in the Mt. Everest region/Nepal using spaceborne imagery, *Nat. Hazards Earth Syst. Sci.*, 8:1329-1340, 2008.

- Bolch, T., Peters, J., Yegorov, A., Pradhan, B., Buchroithner, M., and Blagoveshchensky, V.: Identification of potentially dangerous glacial lakes in the northern Tien Shan, *Nat. Hazards*, 59, 1691-1714, doi:10.1007/s11069-011-9860-2, 2011a.
- Bolch, T., Pieczonka, T., and Benn, D.I.: Multi-decadal mass loss of glaciers in the Everest area (Nepal Himalaya) derived from stereo imagery, *The Cryosphere*, 5:349-358, 2011b.
- Bolch, T., Kulkarni, A., Kääb, A., Huggel, C., Paul, F., Cogley, J.G., Frey, H., Kargel, J.S., Fujita, K., Scheel, M., Bajracharya, S., and Stoffel, M.: The state and fate of Himalayan glaciers, *Science*, 336:310-314, 2012.
- Brock, B.W., Mihalcea, C., Kirkbride, M.P., Diolaiuti, G., Cutler, M.E.J. and Smiraglia, C.: Meteorology and surface energy fluxes in the 2005–2007 ablation seasons at the Miage debris-covered glacier, Mont Blanc Massif, Italian Alps. *J. Geophys. Res.*, 115(D9), D09106, 2010.
- Brock, B.W., Willis, I.C., and Sharp, M.J.: Measurement and parameterization of aerodynamic roughness length variations at Haut Glacier d’Arolla, Switzerland., *J. Glaciol.*, 52(177):281-297, 2006.
- Budhathoki, K.P., Bajracharya, O.R., and Pokharel, B.K.: Assessment of Imja Glacier Lake outburst flood (GLOF) risk in Dudh Koshi River Basin using remote sensing techniques, *Journal of Hydrology and Meteorology*, 7(1):75-91, 2010.
- Byers, A.C., McKinney, D.C., Somos-Valenzuela, M., Watanabe, T., Lamsal, D.: Glacial lakes of the Hinku and Hongu valleys, Makalu Barun national park and buffer zone, Nepal, 69:115-139, doi:10.1007/s11069-013-0689-8, 2013.
- Byers, A.C., Byers, E.A., and Thapa, D.: Conservation and restoration of alpine ecosystems in the Upper Barun valley, Makalu-Barun national park, Nepal, Technical Report No. 2014.11, 2014, The Mountain Institute, Washington D.C., USA.

- Carey, M.: In the shadow of melting glaciers: Climate change and Andean society, Oxford University Press, 2010
- Carrivick, J.L. and Tweed, F.S.: Proglacial lakes: character, behavior and geological importance, *Quaternary Sci Rev*, 78:34-52, 2013.
- Cenderelli, D.A. and Wohl, E.E.: Peak discharge estimates of glacial-lake outburst floods and “normal” climatic floods in the Mount Everest region, Nepal, *Geomorphology*, 40:57-90, 2001.
- Clauge, J.J. and Evans, S.G.: A review of catastrophic drainage of moraine-dammed lakes in British Columbia, *Quaternary Sci. Rev.*, 19:1763-1783, 2000.
- Coll, C., Galve, J.M., Sanchez, J.M., and Caselles, V.: Validation of Landsat-7/ETM+ Thermal-Band Calibration and Atmospheric Correction With Ground-Based Measurements, *IEEE Transactions on Geoscience and Remote Sensing*, 48(1):547-555, 2010.
- Coll, C., Caselles, V., Valor, E., and Niclos, R.: Comparison between different sources of atmospheric profiles for land surface temperature retrieval from single channel thermal infrared data, *Remote Sensing of Environment*, 117:199-210, 2012.
- Collier, E., Nicholson, L.I., Brock, B.W., Maussion, F., Essery, R., and Bush, A.B.G.: Representing moisture fluxes and phase changes in glacier debris cover using a reservoir approach, *The Cryosphere*, 8:1429-1444, doi:10.5194/tc-8-1429-2014, 2014.
- Conway, H. and Rasmussen, L.A.: Summer Temperature Profiles within Supraglacial Debris on Khumbu Glacier, Nepal, *Debris-Covered Glaciers*, Proceedings of a workshop held at Seattle, Washington, USA, September 2000.
- Costa, J.E. and Schuster, R.L: The formation and failure of natural dams, *Geol. Soc. Am. Bull.*, 100:1054-1068, 1988.

- Emmer, A. and Cochachin, A.: The causes and mechanisms of moraine-dammed lake failures in the Cordillera Blanca, North American Cordillera and Himalaya, *AUC Geographica*, 48(2):5-15, 2013.
- Emmer, A. and Vilímek, V.: Review article: lake and breach hazard assessment for moraine-dammed lakes: an example from the Cordillera Blanca (Peru), *Nat. Hazards Earth Syst. Sci.*, 13:1551-1565, 2013.
- Emmer, A. and Vilímek, V.: New method for assessing the susceptibility of glacial lakes to outburst floods in the Cordillera Blanca, Peru, *Hydrol. Earth Syst. Sci.*, 18:3461-3479, 2014.
- Farr, T.G., Rosen, P.A., Caro, E., Crippen, R., Duren, R., Hensley, S., Kobrick, M., Paller, M., Rodriguez, E., Roth, L., Seal, D., Shaffer, S., Shimada, J., Umland, J., Werner, M., Oskin, M., Burbank, D., and Alsdorf, D.: The shuttle radar topography mission, *Rev. Geophys.*, 45:1-33, 2007.
- Foster, L.A., Brock, B.W., Cutler, M.E.J., and Diotri, F.: Instruments and Methods: A physically based method for estimating supraglacial debris thickness from thermal band remote-sensing data, *J. Glaciol.*, 58(210):677-691, 2012.
- Frey, H., Machguth, H., Huss, M., Huggel, C., Bajracharya, S., Bolch, T., Kulkarni, A., Linsbauer, A., Salzmann, N., and Stoffel, M.: Estimating the volume of glaciers in the Himalayan-Karakoram region using different methods, *The Cryosphere*, 8:2313-2333, doi:10.5194/tc-8-2313-2014, 2014.
- Fujisada, H., Bailey, G., Kelly, G., Hara, S., and Abrams, M.: ASTER DEM performance, *Geoscience and Remote Sensing, IEEE Transactions*, 43:2707-2714, 2005.

- Fujita, K., Suzuki, R., Nuimura, T., and Sakai, A.: Performance of ASTER and SRTM DEMs, and their potential for assessing glacial lakes in the Lunana region, Bhutan Himalaya, *J. Glaciol.*, 54(185):220-228, 2008.
- Fujita, K., Sakai, A., Takenaka, S., Nuimura, T., Surazakov, A.B., Sawagaki, T., and Yamanokuchi, T.: Potential flood volume of Himalayan glacial lakes, *Nat. Hazards Earth Syst. Sci.*, 13:1827-1839, doi:10.5194/nhess-13-1827-2013, 2013.
- Fujita, K. and Sakai, A.: Modelling runoff from a Himalayan debris-covered glacier, *Hydrol. Earth Syst. Sci.*, 18:2679-2694, doi:10.5194/hess-18-2679-2014, 2014.
- Fyffe, C.L., Reid, T.D., Brock, B.W., Kirkbride, M.P., Diolaiuti, G., Smiraglia, C., and Diotri, F.: A distributed energy-balance melt model of an alpine debris-covered glacier, *J. Glaciol.*, 60(221):587-602, doi:10.3189/2014JoG13J148, 2014.
- Gardelle, J., Arnaud, Y., and Berthier, E.: Contrasted evolution of glacial lakes along the Hindu Kush Himalaya mountain range between 1990 and 2009, *Global Planet Change*, 75(1-2):47-55, doi:10.1016/j.gloplacha.2010.10.003, 2011.
- Gardelle, J., Berthier, E., Arnaud, Y., and Kääb, A.: Region-wide glacier mass balances over the Pamir-Karakoram-Himalaya during 1999-2011, *The Cryosphere*, 7:1263-1286, doi:10.5194/tc-7-1263-2013, 2013.
- Grabs, W.E. and Hanisch, J.: Objectives and prevention methods for glacial lake outburst floods (GLOFs), in: *Snow and Glacier Hydrology (Proceedings of the Kathmandu Symposium, November 1992)*, Great Yarmouth (UK), 341-342, 1993.
- Gruber, S.: Derivation and analysis of a high-resolution estimate of global permafrost zonation, *The Cryosphere*, 6:221-233, doi:10.5194/tc-6-221-2012, 2012.
- Hambrey, M.J., Quincey, D.J., Glasser, N.F., Reynolds, J.M., Richardson, S.J., and Clemmens, S.: Sedimentological, geomorphological and dynamic context of debris-

- mantled glaciers, Mount Everest (Sagarmatha) region, Nepal, *Quat. Sci. Rev.*, 27:2361-2389, 2008.
- Han, H., Ding, Y., and Liu, S.: A simple model to estimate ice ablation under a thick debris layer, *J. Glaciol.*, 52(179):528-536, 2006.
- Hegglin, E. and Huggel, C.: An integrated assessment of vulnerability to glacial hazards: a case study in the Cordillera Blanca, Peru, *Mt Res Dev*, 28(3-4):299-309, 2008.
- Hock, R. and Noetzli, C.: Areal Melt and Discharge Modelling of Storglaciaren, Sweden, *Ann. Glaciol.*, 24:211-216, 1997.
- Huggel, C., Kääb, A., Haeberli, W., and Krummenacher, B.: Regional-scale GIS-models for assessment of hazards from glacier lake outbursts: evaluation and application in the Swiss Alps, *Nat. Hazards and Earth Syst. Sci.*, 3:647-662, 2003.
- Huggel, C., Kääb, A., and Salzmann, N.: GIS-based modeling of glacial hazards and their interactions using Landsat-TM and IKONOS imagery, *Norwegian Journal of Geography*, 58, 61-73, 2004a.
- Huggel, C., Haeberli, W., Kääb, A., Bieri, D., and Richardson, S.: An assessment procedure for glacial hazards in the Swiss Alps, *Can. Geotech. J.*, 41, 1068-1083, doi:10.1139/T04-053, 2004b.
- Huggel, C., Zraggen-Oswald, S., Haeberli, W., Kääb, A., Polkvoj, A., Galushkin, I., and Evans, S.G.: The 2002 rock/ice avalanche at Kolka/Karmadon, Russian Caucasus: assessment of extraordinary avalanche formation and mobility, and application of Quickbird satellite imagery, *Natural Hazards and Earth System Sciences*, 5, 173-187, 2005.
- ICIMOD-International Centre for Integrated Mountain Development: Glacial lakes and glacial lake outburst floods in Nepal, International Centre for Integrated Mountain Development (ICIMOD), Kathmandu, Nepal, 2011.

- Inoue, J. and Yoshida, M.: Ablation and Heat Exchange over the Khumbu Glacier, *Seppyo*, 41:26-31, 1980.
- Kalnay, E., Kanamitsu, M., Kistler, R. et al.: The NCEP/NCAR 40-year reanalysis project, *Bulletin of the American Meteorological Society*, 77, 437-470, 1996.
- Kayastha, R.B., Takeuchi, Y., Nakawo, M. and Ageta, Y.: Practical prediction of ice melting beneath various thickness of debris cover on Khumbu Glacier, Nepal, using a positive degree-day factor, *Int. Assoc. Hydrol. Sci. Publ.*, 264, 71–81, 2000.
- Khanal, N.R., Mool, P.K., Bhakta, S., Rasul, G., Ghimire, P.K., Shrestha, R.B., and Joshi, S.P.: A comprehensive approach and methods for glacial lake outburst flood risk assessment, with examples from Nepal and the transboundary area, *Water Resources Development*, doi:10.1080/07900627.2014.994116, 2015.
- Lamsal, D., Takanobu, S., and Watanabe, T.: Digital Terrain Modelling Using Corona and ALOS PRISM Data to Investigate the Distal Part of Imja Glacier, Khumbu Himal, Nepal, *Journal of Mountain Science*, 8:390-402, 2011.
- Lamsal, D., Sawagaki, T., Watanabe, T., and Byers, A.C.: Assessment of glacial lake development and prospects of outburst susceptibility: Chamlang South Glacier, eastern Nepal Himalaya, *Geomatics, National Hazards and Risk*, 7(1):403-423, doi:10.1080/19475705.2014.931306, 2016.
- Lejeune, Y., Bertrand, J., Wagnon, P., and Morin, S.: A physically based model of the year-round surface energy and mass balance of debris-covered glaciers, *J. Glaciol.*, 49(214): 327-344, 2013.
- Lettau, H.: Note on aerodynamic roughness-parameter estimation on the basis of roughness-element description, *J. Appl. Meteorol.*, 8:828-832, 1969.
- Liang, S.: Narrowband to broadband conversions of land surface albedo I Algorithms, *Remote Sensing of Environment*, 76:213-238, 2001.

- Mattson, L.E., Gardner, J.S., and Young, G.J.: Ablation on Debris Covered Glaciers: an Example from the Rakhiot Glacier, Punjab, Himalaya, *Int. Assos. Hydrol. Sci. Publ.*, 218, 289-296, 1993.
- McFeeters, S.K.: The use of the normalized difference water index (NDWI) in the delineation of open water features, *Int J Remote Sens*, 17(7):1425-1432, doi:10.1080/01431169608948714, 1996.
- McKillop, R.J. and Clague, J.J.: Statistical, remote sensing-based approach for estimating the probability of catastrophic drainage from moraine-dammed lakes in southwestern British Columbia, *Global Planet. Change*, 56:153-171, 2007a.
- McKillop, R.J. and Clague, J.J.: A procedure for making objective preliminary assessments of outburst flood hazard from moraine-dammed lakes in southwestern British Columbia, *Nat. Hazards*, 41:131-157, 2007b.
- Mergili, M. and Schneider, J.F.: Regional-scale analysis of lake outburst hazards in southwestern Pamir, Tajikistan, based on remote sensing and GIS, *Nat. Hazards Earth Syst. Sci.*, 11:1447-1462, doi:10.5194/nhess-11-1447-2011, 2011.
- METI/NASA/USGS: ASTER Global DEM Validation Summary Report, Tech. rep., METI/ERSDAC, NASA/LPDAAC, USGS/EROS, 2009.
- Mihalcea, C., Brock, B.W., Diolaiuti, G., D'Agata, C., Citterio, M., Kirkbride, M.P., Cutler, M.E.J., and Smiraglia, C.: Using ASTER satellite and ground-based surface temperature measurements to derive supraglacial debris cover and thickness patterns on Miage Glacier (Mont Blanc Massif, Italy), *Cold Regions Science and Technology*, 52:341-354, 2008a.
- Mihalcea, C., Mayer, C., Diolaiuti, G., D'Agata, C., Smiraglia, C., Lambrecht, A., Vuillermoz, E., and Tartari, G.: Spatial distribution of debris thickness and melting

- from remote-sensing and meteorological data, at debris-covered Baltoro glacier, Karakoram, Pakistan, *Ann. Glaciol.*, 48:49-57, 2008b.
- Mool, P.K., Bajracharya, S.R., and Joshi, S.P.: Inventory of glaciers, glacial lakes and glacial lake outburst floods: monitoring and early warning systems in the Hindu Kush-Himalayan region Nepal, International Centre for Integrated Mountain Development (ICIMOD), Kathmandu, Nepal, 2001.
- Munro, D.S.: Surface roughness and bulk heat transfer on a glacier: comparison with eddy correlation, *J. Glaciol.*, 35(121):343-348, 1989.
- Nakawo, M. and Rana, B.: Estimate of Ablation Rate of Glacier Ice Under a Supraglacial Debris Layer, *Geografiska Annaler*, 81(4):695-701, 1999.
- Nakawo, M. and Young, G.J.: Field Experiments to Determine the Effect of a Debris Layer on Ablation of Glacier Ice, *Ann. Glaciol.*, 2:85-91, 1981.
- Nakawo, M. and Young, G.J.: Estimate of Glacier Ablation Under a Debris Layer From Surface Temperature and Meteorological Variables, *J. Glaciol.*, 28(98):29-34, 1982.
- Nakawo, M., Iwata, S. Watanabe, O. and Yoshida, M.: Processes which distribute supraglacial debris on the Khumbu Glacier, Nepal Himalaya, *Ann. Glaciol.*, 8:129-131, 1986.
- Nakawo, M., Yabuki, H., and Sakai, A.: Characteristics of Khumbu Glacier, Nepal Himalaya: recent change in the debris-covered area, *Ann. Glaciol.*, 28:118-122.
- NASA – National Aeronautics and Space Administration: Landsat 7 Science Data Users Handbook. Retrieved January 2011 <<http://landsathandbook.gsfc.nasa.gov>>.
- NASA Land Processes Distributed Active Archive Center (LP DAAC): ASTER GDEM and Landsat7 ETM+ Level 1T Product. USGS/Earth Resources Observation and Science (EROS) Center, Sioux Falls, South Dakota, 2011.

- Nicholson, L. I. “Modelling melt beneath supraglacial debris: implications for the climatic response of debris-covered glaciers.” PhD Thesis, University of St Andrews, 2005.
- Nicholson, L. and Benn, D.I.: Calculating ice melt beneath a debris layer using meteorological data, *J. Glaciol.*, 52:463–470, 2006.
- Nicholson, L. and Benn, D.I.: Properties of Natural Supraglacial Debris in Relation to Modelling Sub-Debris Ice Ablation, *Earth Surface Processes and Landforms*, 38(5):490-501, 2012.
- Nield, J.M., Chiverrell, R.C., Darby, S.E., Leyland, J., Vircavs, L.H., and Jacobs, B.: Complex spatial feedbacks of tephra redistribution, ice melt and surface roughness modulate ablation on tephra covered glaciers, *Earth Surf. Process. Landforms*, 38, 95-102, doi:10.1002/esp.3352, 2013a.
- Nield, J.M., King, J., Wiggs, G.F.S., Leyland, J., Bryant, R.G., Chiverrell, R.C., Darby, S.E., Eckardt, F.D., Thomas, D.S.G., Vircavs, L.H., and Washington, R.: Estimating aerodynamic roughness over complex surface terrain, *Journal of Geophysical Research: Atmospheres*, 118, 12, 948-12, 961, doi:10.1002/2013JD020632, 2013b.
- Nuimura, T., Fujita, K., Yamaguchi, S., and Sharma, R.R.: Elevation changes of glaciers revealed by multitemporal digital elevation models calibrated by GPS survey in the Khumbu region, Nepal Himalaya, 1992-2008, *J. Glaciol.*, 58(210): 648-656, doi:10.3189/2012JoG11J061, 2012.
- Nussbaumer, S., Schaub, Y., Huggel, C., and Walz, A.: Risk estimation for future glacier lake outburst floods based on local land-use changes, *Nat. Hazards Earth Syst. Sci.*, 14:1611-1624, 2014.
- Nuth, C. and Kääb, A.: Co-registration and bias corrections of satellite elevation data sets for quantifying glacier thickness change, *The Cryosphere*, 5:271-290, 2011.

- O'Connor, J.E., Hardison, J.H., and Costa, J.E. (Eds.): Debris flows from failures of Neoglacial-age moraine dams in the Three Sisters and Mount Jefferson Wilderness areas, Oregon, US Geological Survey, Reston (Virginia), 2001.
- Osti, R., Bhattarai, T.N., and Miyake, K.: Causes of catastrophic failure of Tam Pokhari moraine dam in the Mt. Everest region, *Nat Hazards*, 58:1209-1223, doi:10.1007/s11069-011-9723-x, 2011.
- Östrem, G.: Ice Melting under a Thin Layer of Moraine, and the Existence of Ice Cores in Moraine Ridges, *Geografiska Annaler*, 41(4):228-230, 1959.
- Quincey, D.J., Richardson, S.D., Luckman, A., Lucas, R.M., Reynolds, J.M., Hambrey, M.J., and Glasser, N.F.: Early recognition of glacial lake hazards in the Himalaya using remote sensing datasets, *Global Planet. Change*, 56:137-152, 2007.
- Rahimi, C.J. and Konrad, J-M.: Thermal conductivity of compacted snow. *Cold Regions Engineering: Sustainable Infrastructure Development in a Changing Cold Climate*, ASCE, 833-843, 2012.
- Rana, B., Shrestha, A. B., Reynolds, J. M., Aryal, R., Pokhrel, A. P., and Budhathoki, K. P.: Hazard Assessment of the Lake Rolpa Glacier Lake and Ongoing Remediation Measures, *J. Nepal Geol. Soc.*, 22, 563–570, 2000.
- Rees, W.G. and Arnold, N.S.: Scale-dependent roughness of a glacier surface: implications for radar backscatter and aerodynamic roughness modelling, *J. Glaciol.*, 52(177):214-222, 2006.
- Reid, T.D. and Brock, B.W.: An Energy-Balance Model for Debris-Covered Glaciers Including Heat Conduction through the Debris Layer, *J. Glaciol.*, 56(199):903-916, 2010.
- Reid, T.D., Carenzo, M., Pellicciotti, F. and Brock, B.W.: Including debris cover effects in a distributed model of glacier ablation, *J. Geophys. Res.*, 117(D18), D18105, 2012.

- Reynolds, J.M.: Glacial hazard assessment at Tsho Rolpa, Rolwaling, Central Nepal, Q. J. Eng. Geol., 32:209-214, 1999.
- Reynolds, J.M.: On the formation of supraglacial lakes on debris-covered glaciers, Int. Assoc. Hydrol. Sci. Publ., 264, 153–161, 2000.
- Reynolds, J.M.: Development of glacial hazards and risk minimization protocols in rural environments: methods of glacial hazard assessment and management in the Cordillera Blanca, Peru, Reynolds Geo-Sciences Ltd., Flintshire (UK), 2003.
- Richardson, S.D. and Reynolds, J.M.: An overview of glacial hazards in the Himalayas, Quatern Int, 65/66:31-47, 2000.
- Robertson, E.C.: Thermal Properties of Rocks. US Geological Survey (No. 88-441), 1988.
- Rounce, D.R., and McKinney, D.C.: Debris thickness of glaciers in the Everest area (Nepal Himalaya) derived from satellite imagery using a nonlinear energy balance model, The Cryosphere, 8:1317-1329, doi:10.5194/tc-8-1317-2014, 2014.
- Rounce, D.R., Quincey, D.J., and McKinney, D.C.: Debris-covered glacier energy balance model for Imja-Lhotse Shar Glacier in the Everest region of Nepal, The Cryosphere, 9:2295-2310, doi:10.5194/tc-9-2295-2015, 2015.
- Sakai, A., Nishimura, K., Kadota, T., and Takeuchi, N.: Onset of calving at supraglacial lakes on debris-covered glaciers of the Nepal Himalaya, J. Glaciol., 55(193):909-917, 2009.
- Sawagaki, T., Lamsal, D., Byers, A.C., and Watanabe, T.: Changes in surface morphology and glacial lake development of Chamlang South Glacier in the Eastern Nepal Himalaya since 1964, Global Environmental Research, 16:83-94, 2012.

- Shea, J.M., Immerzeel, W.W., Wagnon, P., Vincent, C., and Bajracharya, S.: Modelling glacier change in the Everest region, Nepal Himalaya, *The Cryosphere*, 9:1105-1128, doi:10.5194/tc-9-1105-2015, 2015.
- Shrestha, B.B., Nakagawa, H., Kawaike, K., Baba, Y., and Zhang, H.: Glacial hazards in the Rolwaling valley of Nepal and numerical approach to predict potential outburst flood from glacial lake, *Landslides*, doi:10.1007/s10346-012-0327-7, 2012.
- Smith, M.W.: Roughness in the Earth Sciences, *Earth-Science Reviews*, 136, 202-225, 2014.
- Snively N.: Scene reconstruction and visualization from internet photo collections, Unpublished PhD thesis, University of Washington, USA, 2008.
- Snively, N., Seitz, S.M., and Szeliski, R.: Modeling the world from internet photo collections, *Int. J. Comput. Vis.*, 80:189-210, doi:10.1007/s11263-007-0107-3, 2008.
- Somos-Valenzuela, M.A., McKinney, D.C., Rounce, D.R., and Byers, A.C.: Changes in Imja Tsho in the Mount Everest region of Nepal, *The Cryosphere*, 8:1661-1671, doi:10.5194/tc-8-1661-2014, 2014.
- Somos-Valenzuela, M.A., McKinney, D.C., Byers, A.C., Rounce, D.R., Portocarrero, C., and Lamsal, D.: Assessing downstream flood impacts due to a potential GLOF from Imja Tsho in Nepal, *Hydrol. Earth Syst. Sci.*, 19:1401-1412, doi:10.5194/hess-19-1402-2015, 2015.
- Sturm, M., Holmgren, J., König, M., and Morris, K.: The thermal conductivity of seasonal snow, *J. Glaciol.*, 43, 26-41, 1997.
- Sturm, M., Perovich, D.K., and Holmgren, J.: Thermal conductivity and heat transfer through the snow on the ice of the Beaufort Sea, *J. Geophys. Res.*, 107(C21), 2002.

- Suzuki, R., Fujita, K., and Ageta, Y.: Spatial Distribution of Thermal Properties on Debris-Covered Glaciers in the Himalayas Derived from ASTER Data, *Bulletin of Glaciological Research*, 24:13-22, 2007.
- Szeliski, R.: *Computer Vision: algorithms and applications*. Springer, London, 2011.
- Takeuchi, Y., Kayastha, R. B. and Nakawo, M.: Characteristics of ablation and heat balance in debris-free and debris-covered areas on Khumbu Glacier, Nepal Himalayas, in the pre-monsoon season, *Int. Assoc. Hydrol. Sci. Publ.*, 264, 53–61, 2000.
- Thakuri, S., Salerno, F., Bolch, T., Guyennon, N., and Tartari, G.: Factors controlling the accelerated expansion of Imja Lake, Mount Everest region, Nepal, *Ann. Glaciol.*, 57(71):245-257, doi:10.3189/2016AoGA063, 2015.
- UNDP-United Nations Development Programme: *Community Based Glacier Lake Outburst and Flood Risk Reduction in Nepal*. Project Document, UNDP Environmental Finance Services, Kathmandu, Nepal, 2013.
- Vuichard, D. and Zimmermann, M.: The 1985 catastrophic drainage of a moraine-dammed lake, Khumbu Himal, Nepal: cause and consequences, *Mt Res Dev*, 7(2):91-110, 1987.
- Wang, X., Shiyin, L., Wanqin, G., Junli, X.: Assessment and simulation of glacier lake outburst floods for Lonbasaba and Pida lakes, China, *Mt Res. Dev.*, 28(3):310-317, doi:10.1659/mrd.0894, 2008.
- Wang, X., Yao, T., Gao, Y. Yang, X., and Kattel, D.B.: A first-order method to identify potentially dangerous glacial lakes in a region of the southeastern Tibetan Plateau, *Mt Res Dev*, 31(2):122-130, doi:10.1659/MRD-JOURNAL-D-10-00059.1, 2011.
- Wang, X., Liu, S., Ding, Y., Guo, W., Jiang, Z., Lin, J., Han, Y.: An approach for estimating the breach probabilities of moraine-dammed lakes in the Chinese

- Himalayas using remote-sensing data, *Nat. Hazards Earth Syst. Sci.*, 12:3109-3122, 2012.
- Watanabe, T., Ives, J.D., and Hammond, J.E.: Rapid growth of a glacial lake in Khumbu Himal, Himalaya: prospects for a catastrophic flood, *Mt Res Dev*, 14(4):329-340, 1994.
- Watanabe, T., Lamsal, D., and Ives, J.D.: Evaluating the growth characteristics of a glacial lake and its degree of danger of outburst flood: Imja Glacier, Khumbu Himal, Nepal, *Norwegian Journal of Geography*, 63:255-267, 2009.
- Watson, C.S., Carrivick, J., Quincey, D.: An improved method to represent DEM uncertainty in glacial lake outburst flood propagation using stochastic simulations, *J. Hydrol.*, 529:1373-1389, 2015.
- Westoby, M.J., Brasington, J., Glasser, N.F., Hambrey, M.J., and Reynolds, J.M.: 'Structure-from-Motion' Photogrammetry: A low-cost, effective tool for geoscience applications, *Geomorphology*, 179:300-314, 2012.
- Westoby, M.J., Glasser, N.F., Brasington, J., Hambrey, M.J., Quincey, D.J., and Reynolds, J.M.: Modelling outburst floods from moraine-dammed glacial lakes, *Earth-Sci Rev*, 134:137-159, 2014.
- Westoby, M.J., Brasington, J., Glasser, N.F., Hambrey, M.J., Reynolds, J.M., Hassan, M.A.A.M., and Lowe, A.: Numerical modelling of glacial lake outburst floods using physically based dam-breach models, *Earth Surf. Dynam.* 3:171-199, doi:10.5194/esurf-3-171-2015, 2015.
- Worni, R., Huggel, C., and Stoffel, M.: Glacial lakes in the Indian Himalayas – from an area-wide glacial lake inventory to on-site and modeling based risk assessment of critical glacial lakes, *Science of the Total Environment*, 468-469:S71-S84, 2013.

Yamada, T.: Glacier lake and its outburst flood in the Nepal Himalaya, Tokyo, Japanese Society of Snow and Ice, 1-96, 1998.

Zhang, Y., Fujita, K., Liu, S., Liu, Q., and Nuimura, T.: Distribution of Debris Thickness and its Effect on Ice Melt at Hailuogou Glacier, Southeastern Tibetan Plateau, Using In Situ Surveys and ASTER Imagery, *J. Glaciol.*, 57(206):1147-1157, 2011.